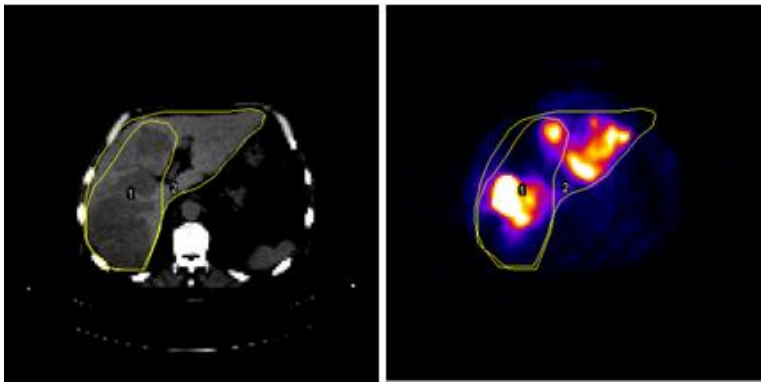

Development of an advanced partition model dosimetry system for hepatic radioembolization using ^{90}Y-microspheres

Vera Catarina Marques Antunes

Mestrado em Física Médica

Departamento Física e Astronomia

2017

Orientador

João António Miranda dos Santos, PhD
Assessor de Saúde (Física Médica) no Instituto Português de Oncologia Francisco Gentil, EPE;
Professor Afiliado da Universidade do Porto (ICBAS)

Todas as correcções determinadas pelo júri, e só essas, foram efectuadas.

O Presidente do Júri,

Porto, _____/_____/_____

Acknowledgements

Foremost, I would like to express my deepest gratitude to my supervisor, Professor João Santos, for his expert advice and encouragement throughout this thesis.

I thank profusely all Service of Nuclear Medicine, especially to Dr. Hugo Duarte, director of the Service, for their kind help and co-operation throughout my study period.

To my boyfriend and to all friends who in one way or another shared their support, either morally and physically. Thank you.

Finally and most importantly, I would like to thank my parents for allowing me the opportunity to realize my dreams, for their love and unconditional support throughout my years of study. My love for them is beyond words. Thank you.

Abstract

According to 2013/59/Euratom BSS, for all medical exposure of patients for radiotherapeutic purposes, including Nuclear Medicine, doses in target volumes shall be individually planned. Furthermore, doses to non-target volumes (e.g. organs-at-risk) shall be as-low-as-reasonably-achievable and consistent with the intended radiotherapeutic purposes. For ^{90}Y-microspheres radioembolization, four methods of activity calculation to be administered are usually used. For resin microspheres are presented three: empirical, body-surface-area (BSA) and partition methods. For glass microspheres application, only an activity calculation method is available.

The ^{99m}Tc-MAA is primarily used for LSF analysis and evaluation of extrahepatic deposition, with the aim to predict intrahepatic post-therapy ^{90}Y-microspheres distribution. Usually performed by planar and SPECT/CT imaging. In addition, treatment efficacy of radioembolization is assessed by the ^{90}Y Bremsstrahlung SPECT imaging. However, Bremsstrahlung SPECT imaging demonstrates a poor image quality.

A total of sixty two patients were evaluated for radioembolization after the ^{99m}Tc-MAA procedure and were treated with resin microspheres using the BSA method for activity calculation. A retrospective evaluation indicates that more than 35% of the treated patients have hepatocellular carcinoma. This analysis also indicates that a large number of patients did not present a significant LSF (approximately 80%), and the average of resin microspheres activity was about 1.70 ± 0.42 GBq. However, the three cases analyzed show the limitation of the currently used BSA activity calculation method compared with a partition method.

In conclusion, caution regarding patient selection, treatment preparation including an appropriate dosimetry, and performance is particularly important to prevent toxicity to be associated with this treatment. Thus, the shift towards personalized radionuclide therapy should be the way forward.

Keywords: Radioembolization; ^{90}Y; Internal dosimetry; Nuclear Medicine; Radiotherapy

Resumo

De acordo com a diretiva 2013/59/Euratom, para todas as exposições médicas de pacientes com fins radioterapêuticos, incluindo a Medicina Nuclear, as doses em volumes alvo devem ser planeadas individualmente. Além disso, as doses para volumes não visados (por exemplo, órgãos de risco) devem ser tão baixas quanto razoavelmente possível e consistentes com os propósitos radioterapêuticos pretendidos. Para a radioembolização com microesferas de ^{90}Y, são utilizados geralmente quatro métodos de cálculo de atividade a ser administrada. Para as microesferas de resina são apresentados três: método empírico, método do *BSA* e método de partição. Para a aplicação de microesferas de vidro, apenas um método de cálculo de atividade está disponível.

^{99m}Tc-MAA é utilizado principalmente para análise de *LSF* e avaliação de deposição extra-hepática, com o objetivo de prever a distribuição intra-hepática de pós-terapia com microesferas de ^{90}Y. Geralmente realizado através de imagens planar e SPECT/CT. Além disso, a eficácia do tratamento da radioembolização é avaliada pela imagem SPECT de ^{90}Y Bremsstrahlung. No entanto, a imagem SPECT de Bremsstrahlung demonstra uma baixa qualidade de imagem.

Um total de sessenta e dois pacientes foram avaliados para radioembolização após o procedimento de ^{99m}Tc-MAA e foram tratados com microesferas de resina usando o método *BSA* para o cálculo de atividade. Uma avaliação retrospectiva indica que mais de 35% dos pacientes tratados apresentam carcinoma hepatocelular. Esta análise também indica que um grande número de pacientes não apresentou *LSF* significativo (aproximadamente 80%), e a média da atividade administrada de microesferas de resina foi de cerca de 1,70 ± 0,42 GBq. No entanto, os três casos analisados mostram uma limitação do método *BSA* para o cálculo da atividade em comparação com um método de partição.

Em conclusão, o cuidado com a seleção do paciente, a preparação do tratamento, com uma dosimetria apropriada, e o desempenho são particularmente importantes para evitar que a toxicidade seja associada a este tratamento. Assim, a mudança para a terapia personalizada com radionuclídeos deve ser o caminho a seguir.

Palavras-chave: Radioembolização; ^{90}Y, Dosimetria interna; Medicina Nuclear, Radioterapia

List of Publications Accepted Resulting from the Developed Work

"Comparison of three dose calculation methodologies for Y-90 microspheres radioembolization", V. Antunes, J.A.M Santos

Accepted as a poster in the 1º European Congress of Medical Physics, September 1-4, 2016, Athens Greece.

Contents

List of Tables

List of Figures

List Abbreviations and Acronyms

^{111}In	Indium-111
^{153}Sm-EDTMP	Samarium-153 ethylenediaminetetramethylenephosphonate
^{177}Lu	Lutetium-177
^{186}Re-HEDP	Rhenium-186 hydroxyethylidene diphosphonate
^{32}P	Phosphorus-32
^{89}Sr	Strontium-89
^{90}Y	Yttrium-90
^{99m}Tc-MAA	Technetium-99m-Macroaggregated Albumin
A_{total}	Total activity
Bq	Becquerel
BSA	Body Surface Area
CT	Computed Tomography
D_{Lung}	Dose to the lung
DNA	Deoxyribonucleic Acid
D_{NL}	Dose to the normal liver
D_T	Dose to the tumor
EANM	European Association of Nuclear Medicine
EC	Electron Capture
Euratom	European Atomic Energy Community
FBP	Filtered Backprojection
FDA	Food and Drug Administration
Gy	Gray
HCC	Hepatocellular Carcinoma
IC	Internal Conversion

IPO-PORTO	Instituto Português de Oncologia Francisco Gentil, EPE do Porto
I_T	Tumor involvement
LET	Linear Energy Transfer
LSF	Lung Shunt Fraction
MIRD	Medical Internal Radiation Dose
MLEM	Maximum Likelihood Expectation Maximization
MR	Magnetic Resonance
NET	Neuroendocrine Tumors
OSEM	Ordered Subsets Expectation Maximization
PET	Positron Emission Tomography
PHA	Pulse-Height-Analyzer
PM	Partition Method
PMT	Photomultipliers Tube
RIT	Radioimmunotherapy
ROI	Region-of-interest
SIRT	Selection Internal Radiation Therapy
SPECT	Single Photon Emission Computed Tomography
TRT	Targeted Radionuclide Therapy
V_{Lung}	Volume of the lung
V_{NL}	Volume of the normal liver
V_T	Volume of the tumor

1. Introduction

1.1. Dissertation Context

Liver cancer, from metastatic cancer to hepatocellular carcinoma (HCC), is a highly fatal disease being the second most common cause of death from cancer in the world [1]. More than 700,000 new liver cancer cases throughout the world and accounting for more than 600,000 deaths occurred worldwide each year [2].

One HCC option of treatment, being proposed to certain patients as a locoregional treatment, involves either chemoembolization or radioembolization. Radioembolization is based on the administration of a large quantity of microspheres labeled with yttrium-90 (^{90}Y) in the arterial vasculature of the liver, commonly known as selective internal radiation therapy (SIRT), reaching (and depositing a required dose) the tissues intended to be treated [3,4]. The ^{90}Y transarterial radioembolization is a complex technique and requires a multidisciplinary approach to planning, delivering and reviewing cancer treatment [5].

According to 2013/59/Euratom BSS: *For all medical exposure of patients for radiotherapeutic purposes, exposures of target volumes shall be individually planned and their delivery appropriately verified taking into account that doses to non-target volumes and tissues shall be as low as reasonably achievable and consistent with the intended radiotherapeutic purpose of the exposure.* That is, to ensure the safe use of radioactively labeled drugs in medical practice, it is necessary to determine the radiation dose received by the patient (specially the treatment volume, sparing the healthy tissues) [6]. For ^{90}Y-microspheres radioembolization, four different models are available for planning the radiation activity for the tumor. For resin microspheres, the previously used activity calculation method was the empiric method. The empirical method is based uniquely on percentage of tumor mass, without any other patient-based factor. The second method, the body surface area (BSA), is the semiempiric method. This is the most widely used methodology for determination the amount of ^{90}Y-microspheres activity to be administrated to patients and is relatively simple, not taking into account significant variations such as tumor size, shape or location. This model assumes that the size of each patient's liver correlates with the BSA. A third, more sophisticated method is the partition method. It is based on tumor and normal liver volumes and expected activity distribution, predicted by single photon emission

computed tomography (SPECT) imaging. The partition model is more accurate, scientifically rigorous and personalized, but less popular due to its relative complexity. For glass microspheres application, only an activity calculation method is available [7–9].

A simulation of the real treatment is performed prior radioembolization with technetium-99m-macroaggregated albumin (^{99m}Tc-MAA). ^{99m}Tc-MAA allows that planar and SPECT gamma-camera imaging and it is used to calculate the lung shunt fraction (LSF) and detect any extrahepatic deposition of activity. Moreover, ^{99m}Tc-MAA can also be used to predict the intrahepatic distribution of ^{90}Y-microspheres and subsequently prescribe on an individualized treatment planning including a dosimetry step. Dosimetry can be used to optimize the tumor response and treatment efficacy with acceptable toxicity preventing complications by administration the highest possible activity to the tumor while maintaining low radiation dose to the sensitive and other healthy tissues [8–11].

1.2. Dissertation Aim

Yttrium-90 radioembolization is a well-established therapy for the treatment of the liver diseases and also of metastatic liver deposits from other malignancies. The first aim this work was to make an evaluation be about ^{90}Y-microspheres techniques and challenges facing it in terms of the dosimetry with focus on the Partition Method. In addition, in radionuclide therapy it is necessary to measure the distribution of the radiopharmaceutical *in vivo.* Measurements are usually performed by SPECT imaging. Thus, the second aim was to investigate the quality of Bremsstrahlung SPECT imaging using different reconstruction methods.

1.3. Dissertation Structure

This thesis is comprised of a background chapter and a series of chapters describing the findings and outcomes of this research.

The second chapter presents general concepts of Nuclear Medicine that will be needed throughout this work. Chapter 2 includes the physics behind the Nuclear Medicine, the components and operation of a gamma camera as well as the development of SPECT reconstruction methods. And still the concepts and the current practice of nuclide therapy and the fundaments of the internal radionuclide radiation.

The third chapter presents the methodology of ^{90}Y-microspheres radioembolization including treatment planning, activity and dose calculation and therapy.

In chapter 4 is clarified the methodology used in this work with a pre-therapy and post-therapy evaluation.

Chapter 5 summarizes the results obtained as well as discussion of one of them.

The last chapter presents the conclusions and discusses the future work.

2. Nuclear Medicine Fundamentals

Nuclear medicine is a medical specialty that involves the administration of radioactive tracers (radiopharmaceuticals) that are used to diagnostic information and treat diseases in a safe and painless way. The radiopharmaceutical has a radionuclide labeled with a pharmaceutical and the mode of tracer administration will depend on the disease process that will to be implemented. For most diagnostic studies in nuclear medicine, the radioactive tracer is administered to a patient by intravenous injection. However, the radiopharmaceutical may also be administered by inhalation, by oral ingestion, or by direct injection into an organ [12].

The type of radiation used is strongly linked with the purpose of the radiopharmaceutical. For diagnosis, the pharmaceutical is labeled with a gamma-ray-emitting radionuclide or positron-emitting radionuclide. In therapy the radionuclide ideally has a pure negative beta-emitting or an alpha-emitting radionuclide. When the radionuclide decays, gamma-rays or high-energy photons are also emitted. Although some radiation interacts with body tissues by scatter and attenuation, a significant number can exit the body. The radiation that escapes can be externally detected by a sensitive gamma camera, and can be used to form an image of the distribution of the radiopharmaceutical in the body. The image of gamma-ray emission is performed with a single photon imaging (Planar imaging or SPECT with Anger camera) and the positron imaging (PET) is used when there is a positron emission.

This work focuses on a particular therapeutic use of radionuclides in modern medicine. Before discussing about radionuclide therapy, a brief introduction on important concepts will be presented.

2.1. Quantitative Imaging

Radionuclide therapy is gradually becoming more important as a therapy option in various diseases or as adjunct to external beam radiotherapy and chemotherapy [13]. Nuclear medicine imaging plays an important role in this process, before, during and after the therapy. Prior to the therapy, imaging can be used to predict dose to the tumor and surrounding organs, using a surrogate radiopharmaceutical. During treatment can be used for delivery control and dose assessment. After therapy it is important to follow the patient's response [14].

Nuclear medical imaging is based on detection of radiation distribution emitted from the body after administering a radiopharmaceutical. Thus, radionuclides that emit photons with appropriate energy (typically in the 60 to 600 keV range) for imaging during decay, the activity distribution *in vivo* can be estimated by imaging these photons outside the body using a scintillation gamma-camera. At the same time, the energy should not be so high that it cannot be collimated or detected efficiently. Gamma-emission imaging may be subdivided into categories, planar scintigraphy and emission tomography in the form of single photon emission computed tomography (SPECT) [15].

2.1.1. Radioactive decay

Radiological physics began with the discovery of x-rays by Wilhelm Rontgen, of natural radioactivity by Henri Becquerel, and of Polonium and Radium by the Curies in the 1890s. The introduction of artificial radioactivity by I. Curie and Joliot prompted the invention of cyclotrons and reactors in which many radionuclides are now produced with different physical properties [16].

Radioactive decay is a spontaneous process in which an unstable nucleus (*parent*) transforms into a more stable configuration (*daughter*) through expulsion of energetic particles. In many cases, the daughter is also radioactive and undergoes further radioactive decay. This process results in the conversion of mass into energy and the total energy (mass, quantum and kinetic) of photons and other particles released by the disintegration process is equal to the net decrease in the rest mass of the neutral atom. Total energy, momentum, and electric charge are each conserved in the process [17].

Each radionuclide has a set of characteristic properties that include the mode of radioactive decay and type of emissions. The radioactive nuclei, *X*, disintegration is characterized by changes in the atomic number, *Z* (number of protons) and mass number, *A* (number of nucleons) when decays into a daughter, *Y* (Table 1). The main disintegration processes are alpha decay (α), electron decay (β^-), positron decay (β^+), electron capture and gamma decay (γ). Several others processes can be also involved [18].

Table 1 - Variation of atomic number (*Z*) and number of nucleons (*A*) in decay process.

	ΔZ	ΔA
α-particle	- 2	-4
β^--particle	+1	0
β^+-particle	-1	0
γ-ray	0	0

ALPHA DISINTEGRATION

The α-decay occurs mainly in heavy nuclei such as uranium, plutonium and so forth. The α-particles consist in helium ions with two protons and two neutrons. The standard notation of the decay by an α-particle emission is represented as:

$$\mathbf{{}^{A}_{Z}X \xrightarrow{\alpha} {}^{A-4}_{Z-2}Y + {}^{4}_{2}He} \qquad \textbf{Equation 1}$$

After decay, the mass number of the nucleus is reduced by 4 and the mass number by 2, resulting in a transformation of elements. The kinetic energy of the α-particle is, in general, between 4 and 8 MeV. Despite the high-energy of the α-particles, they present several difficulties in diagnostic medical imaging, because the range is very short and cannot even penetrate the outer, dead layer of skin, Bremsstrahlung x-ray is also a major problem. However, α-particles have an increase medical interest for radiation therapy (e.g. Radium-223) [12,16].

BETA DISINTEGRATION

Beta decay

When a radionuclide is neutron rich, it tends to emit an electron (β^--particle), leaving the nucleus with one less neutron and one more proton. Schematically, the process is:

$$\mathbf{n \rightarrow p + \beta^- + \bar{\nu}} \qquad \textbf{Equation 2}$$

The β^--particle and the antineutrino ($\bar{\nu}$) are created at the moment of nuclear decay. The antineutrinos have no electric charge or mass, they do not interact with matter and therefore are essentially undetectable, unless in rather sophisticated experiments. In the β^--decay, a neutron is converted to a proton, thus the atomic number *Z* is increased by 1. The atomic mass-energy balance equation is:

$$ {}^{A}_{Z}X \xrightarrow{\beta^-} {}^{A}_{Z+1}Y + \beta^- + \overline{\nu} \qquad \text{Equation 3} $$

Mass number, *A*, does not change, this because the total number of nucleons (protons + neutrons) remains constant, so that the parent and daughter are isobars.

The energy released in the negative β^--decay, this is, the difference of energy between parent and daughter nuclides is called the *transition energy* (E_{max}). The E_{max} is the maximum possible β^--particle energy, may be also shared with antineutrino. This result in a spectrum of energy as showed in Figure 1.

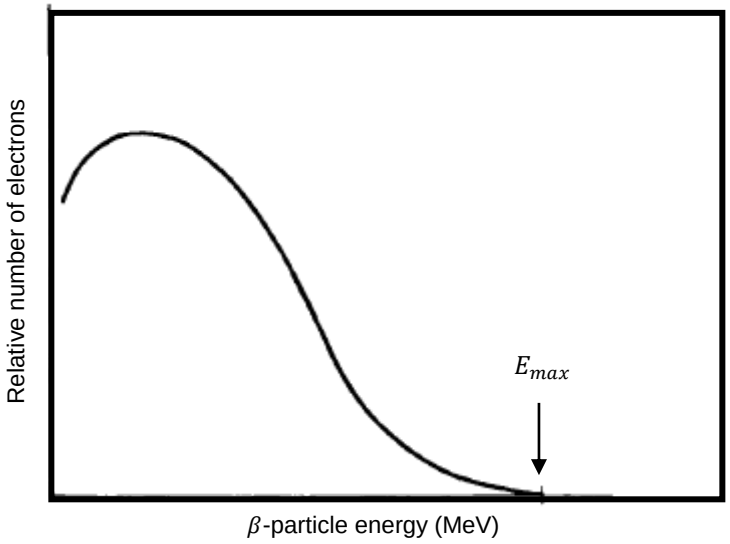

Figure 1 - Shape of typical energy spectrum for β-particles (adapted from Podgorsak, 2010).

Pure beta-rays can penetrate only relative small thicknesses travelling a short distance inside the tissue. Thus they are not useful for diagnostic imaging, because it is impossible to detect β-particles coming from a patient with a detector. Bremsstrahlung radiation is used, with poor image quality results. Nevertheless, a pure beta-emitter can be used in radionuclide therapy, as will be seen in section 2.2. In some cases, the beta-emitter radionuclides also emit gamma-rays. As mentioned, the high-energy of β^--particles can emit Bremsstrahlung x-ray. This can be the only radiation that is used for measurement *in vivo* [12,16,17].

Bremsstrahlung is the German term for “braking radiation”. In the Bremsstrahlung process, a charged particle (β) travelling in a material is slowed when it is deflected by another charged particle. As a high speed electron passes near atomic nucleus, its path of travel will be changed somewhat in the direction of the nucleus and, subsequently slow down and loses energy. In these cases, the energy lost is released in the form of electromagnetic radiation, called *Bremsstrahlung*.

Positron decay

In the other hand, when the radionuclide has an excess of protons in the nucleus usually occurs a positron emission (β^+-particle) accompanied by the emission of a neutrino. A positron is the antiparticle of an ordinary electron and its emission only occurs when the energy difference (transition energy) between the parent and daughter nuclides is greater than 1.02 MeV. In positron decay, essentially a proton is converted to a neutron reducing *Z* by one unit and leaving *A* unchanged:

$$\boldsymbol{p \rightarrow n + \beta^+ + \nu} \qquad \textbf{Equation 4}$$

$$\boldsymbol{{}^{A}_{Z}X \xrightarrow{\beta^+} {}^{A}_{Z-1}Y + \beta^+ + \nu} \qquad \textbf{Equation 5}$$

After β^+-emission, it loses its energy passing through matter. The range of β^+-particles is short in matter, thus it interacts with a nearby electron and is annihilated, given rise to two photons of 0.511 MeV emitted in almost opposite directions. This process is called *annihilation reaction* and permits that the resulting photons to be useful in diagnostic imaging (PET) [12,16].

ELECTRON CAPTURE

Some nuclei undergo a radioactive decay by capturing an orbital electron, usually from K-shell because of its proximity. The captured electron is combined with a proton to form a neutron and eject a monoenergetic neutrino [12,17]. This reaction is an alternative to β^+-decay with same net effect, the *Z* decreases by 1, but *A* unchanged.

$$\boldsymbol{p + e^- \rightarrow n + \nu} \qquad \textbf{Equation 6}$$

$$\boldsymbol{{}^{A}_{Z}X \xrightarrow{EC} {}^{A}_{Z-1}Y + \nu} \qquad \textbf{Equation 7}$$

In this process, vacancy is created in the shell from which the electron is captured. When the vacancy is filled by the transition of an electron from the next upper shell, the remaining energy appears as characteristic x-ray and/or Auger electron emitted by the daughter nuclide [16].

GAMMA-RAY EMISSION

Gamma-ray decay occurs when a daughter nuclei in an excited state releases its excess energy by emission of electromagnetic radiation (photons) until it achieves a stable level. Transitions that result in gamma emission leave *Z* and *A* unchanged and

are called *isomeric transition*. These states may have lifetimes of fraction of picoseconds to many years. When isomeric states are long lifetime is known as *metastable state*, as in the case of the ^{99m}Tc [16].

Metastable radionuclides are of great importance in nuclear medicine due to the fact that gamma-energy can be easily detected by external equipment. Although metastable nuclides always emit a certain number of conversion electrons, they do not contribute for the image because almost all are absorbed within the tissue [12].

INTERNAL CONVERSION

An alternative to the γ-ray decay is the *internal conversion* (IC) process. This process can occur if excited nucleus transfers the excitation energy to an orbital electron, which is ejected instead of the γ-ray. The ejected electron is called the *conversion electron* and carries the energy excess above the biding energy as kinetic energy. The orbital vacancy created by internal conversion consequently is filled by an electron from the next higher shell. And, such as in electron capture, characteristic x-ray and/or Auger electron are emitted [16].

2.1.2. Radioactivity

Radioactivity is characterized as spontaneously emission of radiation by an unstable nuclide. In general, there are two classifications of radioactivity: natural and artificial. However, the radioactive decay is a random process and is no way to predict with certainty the exact moment of its transformation into another stable nucleus. Mathematically, radioactive decay is described in terms of probability and average decay rates.

The decay rate of a radionuclide is the number of disintegration per unit time, also referred as *activity*, denoted by *A*. In the others words, the activity is proportional to the total number of radioactive nuclei (*dN*) that decay in a period of time (*dt*) (Equation 8). The traditional unit of activity is the *Curie* (*Ci*), even though by System International (SI) the official unit of activity is the *Becquerel* (*Bq*), defined as one disintegration per second: 1 Bq = 1 s^{-1}. The curie is thus defined as 1Ci = 3.7 x 10^{10}Bq.

$$\boldsymbol{A = -\frac{dN}{dt} = \lambda N} \qquad \textbf{Equation 8}$$

The negative signal means that *N* decreases as the time *t* increases. The quantity λ is the decay constant of the radionuclide and it has the dimensions of inverse time (s^{-1}).

The decay constant is a characteristic value for each radionuclide and it represents a small fraction of the radioactive atoms that decays in a very short period of time [12,16,17].

With the passage of the time, the number of atoms (*N*) in a sample decreases and consequently the activity also decreases. The factor that represents this decay is obtained by integration of Equation 8. The result is:

$$\boldsymbol{N_t = N_0 e^{-\lambda t}} \qquad \textbf{Equation 9}$$

$$\boldsymbol{A_t = A_0 e^{-\lambda t}} \qquad \textbf{Equation 10}$$

where N_t is the number of atoms remaining after a time t, N_0 is the number of atoms at time $t = 0$ and $e^{-\lambda t}$ is the decay factor. The decay factor is an exponential function of time, thus both the number of radioactive atoms and activity remaining in the sample are decreasing continuously with time. A graph of either of these quantities is a curve that gradually approaches zero [19].

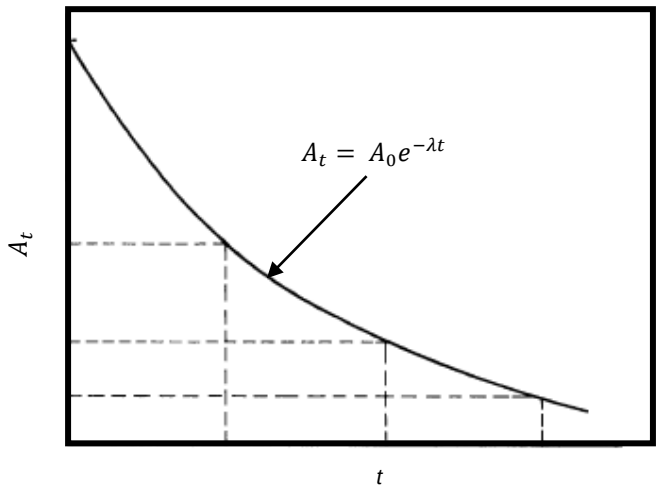

Figure 2 - Exponential radioactivity decay, showing relative activity, *A*, as a function of time, *t* (adapted from Turner, 2007).

Every nuclide is characterized by a half-life ($\tau_{1/2}$), which is the expectative value of the time required for one-half of the initial radioactive atoms to disintegrate, and therefore the sample reduce to half of its existing activity. The decay constant and half-life of a radionuclide are related as [17]:

$$\boldsymbol{\tau_{1/2} = \frac{\ln 2}{\lambda}} \qquad \textbf{Equation 11}$$

When considering the use of radioactive drugs for both diagnostic and therapeutic purposes another characteristic to be considered. This is because it disappears from

the body not only by radioactive decay but also by biological clearance. In this way, a new factor arises, the effective half-life (τ_{eff}). It is defined as the period of time required to reduce the radioactivity level of an internal organ or of whole body to one half its initial value due to both decay and elimination. The effective half-life is then related by:

$$\frac{1}{\tau_{eff}} = \frac{1}{\tau_p} + \frac{1}{\tau_b} \qquad \text{Equation 12}$$

The effective half-life takes into account not only the radioactive decay represented by physical half-life (τ_p) but also the elimination represented by biological half-life (τ_b). While the physical half-life is unaffected by anything that human can do to the radionuclide because is unique parameter for each radionuclide. The biological half-life represents the period of time required to reduce the amount of a radiopharmaceutical the body to one half its original value due solely to biological elimination [16].

2.1.3. Gamma camera imaging

Anger scintillation camera or gamma camera, as popularly called, is the most common imaging system used in Nuclear Medicine and radionuclide therapy [20]. It is called in honor of Hal O. Anger, who invented it in the late 1950s [12]. The equipment detects gamma photons emitted by radionuclides and forms planar or 2D projection images of the 3-D distributed radionuclides *in vivo* [15].

Many sophisticated improvements have been made on the gamma cameras over the years. However, the basic principles of the operation have essentially remained the same. Figure 3 illustrates the basic principles of image formation with the gamma camera. The gamma camera converts photons, emitted from and transmitted through the patient, in electric signal if passing through a collimator and being detected by a scintillation detector [20]. The major components are a collimator, a scintillation crystal, a light guide, an array of photomultipliers tubes (PMT), pulsed-height analyzer (PHA), an X-, Y-positioning circuit [12]. The main components are described below.

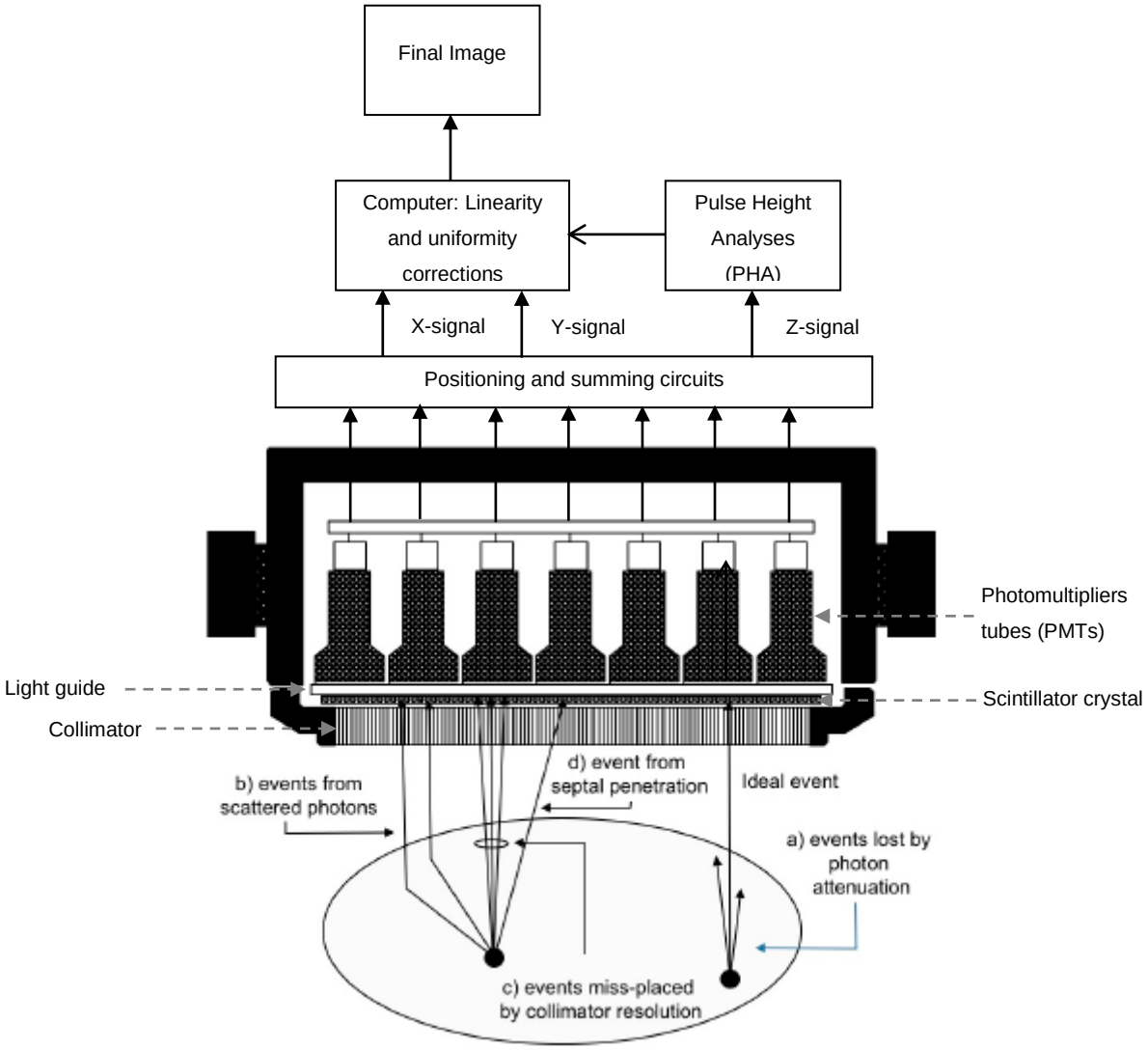

Figure 3 - Basic components of a scintillation camera (adapted from Ljungberg *et al,* 2016).

COLLIMATOR

The collimator is the first component of the gamma camera after the photons leave the patient and is used to define the direction of the detected γ-rays. The most common consist of a lead plate or a similar high atomic number substance and stopping power such as tungsten. They are designed in different sizes and shapes and contain a large array of holes (circular, triangular, square or more frequently hexagonal shaped) to view the area of interest. The purpose of the collimator is to permit that incident photos traveling along only certain directions, reaching the scintillation crystal and thereby providing a means to localize the site of the emitting sources. It is the image forming component of the Anger camera [15].

Collimators are primarily classified by the type of focusing, can be parallel-hole, pinhole, converging or diverging type. *Pinhole collimator* has a conic form with a single hole. Its main use is to give a significantly magnified image of a small organ such as the thyroid glands or heart. The organ must be located near a body surface so that the pinhole can be positioned close to it. There is a variation in resolution and sensitivity across an organ, and sensibility falls of quickly with increasing distance source-aperture [12]. *Parallel-hole collimator* is the most commonly collimator used in nuclear medicine procedures. This collimator is made with holes that are parallel to each other and perpendicular to the face of the collimator. The γ-rays image projected by this collimator has the same size as the source distribution onto scintillation crystal. *Parallel-hole collimator* are classified as low-energy, medium-energy or high-energy and high-resolution, all-purpose and high-sensibility. The characteristics of parallel-hole collimator such as septal thickness, septal length and size of collimator hole are chosen according to the energy of the radionuclide using for image [16]. *Converging collimators* are made with tapered holes converging to a point in front of the collimator and are provide magnified images. This collimator is employed when the organ of interest is smaller than the size of the detector. *Diverging collimator* has holes that diverge from the detector face. In opposite to the converging collimator, images of organ larger than size of the detector are minified (Figure 4) [16].

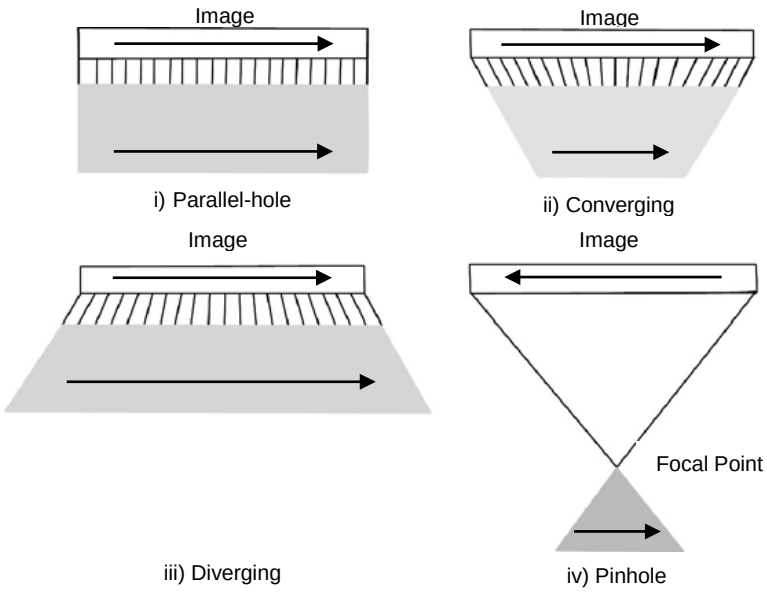

Figure 4 - Types of the gamma camera collimators: i) parallel-hole collimator, ii) converging collimator, iii) diverging collimator and iv) pinhole collimator (Adapted from Sharp *et al*, 2005)

SCINTILLATION CRYSTAL

The γ-rays that passed through the collimator interact with the detector. The detector used in gamma camera is a continuous scintillation crystal made from sodium iodine doped with a small amount of thallium, NaI(Tl) (Figure 5). The function of the NaI(Tl) crystal is to stop the gamma photons and convert these into visible light photons (scintillation) [15]. The choice of the thickness of the crystal is a trade-off between detection efficiency and image quality. Because increasing the thickness of a detector increases the probability of complete observation of γ-rays and hence the sensibility, but resolution of the image of the area the interest deteriorates. Also, the probability of multiple Compton scattering also increases in thicker detectors [16].

The amount of scintillation light produced following the interaction of a single gamma photon is proportional to the energy deposited by the incident photon and these optical photons are emitted isotropically from their point of creation. These photons deposit energy within the scintillation crystal by a photoelectric or a Compton scattering interaction. Therefore, the desired event is the photoelectric interaction where the entire energy of the photon is transferred to an electron and the photon ceases to exist. In a Compton scattering only a partial amount of the energy of the photon is transferred to the electron and the photon changes direction and loses energy. The visible light is then guided towards the photomultiplier tubes through the light guide increasing the light collection efficiency [12,15].

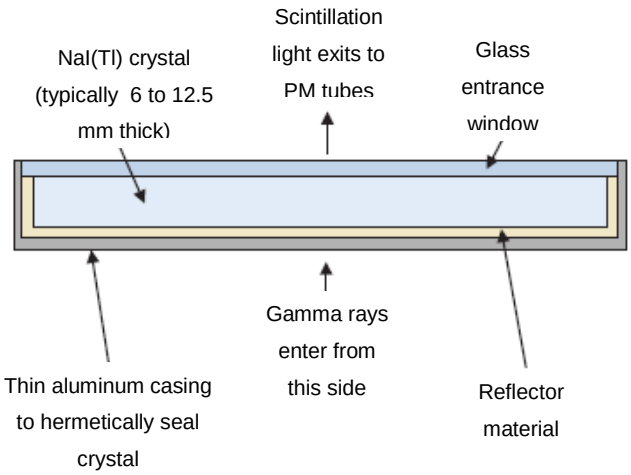

Figure 5 - Schematic cross-section of a NaI(Tl) crystal assembly for a gamma camera (adapted from Cherry *et al*, 2012)

PHOTOMULTIPLIERS TUBES (PMTs)

The photomultiplier tubes are fixed on the NaI(Tl) crystal with the photocathode facing the crystal by a special optical grease or connected to the crystal using light pipes. The PMTs are usually arranged in a close-packed array and are mounted in a hexagonal fashion to ensure that the smallest possible gaps are left between tubes [16]. The visible light photons collected by a particular PMT are converted into electrons, multiplied and converted into an electrical signal [15]. It amplifies the electronic signal (typically by a factor of 10^7) in order to generate a sufficiently large current to be received and processed by the subsequent electronics [21]. The output signal from PMTs are fed into positioning logic circuits or software which is used to define the X, Y location of the point of interaction of the γ-rays in the detector [16].

The amount of light photons detected by a PMT is inversely related to the lateral distance between the interaction site and the center of the PMT. The PMT closest to the point of interaction collect the largest number of light photons. Subsequently, it will have a largest output signal, with the amplitude of the signal output of the other PMT decreasing with increasing distance from the interaction point (Figure 6) [22].

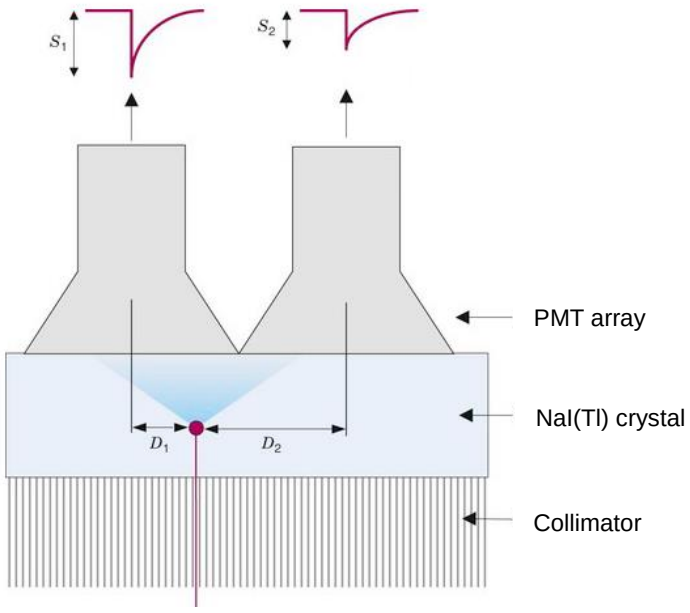

Figure 6 - Illustration of light photon sharing between PMTs. The PMT signal, S, is inversely related to the distance of the interaction site, D, from the center of the PMT (adapted from Cherry *et al,* 2012).

ELECTRONIC INSTRUMENTATION

The position information for an event on the crystal is used to form the 2D projection image and hence the final image depends of the distribution of signal amplitudes in the

PMTs. The location of the gamma-ray interaction can be estimated by the calculation of centroid of the position-weighted PMT outputs, a process often referred to as Anger Logic or Anger Arithmetic [22].

In analogue circuits the signals from PMTs are processed to give three signals required X, Y and Z. The X and Y provide spatial information the point of interaction of the γ-ray in the scintillation crystal by use an X-, Y-positioning circuit. The Z-signal is proportional to the total energy deposited in the crystal by a scintillation event produced simply by circuit the outputs from all the tubes. This electrical pulse is analyzed by a pulse-height analyzer (PHA) and is accepted if it falls within the range of selected energies [16,21]. The spatial information is more complex to generate. All PM tubes are connected through resistors and the position is determined by splitting the signal from each PMT onto four output lines (X^+, X^-, Y^+ and Y^-). The output signal from each PMT is determined by the appropriate resistor values and then summed to form each of the X+, X−, Y+, and Y− signals individually [12].

Also, these pulses can be stored in the computer. In modern camera systems, the output signal from each PMT is digitized and the event position is calculated in software. In digital cameras the analogue signal is required to be digitized. So, two general approaches are currently taken; the X, Y and Z signals are acquired in analog form and then digitized by analog-to-digital converters (ADC) to digital signals or the position signals and the total energy deposited being digitized before signals are computed. The position estimates are computed by combining only PMT with signals above a certain threshold. Therefore, with signal thresholding, only a small number of PMT surrounding the interaction location are used for position determination [16,22].

PULSE-HEIGHT-ANALYZER (PHA)

The summing circuit provides the energy signal (Z), which is proportional to the amount the light photons produced by a scintillation event in the crystal. After the Z pulses are formed by the summing circuit, each event is analyzed by pulse-height-analyzer (PHA). The PHA allows selecting only the Z signals where the gamma rays energy has a certain amplitude range of interest. This energy range is selected by use of appropriate peak and window setting, which is usually chosen according to the radionuclide being imaged [12,16].

A typical energy spectrum includes several peaks. A typical example is the ^{99m}Tc spectrum with a gamma ray of 140 keV and typically a window equal to 20% centered symmetrically on the photopeak is employed. In Figure 7 is possible see the different

features of this spectrum. The *photopeak* is the peak that corresponds to interaction in which the total energy of the γ-ray (140 keV) is absorbed in the scintillation crystal, whereas other peaks in the energy spectrum represent some loss of energy from the detection process and therefore will be to the left of the photopeak. The *Compton plateau* results from the Compton scattering in the scintillator or detector and scattered photons that escape from the detector. In this situation only a fraction of its energy is registered by the detector with a peak from 0 to E_{max}. The E_{max} that corresponds to the *Compton edge* is the kinetic energy of those photons that are produced by the 180° Compton backscattering of the γ-ray photons in the detector. In addition, Compton scattering occurs not only in the detector but also outside of the detector. Some scattered photons, created inside the patient may lose only a small amount of energy. In such cases, a γ-ray can travel toward the detector, its energy may fall between the photopeak and the Compton edge [16]. A *characteristic x-ray* is produced by photoelectric interaction of the γ-ray with the shielding or collimator. Because this interaction can cause injection of the k-shell electrons, followed by transition of electrons from the upper shells. The difference in binding energy between the levels appears as lead x-ray. The *backscatter peak* occurs when the gamma ray are scattered at 180º by Compton scattering in the source or surrounding structures and then absorbed in the crystal, appearing in the γ-ray spectrum [12]. *Iodine escape peak* results from photoelectric interaction with iodine atoms of the NaI(Tl) crystal where usually occurs emission of characteristic K x-rays. This peak appears about 28 keV below the photopeak [12].

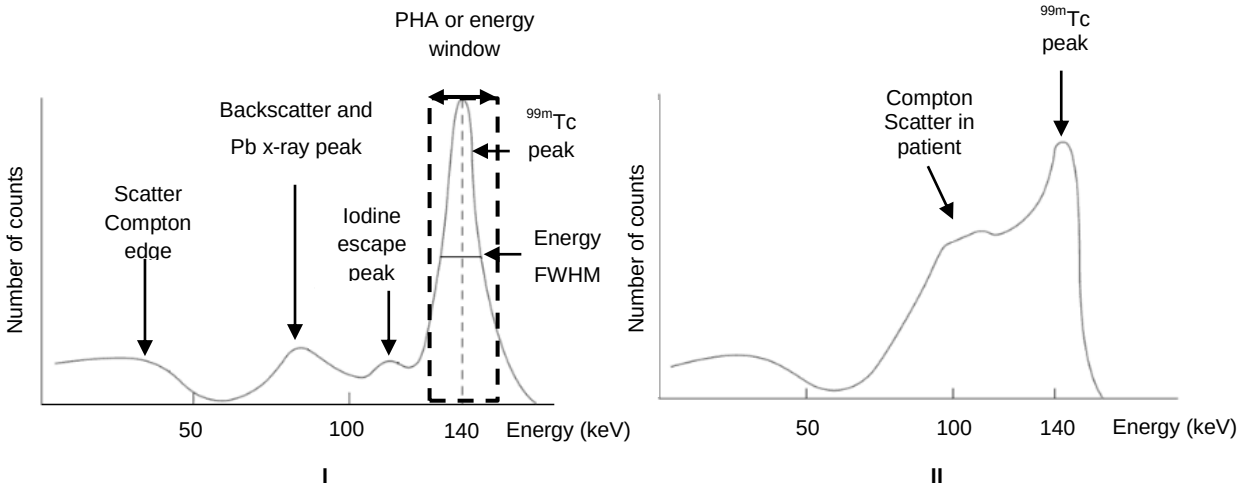

Figure 7 - Energy spectrum of the ^{99m}Tc showing the location of the Compton edge and effect of scatter. I) Spectrum obtained with a gamma camera of point source. II) Spectrum obtained with a gamma camera from patient (adapted from Prekeges, 2013).

2.1.3.1. Planar Imaging

In planar imaging, the final images are a three-dimensional (3-D) distribution of the radioactivity as a two-dimensional (2D) projection. This results in an image with little depth information where structural information is obscured by superimposition of all photons emitted along projections lines. Thus, photons emitted also from overlying and underlying activity along the projection lines will contribute to the signal recorded in a particular pixel. This generally reduces the image contrast in the plane of interest. The problem can be minimized by obtaining multiple planar views (posterior, anterior, lateral, oblique) giving some information about the depth of a structure. For this reason, a 3-D imaging technique has been developed to tackle the problem directly [16,20].

2.1.3.2. Single photon emission computed tomography

SPECT imaging requires two fundamental components: a gamma camera and a means of performing image reconstruction [22]. The tomographic mode of single photon imaging (SPECT) is based on detecting individual photons emitted isotropically by the radionuclide. The gamma camera rotates around the long axis of the patient to acquire multiple projection images at equal spaced angular intervals for collection of data over 180º or 360º. The data are collected in the form of pulses at each angular position and normally stored in a 64 × 64 or 128 × 128 matrix in the computer. As result provide a series of the static images at distinct depths of the organ of interest for later reconstruction [12,16].

The idea behind tomography is to recreate the depth information along the projection line, in order overcome the problems of superimposition of radioactivity. Nevertheless, this can only be properly accomplished if certain requirements are followed: (i) a complete set of projections is acquired, (ii) the internal distribution is not spatially or temporally changing during the time that the projections are acquired, (iii) the detectors that acquire the projections have uniform detection sensitivity that remains constant throughout the acquisition, and (iv) the acquired projections have a common center and its accurate location is required for proper alignment of the projections during reconstruction [23].

Older cameras were initially designed to rotate in circular orbits around the body. This causes loss of data and rapid degradation in spatial resolution with increasing distance of the object from the collimator. To circumvent this problem, many SPECT systems allow the detector head to trace out elliptical rather, permitting that the detector to pass

closer to the patient than would be the case with circular orbits, which can lead to significant improvements in spatial resolution (Figure 8) [12,16].

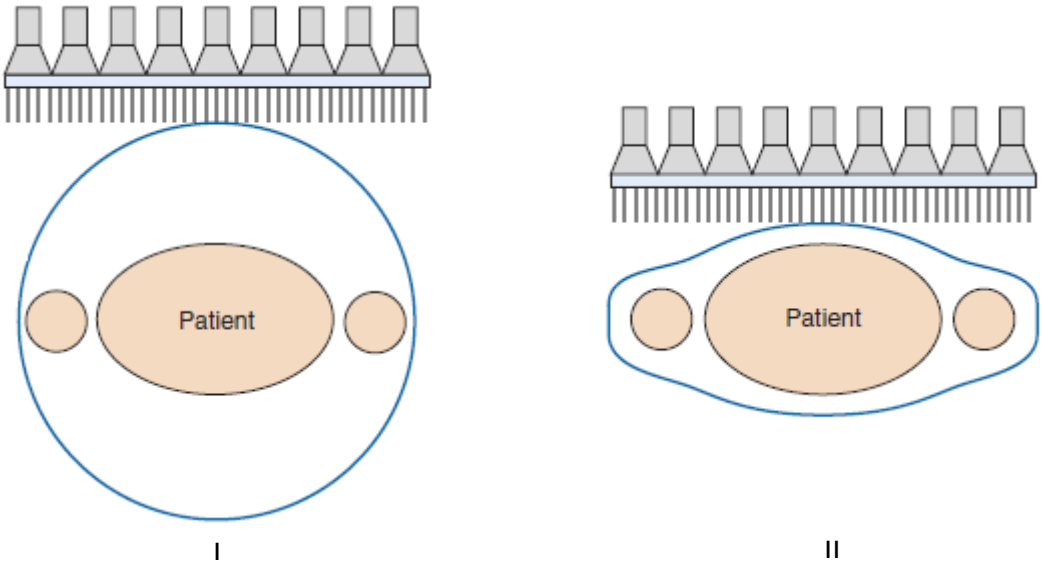

Figure 8 - Illustration of circular (I) and contoured (II) orbits for SPECT imaging (adapted from Cherry *et al*, 2012).

In a reconstruction, it is assumed that the activity distribution remains stationary throughout the acquisition. However, it is important to note that the information collected by SPECT systems is not linearly related to the ray sums of activity in the patient because of tissue attenuation. This means that the difference in spatial distribution of counts in the acquired projection images limit the quality of reconstructed images. The advances in SPECT are directly knotted to improving the quality and accuracy of the acquired projections either through better instrumentation or reconstruction method [20,23].

2.1.3.2.1. Reconstruction methods

A basic problem in conventional radionuclide imaging is that the images obtained are 2D projections of 3D source distributions. To obtain information along the depth of the organ of interest, tomographic images are used to calculate transaxial slices using mathematical algorithms [24]. Reconstruction mathematical algorithms, such as filtered backprojection (FBP) method or an interactive reconstruction algorithm are two common methods of image reconstruction using the acquired data. In the past, the filtered backprojection method was the golden standard of reconstruction methods, but nowadays, due to the promise of better image quality in an acceptable time interval due to an increase in computer performance, iterative reconstruction methods are preferred

alternative methods for performing SPECT (and other tomographic image acquisitions) reconstruction [23]. Both methods are described below.

Before discussing reconstruction methods, it is necessary to introduce some general concepts. Assuming that the data is acquired by a dual-head gamma camera fitted with a conventional parallel-hole collimator with heads counted in opposition (i.e. 180º), the 3D dataset of γ-emitter distribution is obtained by pilling up many slices usually reconstructed independently. For this, the detector rotates around the organ of interest and allows one to observe the pattern of γ-emission in the field of view for many angles Figure 9 [25].

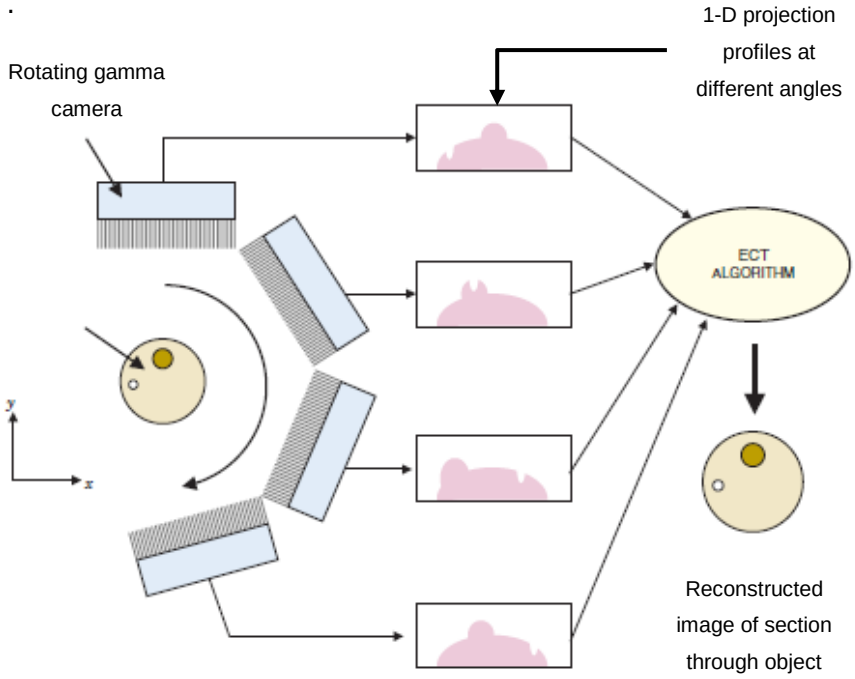

Figure 9 - Rotating the gamma camera around the object provides a set of 1-D projection profiles for a 2D object, which are used to calculate the 2D distribution of radioactivity in the object. ECT, emission computed tomography (adapted from Cherry *et al*, 2012).

For the purpose of analyses, it is convenient to introduce a coordinate system (Figure 10 - The (r,s) coordinate system is rotated by projection angle φ with respect to the (x,y) coordinate system of the object and is fixed with respect to the gamma camera (adapted from Cherry *et al*, 2012). that is stationary with respect to the gamma camera detector. Defining *(r, s)* as the estimated number of photons emitted at any point *(x, y)*, of the transverse slice in the field of view. And If the camera is rotated by an angle φ with respect to the *(x, y)* coordinate system of the scanned object, the equations for transformation from *(x, y)* to *(r, s)* coordinates can be derived from the principle of similar triangles and are given by:

$$r = x\cos\varphi + y\sin\varphi \quad \text{Equation 13}$$

$$s = y\cos\varphi + x\sin\varphi \quad \text{Equation 14}$$

These equations can be used to determine how radioactivity at a location *(x,y)*, for each detector angle φ, and for each location *r* on the detector. Because the collimator allows only photons whose direction is parallel to the axis of its holes to be potentially detected. [25].

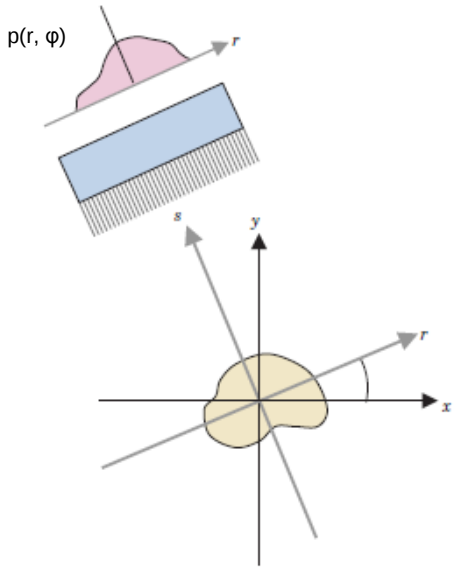

Figure 10 - The (r,s) coordinate system is rotated by projection angle φ with respect to the (x,y) coordinate system of the object and is fixed with respect to the gamma camera (adapted from Cherry *et al*, 2012).

A common representation of the matrix *p(r, φ)* is generically known as a *sinogram* (Figure 11). A sinogram is a 2D image, in which the horizontal axis represents the count location on the detector, and the vertical axis corresponds to the angular position of the detector. The successive rows from top to bottom represent successive projection angles. The sinogram provides a convenient way to represent the full set of data acquired during a scan and can be useful for determining the causes of artifacts in SPECT image. For example, this should demonstrate the smooth progress of the camera head around the patient and any discontinuity indicates patient movement [12,25].

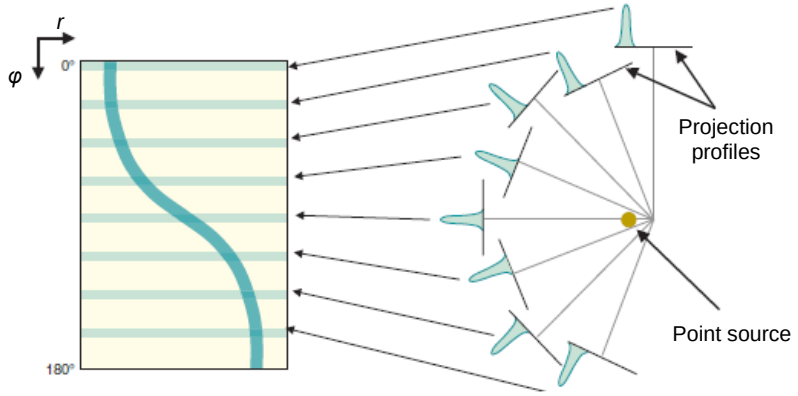

Figure 11 - Sinogram. Each row of sinogram is projection of slice at given angular position of detector (adapted from Cherry *et al*, 2012).

FILTERED BACKPROJECTION

Filtered backprojection (FBP) is a modification of an older technique, called backprojection or simple backprojection. Simple backprojection is a common sense approach, but much unsophisticated. The principle of simple backprojection is illustrated in Figure 12 in which a point source object is acquired from different angles. An image of the original distribution is by "backprojecting" each profile at the appropriate angle on to an image array in the computer. An approximation for the source distribution within the scanned slice is obtained when all projection profiles acquired are added together [12].

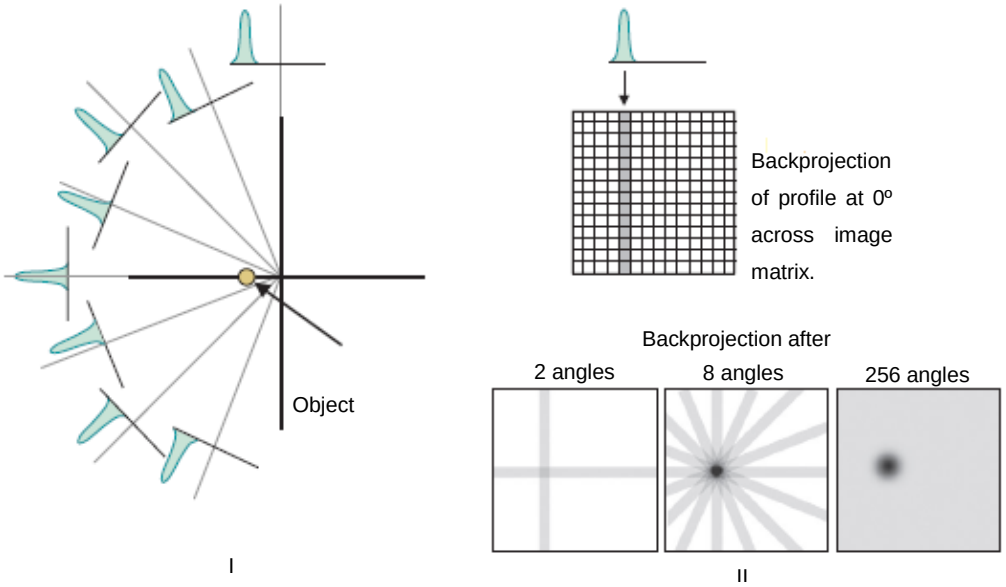

Figure 12 - Basic principle of image reconstruction by the backprojection algorithm. (I) Projection profiles for a point source of radioactivity for different projection angles. (II) Backprojection of one intensity profile across the image at the angle corresponding to the profile. This is repeated for all projection profiles to build up the projected image (adapted from Cherry *et al*, 2012).

However, when the number of projections is small relative to the matrix size, there is a "star-pattern" artifact resulting from counts that inevitably are projected outside the true location of the object, causing a blurring final image [25]. Mathematically, the relationship between the real image and the image reconstructed by simple backprojection is described as:

$$f'(x,y) = f(x,y) \times \frac{1}{r} \quad \text{Equation 15}$$

This way, the blurring effect can be reduce by increasing the number of acquired projections and by decreasing the distance (*r*) from the object of interest [12]. In addition, this problem can be minimized by filtering the profiles prior to backprojection and, the filtered projections are then backprojected to produce an image that is more representative of the original object [16].

It is important to understand that nuclear medicine data is obtained in the spatial domain. And, the frequencies of an image are similar to the frequencies of a sound, where the data for each row and column of the acquisition matrix can be considered as composed of sinusoidal waver of varying amplitudes and frequencies. Thus, using the mathematical technique known as Fourier analysis, it is possible to describe images in terms of their spatial frequencies. The Fourier method of filtering the projection data in the Fourier domain is based on the initial transformation of these data from the spatial domain, represented by $f(x,y)$, to the frequency domain, $F(k_x,k_y)$, which is denoted as [12,16,25]:

$$F(k_x,k_y) = \mathcal{F}[f(x,y)] \quad \text{Equation 16}$$

Finally, the operation of converting the *Fourier transform* (*FT*) of a function back into the original function is called an *inverse FT* and is expressed as [12]:

$$\mathcal{F}^{-1}[F(k_x,k_y)] = f(x,y) \quad \text{Equation 17}$$

In this method, filters are used to eliminate the blurring function *1/r* that arises from simple backprojection of the projection data. The idea is apply a Fourier filter applied in k-space before perform the *inverse FT*. In nuclear medicine, a number of Fourier filters have been designed and used in the reconstruction of image. In common, it have the called Nyquist frequency, that gives an upper limit to the number of frequencies necessary to describe the sine or cosine curves representing an image projection [16].

A well-known filter is the ramp filter (Figure 13), which gives a weight proportional to its frequency to each of the components. This filter will enhance the higher spatial frequencies, the aim being to restore higher spatial frequencies lost by the back-projection process. However, this can also be a problem, because the noise associated with high frequencies in the image is amplified. In addition, the ramp filter to suppress low spatial frequencies that help to removes the blurring effect of simple backprojection [12,16].

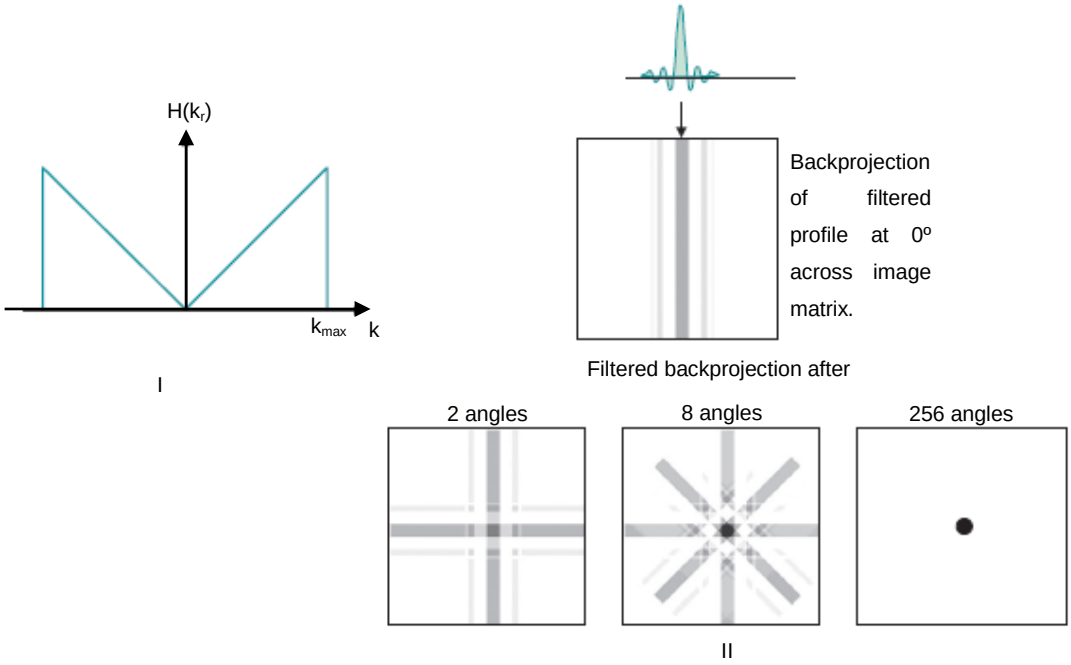

Figure 13 - (I) Ramp filter in the spatial-frequency (k-space) domain. (II) Illustration of the steps in filtered backprojection. The 1-D Fourier transforms of projection profiles recorded at different projection angles are multiplied by the ramp filter. After taking the inverse Fourier transform of the filtered transforms, the filtered profiles are backprojected across the image, as in simple backprojection (adapted from Cherry *et al*, 2012).

To eliminate the high-frequency noise, a window is applied to the ramp filter. The effect of a decreasing window at higher frequencies is to eliminate the noise associated with them. The frequency above which the noise is eliminated is called the cut-off frequency. The typical cut-off frequencies vary from 0.2 to 1.0 times the Nyquist frequency, being that the Nyquist frequency is the highest cut-off frequency. The choice this frequency should be a compromise between noise reduction and image details preserved, because with a very high cut-off value, image detail may be lost [16].

To minimize these effects on signal-to-noise ratio (SNR) and artifacts at sharp edges a variety of reconstruction filters have been developed, each with its own theoretical rationale. Hann, Hamming, Parzen, and Shepp–Logan filters are all low-pass filters because they preserve low-frequency structures, while eliminating high frequency

noise. Butterworth filter is an important low-pass filter that is most commonly used in nuclear medicine. This filter has two parameters: the cut-off frequency (f_c) and the order (n) [16]. The cut-off frequency defines the frequency at which the filter attenuates the amplitude, which for the Butterworth filter is 0.71. One has to be aware of the fact that, by limiting the frequency content of an image, not only is noise is reduced, but also useful information may be lost. The order of the filter allows changing the slope of the filter function that is determines how rapidly the attenuation of amplitudes occurs with increasing frequencies. Thus, the higher the order, the greater the slope. No filter is perfect and, therefore, the design, acceptance, and implementation of a filter are normally done by trial and error with the ultimate result of clinical utility [26].

ITERATIVE RECONSTRUCTION

FBP has some limitations due to the presence of streak artifacts that are particularly prominent near hot structures and the noise enhancement that is inherent in the reconstruction. An alternative to FBP is the use of *iterative reconstruction* techniques, which can more readily incorporate more complex models of the underlying physics and also can better accommodate assumptions regarding the statistical variability of acquired data. As this method is more complex, is also computationally more intensive than FBP.

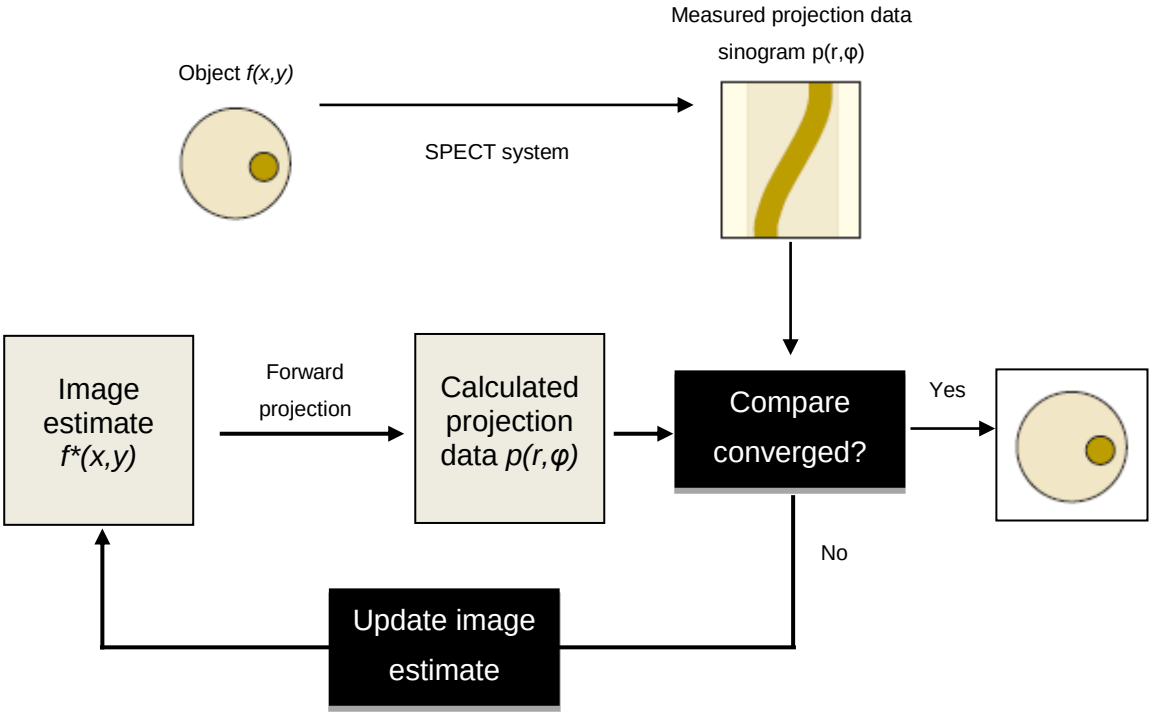

Figure 14 - Schematic of general iterative reconstruction algorithm (adapted from Cherry *et al*, 2012).

The general concepts of iterative reconstruction are outlined in Figure 14. The basic principle of the iterative reconstruction is to find a solution by successive estimates until a satisfactory agreement is achieved [12]. This method tries to determine the “best” estimate of the distribution of activity comparing the estimated image with the measured image. The iterative algorithm involves a feedback process that permits sequential adjustment of the estimated reconstruction so as to improve its correspondence with the measured projections. In practice, a first estimate of the internal source distribution is made and the computer algorithm calculates a projection image (sinogram), using a process called forward projection. This image is then compared with a measured projection to determine where in the modeled image differences occur. As the first result will differ from the actual measured projections, unless the initial guess happens to coincide exactly with the actual object. However, the difference between the estimated and actual projections can be used to adjust the estimated image to achieve closer agreement. This proceeds as the first with the forward projection so as to re-estimate the projections that would derive from this updated object. The successive adjusts led that the estimated image progressively converges toward the true image [12,27].

Most reconstructions in nuclear medicine use the statistical iterative reconstruction methods such as the Maximum Likelihood Expectation Maximization (MLEM) method and Ordered Subsets Expectation Maximization (OSEM) method. The MLEM method basically consists in obtaining the parameters that maximize the likelihood of the statistical model given any outcome. This method requires much iteration to achieve a satisfactory agreement between the estimated and measured images and, between iteration updates the image, demanding a lengthy computation time. A version of the MLEM algorithm is the OSEM, which, due to the improved calculation efficiency, has made the iterative reconstruction methods practical for clinically routine studies. With OSEM, the projection data is grouped into an ordered sequence of subsets separated by some fixed angle. For each subset, MLEM is applied and the expected projection values are computed from the estimation of the pixel values in all projections in the subset and compared with the measured image. However, in OSEM the estimated image is updated, that is, the first full iteration is complete, after only a subset of uniformly-distributed angles has been processed. This means that, in each sub-iteration, instead of computing all projection data, only the projection data in subset are computed in the forward projection. The OSEM method considerably shorten the computing time needed for reconstruction, thus, the convergence rate is reached much

faster and with an accelerating factor, relative to the MLEM algorithm, roughly equal to the number of subsets [16,20,25].

2.2. Radionuclide Therapy

The nuclear medicine therapy is required to be highly specific and targeted, since it involves administration of unsealed sources of radioactivity. The concept of targeted radionuclide therapy (TRT) is like chemotherapy as it is a systemic treatment, bring about by injection radioactive substances into the blood stream [28]. The method of TRT uses radionuclide pharmaceuticals that allow deliver therapeutic doses of radiation directly to the targeted site of disease with potentially less toxicity from exposure of normal tissues. One of the most appealing benefits of TRT is the possibility for personalized medical care, optimized for patient and disease characteristics patient and disease characteristics [29,30]. However, the efficiency of the TRT relies on the delivery of the radiopharmaceutical to the intended tumor site. When the radiopharmaceutical is effectively delivered, it is retained on those tissues and decays for a certain period of time, emitting a prolonged radiation dose to kill cancer cells and minimize tumors by damaging the cells' DNA, thereby stopping these cells from continuing to grow and divide [31].

The biological effect in the target radionuclide therapy depends of energy absorbed from the radiation emitted by the radionuclide. In nuclear medicine imaging, the radionuclides used emit gamma rays, which can penetrate profoundly into the body. The radionuclides used for target radionuclide therapy should emit radiation with a relatively short path length to must irradiate tissue volumes with multicellular, cellular and subcellular dimensions. There are three types of particles radiation possible for radionuclide therapy that is beta (β) particles, alpha (α) particles and Auger electrons.

2.2.1. Radionuclides Selection

Such as in nuclear medicine imaging, in which the radionuclides have some specific characteristics, also the radionuclides for targeted therapy must comply with several requirements. The selection of the therapeutic radionuclide for clinical usage depends on several factors such as type of emissions, energy of the radiation, half-life, method of production, radionuclide purity and cost [28,31–33].

Physical and effective half-life of the radioisotope should be paired to the drug half-life in the body is an important factor for the therapy planning. An optimal half-life for

isotopes used for radionuclide therapy ranges from six hours to seven days. Radioisotopes with very short half-life limits the preparation of pharmaceutical flexibility, its transport and delivery storage and patient transportation, while radionuclides with longer half-life promote an increase to absorbed dose not only in the target tissue, but also in the surrounding areas. Therefore, for an efficient radiation delivery, a balanced optimal biological and physical half-life should be chosen, so that the resulting effective half-life be an appropriate time for maximum therapeutic effect and minimal radiation risks and toxicity for the health cells [31–33].

For therapeutic purposes, the radioactive decay of radionuclides is expected to cause significant damage to cancer cells and the action is determined by the form of ionizing radiation emitted by the radionuclide. This damage is mediated by the linear energy transfer (LET), which is defined as the rate of energy loss by the radiation (dE_L) in the medium per unit distance (dl):

$$\boldsymbol{LET = \frac{dE_L}{dl}} \qquad \textbf{Equation 18}$$

LET is an important parameter for understanding energy deposition effects on living cells [34]. Potentially, radionuclides that emit α, β particles and Auger electron are assumed to display the highest therapeutic efficiency, because these types of radiations allow very high ionization in extremely short path length. Seeing that, they are fully deposited within a small range of tissue, usually a few millimeters [31,33].

The specifications of the radionuclide chosen for a give application will depend on many others factors that include the type of disease to be treated, the accessibility of the disease site, the target and the biochemical mechanism addressed, pharmacokinetic of the radiopharmaceutical as well as the availability and cost of the radionuclide [35].

The Auger electrons is the low-energy electrons (<1 keV) that result of the internal emitters that undergo radioactive decay by electron capture (EC) and/or internal conversion (IC). The very low energies of Auger electrons have two important consequences that become less clinically efficient. First, they emit the particles dispersed form and in a short range (<1 nm to a few μm), requiring their close proximity to the radiosensitive target (DNA) for radiotherapeutic effectiveness. Second, the linear energy transfer for Auger electrons varies between 4 – 26 keV/μm, that is, multiple ionizations occur around of the decay site. These characteristics make the radionuclides that emit Auger electrons more suitable for the treatment of small groups

of cancer cells or small tumor deposits. It is worth that the radionuclides producing Auger effects on electron capture are often used for diagnostic purposes, as is the case of ^{99m}Tc [28,33,36–38]. The α-particles, which are ^{4}He nuclei, have high linear energy transfer values (80 – 100 keV/µm), the path length is in the range of 50-100 µm for mean energies of around 5 – 8 MeV. These properties render α-emitting isotopes highly efficient for therapeutic purpose due to it is capability to deliver a higher radiation dose at cellular level. Because of the high LET and short path length the induction of irreparable damage in DNA is very probable, since the ionizing events occur in the range of about 2 nm, close to the diameter of DNA double helix. In α therapy, high degree of accuracy is required to deliver the radiation to the target cells without targeting healthy cells, for once the double-stranded DNA molecules break, there is very little chance for repair [28,31,33,38]. In current clinical treatment the β-emitting isotopes are most widely used for TRT at present. β-particles are negatively charged electrons that are emitted from nucleus of decaying radioactive atom (1 electron/decay). After emission, the daughter nucleus has 1 more proton and 1 less neutron. The range of β-particles in tissue is 0.05 to 12.0 mm and has wide energies range (50 – 2300 keV). Due to the range of these particles most of their energy is dissipated within an organ, being is indicated for the treatment of larger tumors. In addition, the LET of these energetic particles is low (0.2 – 2.0 keV/ µm), which causes less damaging than high LET radiation, as is the case of the α-particles and Auger electrons (Figure 15) [31,37,38]. An important consequence of the relative long range of emitted electrons is the production of *cross-fire*, where the β electrons energy is deposited in neighboring, non-target cells, is due to the larger range of β-particles in the soft tissue. The main advantage of *cross-fire* is that negates the necessity of the radiotherapeutic agent to target every cell within of tumor; but it has the disadvantage of delivering a significant dose to adjacent normal tissue that can be destroyed [28,37,38].

Some therapeutic β-emitting nuclides produce Bremsstrahlung radiation and could have different energies and intensities. This associated gamma (γ)-radiation could be advantageous if the energy and intensity are within the diagnostic range (100 – 200 keV) because is possible following the pharmacokinetics as well as in vivo localization of the radiopharmaceutics as a function of time by using gamma scintigraphy methods. The γ-radiation contributes very little to therapeutic effectiveness [38].

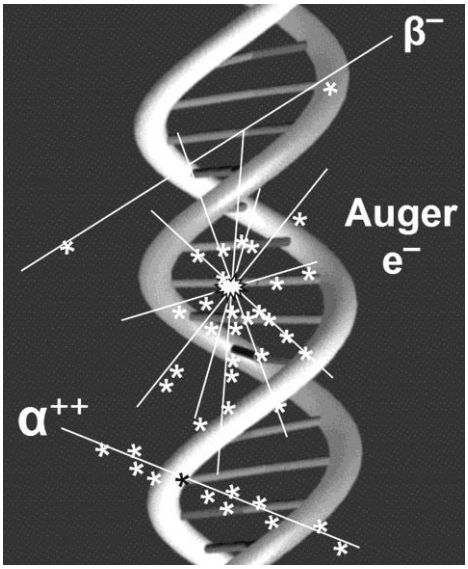

Figure 15 - Local density of ionization produce along track of energetic β -particles, Auger electrons and α-particles [38].

In some cases, mixed emitters are used to allow both imaging and therapy with the same radionuclide, as is the case of ^{131}I, which emits the mixed beta/gamma particles. Moreover, for each type of particles, there are multiple radionuclides with a variety of tissue ranges, half-lives and chemistries, offering the attractive possibility of tailor-making the properties of a target radionuclide therapeutic to the needs of an individual patient [39].

2.2.2. Radionuclide Application

For many decades, radionuclide therapy was one of the most intensively developing directions of nuclear medicine. The target radionuclide therapy is based on the use of molecular carriers of radionuclides with high affinity to tumor cells and, the choice of radionuclide depends on the tumor characteristics. The development of radionuclides such as iodine-131 (^{131}I), phosphorous-32 (^{32}P), strontium-89 (^{89}Sr), lutetium-177 (^{177}Lu), radium-223 (^{223}Ra) and yttrium-90 (^{90}Y) emit charges particles with therapeutic effects and also allow *in vivo* imaging. These radionuclides in therapy have been used successfully for the treatment of metastatic bone pain, neuroendocrine and other benign or malignant disease [30,31,33,37,40].

Radioactive iodine labeled with sodium iodine (^{131}I-NaI), in capsule or liquid form, is commonly used in different thyroid disorders such as Graves' disease, hyperthyroidism, or even, to reduce the thyroid volume [30,33,37,41]. ^{131}I has also been used

for treatment of patients with differentiated thyroid cancer and generally done post-surgical removal of the solid tumor. The radioiodine ablation it seeks to eliminate thyroid remnants and consequently evaluate the differentiated thyroid cancer persistence or recurrence through of diagnostic whole-body scintigraphy [35,42]. With a physical half-life of 8.02 days and with the maximum and average beta particles energy of 0.61 keV and 0.192 keV, respectively, the ^{131}I has suitable characteristics for therapy. However, the abundance of high energy gamma photon (364 keV – 81% and 636 keV – 7.27%) present in the ^{131}I deposits unnecessary dose to surrounding tissues [35,41].

Others pharmaceuticals for TRT with ^{131}I component are introduced in clinical practice. ^{131}I-tositumomabar (Bexxar®) was used to treat certain types of non-Hodgkin's lymphoma. Bexxar® was approved by the USA's Food and Drug Administration (FDA) in 2003. However, in 2014 was taken out of production because of commercial reasons [30,31,33]. Meta-iodobenzylguanidine labeled with ^{131}I (^{131}I-mIBG) have indications to be used in treatments such as pheochromocytoma, paraganglioma, neuroblastoma, carcinoid, medullary thyroid carcinoma. The therapy is administered for intravenous infusion [33,43,44].

Bone pain is caused by skeletal metastases associated with prostate and breast cancer, in about 80% of the cases. Radionuclide therapy has played an important role in palliation of painful bone metastases that reduces the patient quality of life [33,45,46]. There are a number of options of radionuclides, ^{89}Sr chloride (Metastron®), ^{32}P, ^{153}Sm-EDTMP (Quadramet®) and ^{186}Re-HEDP. Strontium is chemically similar to calcium and hence mimics the metabolism of calcium and is associated with rapid washout form normal bone and prolonged retention in diseased bone [35,45,46]. ^{32}P as phosphoric acid was one of the earliest be used how therapeutic radiopharmaceutical for bone pain palliation. Like ^{89}Sr (1.497 MeV), ^{32}P (1.711 MeV) presents hard beta energy, which can induce bone marrow toxicity to the patients. Meanwhile, other isotopes with lower energy have been developed such as ^{153}Sm-EDTMP. The beta energies of ^{153}Sm (808 keV – 17.5%, 705 keV – 49.6% and 635 keV – 32.2%) have the advantage over ^{89}Sr due to low bone marrow involvement. However, the ^{153}Sm is not a pure β emitter with a gamma abundance of about 35% (103 keV – 28.3% and 70 keV – 5.25%) capable of producing imaging of the distribution [32,35,45–47]. The first approved α emitting radiopharmaceutical was ^{223}Ra dichloride (Xofigo®; Bayer Healthcare Pharmaceutical). The ^{223}Ra selectively targets bone metastases with α particles and the results are promising increasing overall survival [30,48].

^{32}P therapy has been an accepted treatment for myeloproliferative disease for more than 30 years. The therapy is proposed for a group of elderly patients with polycythaemia vera characterized by an absolute increase in red blood cell mass, and essential thrombocythaemia characterized by unremitting thrombocyte elevation [32,35,49].

^{177}Lu-labeled radiopharmaceuticals have several therapeutic applications. ^{177}Lu is a medium-energy β-emitter (0.5 MeV) with low abundance of γ-rays (113 keV – 3% and 208 keV – 11%) offering the possibility to perform diagnostic imaging. The lower tissue penetration range of ^{177}Lu (maximum range of 2.1 mm) shows to be advantageous for the treatment of small tumors [32,33,40,50]. In the literature has been reported the success employed in labeled somatostatin analogues with ^{177}Lu offering an opportunity to treat receptor-positive tumors [45,46]. At present, are available [^{177}Lu-DOTA]-Phe^{1}-Tyr^{3}-octretide (^{177}Lu-DOTATOC), [^{177}Lu-DOTA]-Tyr^{3}-octreotate (^{177}Lu-DOTATATE), among others [35,46,50–53]. Monoclonal antibodies have also been successfully radiolabeling with it, for example the CC49, which reacts with a wide range of human carcinomas [35].

^{90}Y is an attractive choice for radionuclide therapy and there are several well established radiopharmaceuticals that incorporate it. The high energy β-emitter and longer path lengths of ^{90}Y may be preferable for treating larger tumors [33,50]. Such as ^{177}Lu, also ^{90}Y labeled with DOTA conjugated somatostatin analogues (e.g. [^{90}Y-DOTA]-Phe^{1}-Tyr^{3}-octreatide and [^{90}Y-DOTA]-lanreotide) has been used for peptide therapy in neuroendocrine tumors (NET) patients [31,33,35,40,46,50]. In 2002, the USA's Food and Drug Administration (FDA) approved the first pharmaceutical for radioimmunotherapy (RIT), Zevalin®. Zevalin is based on a monoclonal antibody targeting the CD20 antigen, ibritumomab, conjugated with ^{90}Y by the metal chelator tiuxetan (^{90}Y-ibritumomab tiuxetan). CD20 is one of many antibodies expressed on the mature B-cells. ^{90}Y-ibritumomab tiuxetan has been used as a radioimmunotherapeutic agent for the therapy of follicular B-cell non-Hodgkin's lymphoma [31,33,40,54]. The FDA requires that be performed a pre-therapeutic whole-body scan using ^{111}In- ibritumomab tiuxetan to confirm the biodistribution of ^{90}Y-ibritumomab tiuxetan [54].

Liver is a common site for metastasis from many primary neoplasms. For example, since almost the whole venous blood of the gastrointestinal tract first flows through the liver can be frequently found colon cancer metastasis. But, primary liver cancer (hepatocellular carcinoma or cholangiocarcinoma) also are recurrent. A treatment option is the selective internal radiation therapy (SIRT). This treatment is in particular related to patients whose liver tumors are not resectable or do not adequately

responding to chemotherapy. SIRT is based on the administration of ^{90}Y-resin (SirSpheres®, Sirtex Medical, Lane Cove, Australia) or ^{90}Y-glass (TheraSphere®, MDS Nordion, Kanata, ON, Canada) microspheres directly into the tumor tissue of the liver by means of femoral or radial catheter application. ^{90}Y-microspheres are delivered in aqueous solution and the radioactive contamination is a concern, therefore be considered as open sources [40,55,56]. As in Zevalin treatment, a pretherapy evaluation must be carried out, in this case, with ^{99m}Tc labeled albumin macroaggregate (^{99m}Tc-MAA) [56].

Several pharmaceuticals for TRT are available for clinical practice. Table 2 shows a summary of the physical characteristics, and clinical indication of the commonly available therapeutic radionuclides [31,33,35,45].

Table 2 - Radionuclides useful in targeted radionuclide therapy.

Nuclide	Physical Half-life ($\sigma_{1/2}$)	Mode decay	Maximum E (MeV)	Principal Eγ (MeV)	Maximum range in tissue (mm)	Radiopharmaceutical	Disease
^{32}P	14.3 days	β^-	1.71	-	7.9	^{32}P phosponate	Polycythemia vera, essential thrombocythaemia
^{89}Sr	50.5 days	β^-	1.49	-	7.0	^{89}Sr chloride (Metastron®)	Painful bone metastasis
^{90}Y	64.1 hours	β^-	2.28	-	11.3	^{90}Y-DOTATOC	Neuroendocrine tumors
						^{90}Y-ibritumomab tiuxetan (Zevalin®)	Non-Hodgkin's lymphoma
						^{90}Y-microspheres	Liver Metastasis; hepatocellular carcinoma
^{131}I	8.1 days	β^-, γ	0.61	0.364	2.3	^{131}I sodium iodine	Differentiated thyroid carcinoma
						^{131}I-tositumomab (Bexxar®)	Non-Hodgkin's lymphoma
						^{131}I-MIBG	Neuroblastoma; Pheochromacytoma; Carcinoid; Paraganglioma; Medullary thyroid carcinoma
^{153}Sm	46.3 hours	β^-, γ	0.81	0.103	3.0	^{153}Sm-EDTMP (Quadramet®)	Bone pain palliation
^{177}Lu	6.73 days	β^-, γ	0.5	0.113 and 0.208	1.8	^{177}Lu-DOTATOC ^{177}Lu-DOTATATE	Neuroendocrine tumors
^{186}Re	3.8 days	EC, β^-	1.08	0.137	4.8	^{186}Re-HEDP	Painful bone metastasis
^{188}Re	17 hours	β^-, γ	2.12	0.155	10.4	^{188}Re-HEDP	Painful bone metastasis
^{223}Ra	11.44 days	α, β, γ	5.98	0.154	< 10	^{223}Ra dichloride (Xofigo®)	Bone metastasis

2.3. Characteristics of ^{90}Y emission

Yttrium-90 is an important radioisotope, essentially β-particles emitter with a physical half-life of 2.67 days (64.2 h), and averages electron energy of 0.935 MeV and a maximum energy of 2.3 MeV. The average penetration range in soft tissue is 2.5 mm and maximum range is 11 mm, and 90% of the emitted energy is absorbed within a sphere with a radius of 5.3 mm [57–59]. The convenient physical characteristics as well as its availability from a ^{90}Sr/^{90}Y generator make it a very attractive choice for developing agents for radionuclide therapy. Currently, has found commercial application in ^{90}Y-microspheres for hepatic radioembolization [29,56,60].

The isotope ^{90}Y can the produce by the irradiation of ^{89}Y in a reactor by the ^{89}Y(n,γ)^{90}Y reaction and through the decay of ^{90}Sr. The feasibility of production of ^{90}Y from a ^{90}Sr/^{90}Y generator is more favorable, because makes this radionuclide should be readily available in sufficient quantities. The decay scheme of ^{90}Sr to ^{90}Y is show in Figure 16. The ^{90}Sr decays completely by β^- decay with no accompanied γ-radiation ($\sigma_{1/2}$ = 28.78 years, E_β = 0.546 MeV). The daughters ^{90}Y also decay by β^- decay and without accompanied γ-emission [28,35].

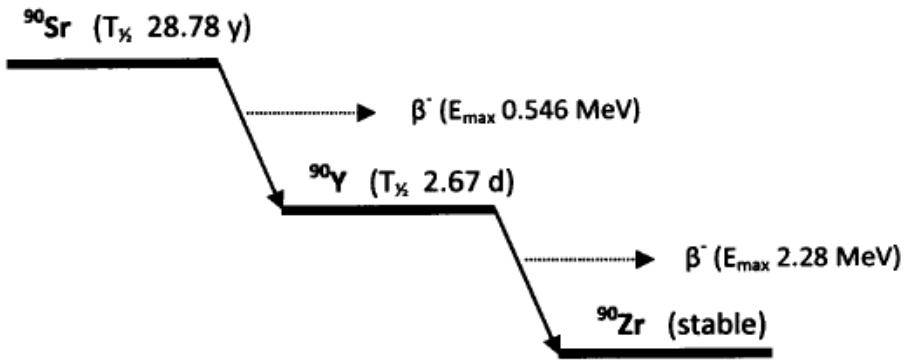

Figure 16 - Decay scheme for ^{90}Sr/^{90}Y [35].

A characteristic of ^{90}Y, suitable for therapy, to be considered is that ^{90}Y decays over 99.99 % of the time via β^- decay to the ground state of ^{90}Zr. Although ^{90}Y decay does not result in γ-emissions, it does produce secondary photons – *Bremsstrahlung photons* [56,58,61]. The Bremsstrahlung photons are broad-spectrum secondary γ-ray emissions that result of the interaction of high energy β-particles emitted by ^{90}Y with tissue [62]. The quantitative the imaging of ^{90}Y Bremsstrahlung photons can be obtained using a dual-head gamma camera equipped with medium-energy collimators through static planar imaging and/or a single photon emission computed tomography (SPECT)

image. Conventional Bremsstrahlung imaging is used in the detection of suspected extra hepatic deposition and to verify the ^{90}Y-microspheres biodistribution for target radionuclide therapy dosimetry application [54,57,58,60–62]. In the absence of a photopeak, SPECT imaging of ^{90}Y is dependent on the continuous and broad spectrum of energy distribution of Bremsstrahlung photons[54]. In contrast to imaging conventional gamma photons emitters, where the acquisition energy windows are usually placed around photopeaks, the same does not happen with ^{90}Y energy spectrum. Due to the continuous nature of the Bremsstrahlung photon energy spectrum there has great variation in the choice of the acquisition energy window being can result in a reduced image quality. This is because exist a substantial numbers of scattered photos in any energy window [29,61]. In quantitative imaging and accuracy are important optimize the acquisition energy window as well as choose an appropriate reconstruction methods.

2.4. Internal Radionuclide Radiation Dosimetry

Radionuclide therapy aims to incorporate an unsealed radiation source in appropriately large amounts into target tissue, delivering a radiation dose sufficiently to produce a therapeutic effect, while maintaining possible side-effects to normal tissue at tolerable levels. Thus, a proper and accurate personalized dosimetry should be requirement for *in vivo* quantification of radiation distributions, as well as its re-distribution over time [20,63].

Internal radionuclide radiation dosimetry is useful for estimate the quantities and spatial and temporal distribution of radiation energy deposited in different tissue by radionuclides. In order to obtain patient-specific dosimetry, information about the time-dependent characteristics of the radionuclide distribution and description of patient anatomy and body composition becomes imperative for the absorbed dose calculation and these are based on modeled biodistribution data and on quantitative imaging procedures [63,64]. Measurements of patient anatomy as mass/volume of target organs are usually performed by computed tomography (CT) or magnetic resonance imaging [6,65,66]. With radionuclide and patient information established several methods have been developed for estimating radiation dose. A methodology widely used for internal dose calculation was developed by the Committee of the Society of Nuclear Medicine is the Medical Internal Radiation Dose (MIRD) formalism [64,67,68]. In internal dosimetry and radiation protection the fundamental quantities that should be considered are: the *absorbed dose* (D), which defines the mean energy absorbed per unit mass of any

material and expressed in Grays [1 Gy = J.kg^{-1}]; the *equivalent dose* (H_T) is defined as the product of the average absorbed dose and a dimensionless radiation weighting factor (w_R) which is measured in Sieverts [Sv]; the *effective dose* (E) is defined as the sum of the weighted equivalent doses over all tissues, multiplied by the appropriate tissue weighting factor (w_T), and is express in [Sv] [19,34,64].

2.4.1. Medical Internal Radiation Dose

In Nuclear Medicine the radiation dose received by the patient is received from radioactive materials within the body, they are referred to as internal dose and cannot be directly measured as happen with distinct radiation dose received from external sources such as an x-ray machine [6]. The MIRD formalism is used to calculate the absorbed radiation dose from internally deposited radionuclides. Absorbed dose is a quantity that usually is estimated from localized distribution of administered radiopharmaceuticals, the radiation decay data of radionuclide and simulations of radiation transport in anthropomorphic models. The measurement of the absorbed dose in patient is established in this first approach becoming an important factor in assessing risk and therapeutic utility [69].

The schema propose by the MIRD is based on the assumption of homogenous distribution of the activity throughout the mass of interest and all of the energy emitted is absorbed [6,58,70,71]. The calculation involve the energy emitted per radioactive decay, the fraction of the emitted energy that is absorbed dose in various target organs, the masses of the organs and both the physical and biologic decay of the injected radionuclide. Absorbed dose rate ($\dot{D}(r_T, T_D)$) to target tissue r_T is given as:

$$\dot{\boldsymbol{D}}(\boldsymbol{r_T}, \boldsymbol{t}) = \widetilde{\boldsymbol{A}}(\boldsymbol{r_S}, \boldsymbol{t})\, \boldsymbol{S}(\boldsymbol{r_T} \leftarrow \boldsymbol{r_S}) \qquad \textbf{Equation 19}$$

where $\tilde{A}(r_T, T_D)$ is the cumulated activity of the radiopharmaceutical in source tissue r_S and $S(r_T \leftarrow r_S)$ is radionuclide specific quantity representing the absorbed dose rate to target tissue r_T at time t after administration per unit cumulated activity present in source tissue r_S [6,58,68,70–73]. The cumulated activity is dependent on biological parameters because represents the total number of radioactive decays occurring within the source organ in which a radiopharmaceutical accumulates. The term $S(r_T \leftarrow r_S)$ usually is referred to as the $S - value$ or $S - factor$ and, deals with the physical components of the absorbed dose for to accounts the energy released from each

radioactive decay and relative geometry of the source organ and the organ for which the absorbed dose is to be calculate [67,68,73]. The quantity S is given as:

$$\boldsymbol{S(r_T \leftarrow r_S) = \frac{1}{m} \langle E \rangle \emptyset(r_T \leftarrow r_S, E, t)} \quad \text{Equation 20}$$

where $\langle E \rangle$ is the mean energy of the transition per nuclear transition, $\emptyset(r_T \leftarrow r_S, E, t)$ is the fraction of radiation energy E emitted within the source tissue r_S at time t that is absorbed in the target tissue r_T and m is the time-dependent mass of the target tissue r_T in the reference individual. The absorbed fraction, $\emptyset(r_T \leftarrow r_S, E, t)$, for β-particles whose range in tissue is short relative to the dimensions of the target tissue is approximately 1 and $\langle E \rangle$ is typically considered as the mean value of the energy spectrum [68].

The absorbed dose, calculated by integrating the dose rate to target tissue over all time is given by the following:

$$\boldsymbol{D(r_T, t) = \int_0^\infty \widetilde{A}(r_S, t) S(r_T \leftarrow r_S) dt} \quad \text{Equation 21}$$

$$\boldsymbol{D(r_T, t) = \frac{A_0 \langle E \rangle}{m} \int_0^\infty e^{-\frac{ln(2)t}{\tau_{1/2}}} dt = \frac{A_0 \langle E \rangle}{m} \frac{\sigma_{1/2}}{\ln(2)}} \quad \text{Equation 22}$$

From the decay data of ^{90}Y, for an activity of 1 GBq in 1 kg of tissue, and if all of the decay energy is completely absorbed within the mass, the absorbed dose can be calculated, more precisely, as follows [58,68,70]:

$$\boldsymbol{D(r_T, t) = \frac{A_0}{m} \left(\frac{0.9267\ MeV}{dis}\right) \left(\frac{1.6022x10^{-13}\ \text{J}}{MeV}\right) \left(\frac{Gy\ kg}{\text{J}}\right) \left(\frac{10^9\ dis}{sGBq}\right)}$$

$$\boldsymbol{x \left(\frac{86400\ s}{day}\right) \left(\frac{2.6684\ day}{ln(2)}\right)} \quad \text{Equation 23}$$

$$\boldsymbol{D(r_T, t) = 49.670 \left[\frac{Gy\ kg}{GBq}\right] x \frac{A_0\ [GBq]}{m\ [kg]}} \quad \text{Equation 24}$$

The MIRD schema presents three important phases: the data collection to identify the various regions containing activity through counts data acquired with a planar scintillation camera, or tomographic SPECT or positron emission tomography (PET) system; the data analysis where it is estimated the activity in regions as a function of the time using the count data and calibration factors obtained from quantitative

measurement techniques; the data processing to integrate of the time-activity curves to obtain the sum of all the nuclear transitions, cumulated activity ($\tilde{A}$) or residence time (τ) in each region [69].

The goal of radiopharmaceutical internal dosimetry is to develop a method to obtain the quantitative measures of radiation distribution to the organs while ensuring that absorbed dose levels to normal or risk organs are kept below tolerance levels so that side effects are minimized [6,67,74]. The patient-specific dosimetry, as a standard practice in external radiotherapy, can be useful to estimate the efficacy of tumor control and predict of toxicity in normal tissue [6,63]. However, the implementation of the internal dosimetry methodology presents two main challenges. The first is the quantification image, by which the counts recorded in an image can be converted to absolute values of activity. The activity distribution is obtained using the functional imaging with SPECT, which can provide 3D voxel representation that is the activity in each individual voxel may be obtained. However, in practice, the finite system spatial resolution and partial volume effects causes great uncertainty associated with quantitating radioactivity within a small volume. The second question that arises is the absorbed dose calculation due the need to deal with problems caused by non-uniform uptake of activity and by non-standard organ geometries [67,69]. Even though there is a limitation in assuming a uniform source distribution in the tumor, the current dose calculation is acceptable as a first approximation for clinical dosimetry when using ^{90}Y-microspheres [70].

Ideally, for each radionuclide therapy patient it is necessary or desirable to perform patient specific treatment planning due to variability in the delivery of the therapeutic agents to tumors and normal liver. A key part of this treatment planning is to include pre-therapy imaging with either a surrogate radionuclide (e.g. ^{111}In for Zevalin) or imaging agent (^{99m}Tc-MAA for ^{90}Y-microspheres) [54,61]. In accordance with guidelines of the European Association of Nuclear Medicine (EANM), imaging studies with ^{99m}Tc-MAA prior to radioembolization are performed to confirm particle localization, rule out extrahepatic shunting to the gastrointestinal tract and lungs, to determinate an optimal therapeutic activity and the tumor to liver ratio [56].

The challenge facing nuclear medicine is to improve the tools and techniques that are available to enable absorbed dose calculation to both target and critical organs-at-risk. The development of more accurate absorbed dose estimates and the correlation of these estimates with biologic response are specially important to a better understanding of the results of treatment, improve the clinical outcomes and for the safe and effective planning patient treatment of radionuclide therapy [8,71].

3. ^{90}Y-microspheres Radioembolization

Liver cancer is the second most common cause of death from cancer worldwide, estimated to be responsible for nearly 746.000 deaths in 2012 [1,75]. In Europe, around 63,500 new cases of liver cancer were diagnosed in 2012 [76].

The liver can develop primary liver cancer in a form either of hepatocellular or cholangiocellular carcinoma. Moreover, the hepatic metastases also is very common from others malignancies such as colorectal cancer, neuroendocrine tumors pancreatic carcinoma and breast cancer [4,57,77]. The surgery is regarded as the first choice and the most effective method of treatment for resection or liver transplantation. But only a select group of these patients meets the conditions for resection [56,70,77]. In the majority of patients the tumor is inoperable at the time of diagnosis because of extrahepatic metastasis, bulky volume, location and multicentricity of the tumor [5,70]. It creates a need to develop other treatments to help to retard tumor progression. That include conformal radiation therapy, hepatic arterial infusion chemotherapy, radiofrequency ablation and radioembolization [56,66,70,77,78]. Radioembolization is an established treatment modality in which intrahepatic arterial delivered ^{90}Y-microspheres are used for selective internal radionuclide therapy (SIRT) [5,7,79]. Currently, two FDA-approved ^{90}Y-microspheres products are available commercially worldwide. These microspheres may be composed of ^{90}Y doped resin (Sir-Spheres®, Sirtex Medical, Lane Cove, Australia) or incorporates ^{90}Y in a glass matrix (TheraSphere®, MDS Nordion, Kanata, ON, Canada) (Table 3) [7,56,58,80]. The method takes advantage of the unique vascular system of the live. Normal liver parenchyma draws approximately 70% - 80% of the organ's blood flow from portal vein. This is in contrast to the hepatic tumors, which have 80% - 100% of their blood supply almost exclusively via the arterial hepatic circulation. This means that the delivery of radioactive microspheres can selectively target the liver malignancies [56,77,81].

Radioactive microspheres are biocompatible but not biodegradable and metabolized [82]. In addition, the radioembolization can provide potential complications such as excess extrahepatic deposition of activity, which may include gastritis/duodenitis, gastrointestinal ulceration/bleeding, cholecytitis, pancreatitis and radiation pneumonitis. And, the excess dose delivered to the healthy liver can leads to the radioembolization-induced liver disease. The unique aspects of therapy require for each patient certain steps of particular importance such as an appropriate imaging, appropriate selection of

patients, pretreatment angiogram with selective visceral catheterization, and treatment simulation with ^{99m}Tc labeled macro-aggregated albumin (MAA), dose calculation, therapy, and follow-up [4,7].

Table 3 - Properties of available commercially ^{90}Y-microspheres.

Description item	SIR-Spheres®	TheraSphere®
Sphere material	Resin	Glass
Sphere diameter (μm)	20-60	20-30
Activity in single vial (GBq)	3	3, 5, 7, 10, 15 and 20
Number of spheres per vial	40-80 x 10^6	1.2-8 x 10^6
Density (g/cm^3)	1.6	3.29
^{90}Y activation mode	Carrier-free	Reactor
Assumed activity per sphere (Bq)	50	2500
Shelf life	24 hours after calibration	12 days after calibration
Manufacture activity calculation recommendations	Empiric Method BSA Method Compartmental MIRD macrodosimetry (Partition Method)	Non-compartmental MIRD macrodosimetry

3.1. Treatment Planning

For a successful radioembolization, a proper planning of the procedure is necessary to ensure that patients receive a safe and effective ^{90}Y-microspheres delivery [83]. The main aim for planning the delivery of ^{90}Y-microspheres is minimize radiation damage to the extrahepatic structures ensuring that the indication for the treatment is correct and helping to deliver the microspheres the right places in the liver [84].

Careful patient selection and preparation for ^{90}Y liver-directed therapy result in an optimal risk/benefit ratio for the patient. Treatment planning for implantation of ^{90}Y-microspheres is typically a 2-stages process, a simulation of the actual treatment with ^{99m}Tc-MAA particles that are roughly the size of the microspheres and 1-2 weeks later an implantation phase [85].

3.1.1. Patient Selection

The candidates referred for SIRT include patients with non-resectable hepatic primary or metastatic cancer that do not respond adequately to other treatment modalities such as transplantation, radiofrequency ablation or transarterial chemoembolization. A comprehensive understanding of the general clinical condition of patient , as described by the Eastern Cooperative Oncology Group (ECOG), laboratory test results, treatment history, and potential future treatment options is critical in patient selection [5,86].

Treatment with ^{90}Y-microspheres must be based on careful review of screening tests of the individual patient. The initial workup should include cross-sectional multi-phase CT or magnetic resonance (MR) imaging of the liver for assessment of tumoral and nontumoral volume, the radiologic staging of disease including number, size, and localization of tumor, portal vein patency, and presence of extrahepatic disease. In addition, molecular imaging with SPECT/CT or PET/CT can be very helpful [5,7,83]. Serum chemical analyses should be performed to evaluate hepatic and renal function and to determine the presence tumor markers. In general, relative contraindications to treatment with ^{90}Y-microspheres include limited hepatic reserve, irreversibly elevated bilirubin levels, compromised portal vein (unless selective or super selective radioembolization can be performed), and prior radiation therapy involving the liver. Sufficient hepatic function is of primary importance and is regarded as the greatest limitation (Child–Pugh score ≤ B7). The renal status should be also adequate to accommodate the use of contrast agents during the diagnostic and the therapeutic angiogram [83,87].

All patients should be selected according to strict inclusion/exclusion criteria and, need to be assessed by a multidisciplinary team (Table 4) [7,83].

Table 4 - Indications and contraindications for Radioembolization.

Indications	Contraindications
Disease nor amenable to surgical resection, liver transplantation or ablative therapies.	Extensive and untreated portal hypertension.
Compensated or early decompensated liver cirrhosis (Child-Pugh ≤ B7).	Active hepatitis.
Performance stage ≤ 2.	Extrahepatic deposition of ^{99m}Tc-MAA (i.e. gastrointestinal tract).
Life expectancy > 3 months.	Anticipated lung exposure to ^{90}Y radiation >30 Gy based on pre-treatment ^{99m}Tc-MAA scan.
Liver only or liver dominant disease.	Excessive tumor burden with limited hepatic reserve.
Preoperative indications.	Elevated total bilirubin level (2 mg/dL) in the absence of a reversible cause.

3.1.2. Angiogram and Therapy Simulation with ^{99m}Tc-MAA

SIRT is a flow-directed therapy that relies upon neoangiogenesis and increased blood flow in malignant tumors to preferentially take up ^{90}Y-microspheres from the hepatic arterial circulation [5]. Once the patient has been selected as a potential candidate, a pretreatment hepatic arteriography and hepatic arterial perfusion (^{99m}Tc-MAA) are performed before radioembolization. The aim of the initial angiographic assessment of the vascular anatomy is identify the vascular supply of the liver and the tumor; identify and embolize vessel that may lead to non-target deposition of the radioembolic material; determine the procedure termination for the microspheres [58,86]. Flow characteristics in the hepatic artery should be detected and extrahepatic deposition of the microspheres is prevented by arterial catheters inserted percutaneously under fluoroscopy by the interventional radiologist. Meticulous technique is required to embolization of all relevant vessels including superior mesenteric, gastroduodenal and right gastric, right and left hepatic artery and other extrahepatic vessels given the possibility of non-target deposition of microspheres. It is important to note that these vessels/organs can revascularize quickly, and therefore the embolization should be

performed close to the anticipated treatment date, realizing a check arteriogram before radioembolization to ensure that such revascularization has not occurred [83].

Once the mapping and embolization steps are completed and the treatment location identified, ^{99m}Tc-MAA (111 MBq – 185 MBq) is injected through the catheter by a nuclear medicine physician in a slow-pulse over several minutes. The infusion of ^{99m}Tc-MAA is used to predict the distribution of the ^{90}Y-microspheres prior to treatment [88]. The patient is then taken to a gamma camera where planar imaging and SPECT of the upper abdomen are acquired to confirm particle localization and rule out extrahepatic shunting to the gastrointestinal tract and lungs [10,86]. The lung shunt fraction (LSF) is calculated using planar images in anterior and posterior projections (Figure 17), given from the total counts within regions of interest (ROI) over both lobes of the lung (C_{lung}) and entire liver counts (C_{liver}) (Equation 25) using the geometrical mean of images. The extrahepatic shunts were noted on both planar and SPECT images. Moreover, SPECT constitutes the basis for image fusion with other pre-/post-therapeutic tomographic images as CT or MR [58,89].

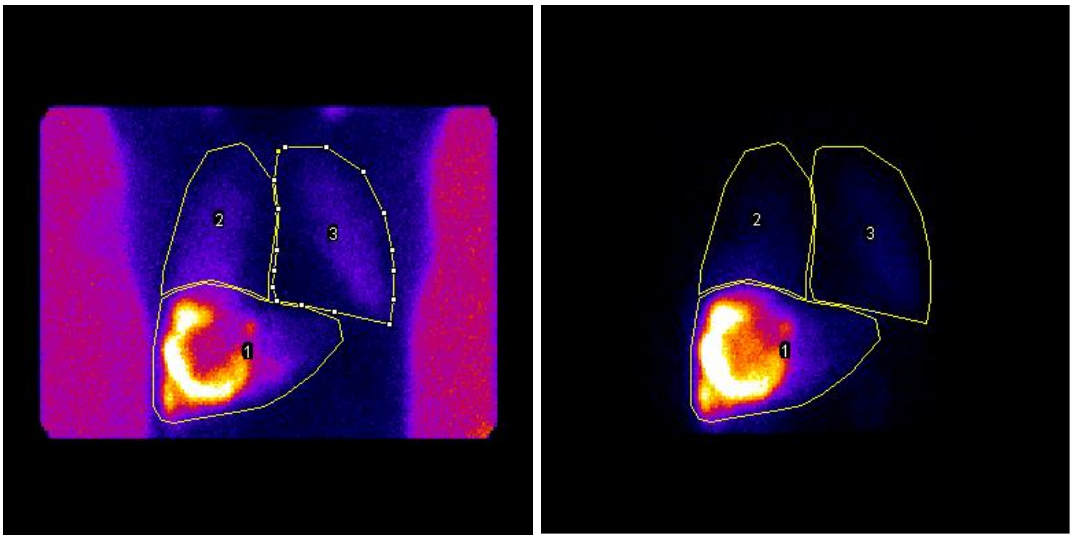

I II

Figure 17 - Planar gamma camera with ROI draw. (I) Planar transmission/emission image with planar phantom for anatomical location of the lungs. (II) Planar emission image for the calculation of the LSF.

$$\boldsymbol{LSF} = \frac{\boldsymbol{C_{lung}}}{\boldsymbol{C_{lung}} + \boldsymbol{C_{liver}}} \times \mathbf{100}\% \qquad \textbf{Equation 25}$$

Patients in whom the hepatopulmonary shunt fraction (LSF) is greater than 20% of the injected activity (Table 5) or in whom the shunt fraction indicates potential exposure of the lung to an absorbed radiation dose of more than 30 Gy can be excluded from the use of microspheres due to the possibility of radiation pneumonitis. In patients with a

LSF less than 20% a reduction in the total administered activity is necessary [58]. In short, the ^{99m}Tc-MAA should ideally be delivered selectively into the hepatic circulation to simulate as closely as possible the planned ^{90}Y radioembolization, allowing accurate determination of any likely pulmonary breakthrough.

Table 5 - Percentage of shunting to the lungs.

Percent Lung Shunting	Activity of ^{90}Y (GBq)
< 10%	Deliver full amount of ^{90}Y-microspheres
10% to 15%	Reduce amount of ^{90}Y-microspheres by 20%
10% to 20%	Reduce amount of ^{90}Y-microspheres by 40%
>20%	Do not give ^{90}Y-microspheres

3.2. Activity and Dose Calculation

Radioembolization usually induces tumor regressions of varying degrees in selective regions. The biological effects of therapy with microspheres are heavily dependent of two components: Dose and Activity. Dose (Gy) is specifically defined as the energy absorbed per unit mass of tissue. In SIRT, the absorbed dose depends on the amount of ^{90}Y activity (GBq) delivered to the target organ. The activity is a constant value, but how microspheres distribute inside the liver after injection is influenced by hemodynamics of the hepatic artery blood flow and the vessel density inside the tumors [79].

Therapeutic efficacy is closely related to the injection activity of ^{90}Y-microspheres. Currently, two ^{90}Y-microspheres products are available commercially, which are made of resin (SIR-Spheres®) or glass (TheraSpheres®) [56]. The required activity for treatment of each patient is to be calculated differently according to whether glass or resin microspheres are to be used. For resin microspheres the manufacturer's user's manual (Sirtex user's manual) suggests three methods of estimating the activity to use for resin microspheres treatment: Empiric Method, Body Surface Area Method, Partition Method. In contrast, the for ^{90}Y glass microspheres have only one method for activity calculation. In common, the four methods have suggested reducing the prescribed ^{90}Y resin microspheres activity if the lung shunt fraction (LSF) is upper 10%, in order to lower the radiation risks to the lungs, because a correlation exists between the administered activity and the lung shunt fraction (Table 5) [9,82,90].

3.2.1. Glass microspheres

TheraSpheres® was approved by the FDA in 1999, with indication for radiation treatment or as a neoadjuvant to surgery or transplantation in patients with unresectable HCC. This therapeutic device consists of insoluble glass microspheres where ^{90}Y is an integral constituent of the glass [87].

The activity for administration of glass microspheres relates directly to the desired absorbed dose. A typical dose between 80 Gy and 150 Gy should be delivered to the treated liver. This wide range allows a treating with clinical flexibility, where patients with cirrhosis should be treated more conservatively (80 – 100 Gy); whereas patients without cirrhosis may be treated with more dose (100 – 150 Gy). Treatment planning using ^{99m}Tc-MAA predicts a target tumor dose at least 205 Gy. It is recommended that the lung dose be less than 30 Gy or 50 Gy for cumulative treatments to prevent radiation pneumonitis. Assuming that glass ^{90}Y-microspheres has uniform distribution in throughout the liver and ^{90}Y undergoes complete decay in the liver, one single method is proposed by the manufacturer for activity calculation, and is based in MIRD formalism [7,82,87,91]:

$$\boldsymbol{A_{total}\,(GBq)} = \frac{\boldsymbol{D_{target} \times M_{target}}}{\mathbf{49.670}} \qquad \text{Equation 26}$$

where D_{target} (Gy) is the absorbed delivered dose to the target liver mass and M_{target} (kg) is the mass of the target liver mass. Equation 26 not takes into account adjustment to the ^{90}Y activity based on LSF. However, a fraction of the microspheres will flow into the pulmonary circulation, when LSF and vial residual is taken into account, the actual doses in the selected volumes of interest (i.e. tumor and healthy liver) after the vial is infused are calculated using the following formula [91,92].

$$\boldsymbol{D\,(Gy)} = \frac{\boldsymbol{A_{total} \times 49.670 \times (1 - LSF - R)}}{\boldsymbol{M_{target}}} \qquad \text{Equation 27}$$

After administration of ^{90}Y-microspheres, the percentage of injected activity (R) remaining in the dose vial, inlet and outlet catheters of the delivery device should be determined for calculation of the actual dose. The LSF is calculated beforehand by using ^{99m}Tc-MAA scintigraphy. It is noted this dosimetry model is independent of tumor burden [87]. See Table 3 for more detailed data.

3.2.2. Resin microspheres

SIR-Spheres® were granted premarket approval by the FDA in 2002, with indication for the treatment of unresectable metastatic liver tumors from primary colorectal cancer with adjuvant intra-hepatic artery chemotherapy of Floxuridine (FUDR). SIR-Spheres® is a device with two components, resin based biocompatible microspheres containing ^{90}Y [58,87,93].

For the resin microspheres, the manufacturer (Sirtex) proposes three alternatives to decide ^{90}Y activity. Just as with TheraSphere®, assumes SIR-Spheres ^{90}Y-microspheres are homogeneously distributed throughout the liver [58].

3.2.2.1. Empiric Method Calculation

The first method proposed by SIR-Spheres is the Empiric Method and was devised on the intraoperative calculations from beta probes of early clinical trials[94–97]. The activity calculation to be used in treatment is based solely on an estimate of tumor involvement (I_T) (Equation 28). The volume of the tumor (V_T) and the volume of the normal liver (V_{NL}) were calculated on computed tomography performed by manual slice by slice contouring. In case of lung shunt is less than 10%, the empiric method recommends three different activities presented in Table 6 [9,56,62,83,87,98]. This method is not the most recommended because it has a crucial limitation that are an individual characteristics of patient is not considered and presents a higher risk of radioembolization-induced liver disease [83,99]. However, it cannot be considered that the empiric method is not useful, since through it was possible to establish an upper limit of activity to be injected according to the clinical conditions previously developed [79].

$$\boldsymbol{I_T}(\%) = \frac{\boldsymbol{V_T}}{\boldsymbol{V_T + V_{NL}}} \boldsymbol{x\ 100} \qquad \text{Equation 28}$$

Table 6 - Activity recommendations.

Percent Tumor Volume	Activity of ^{90}Y (GBq)
< 25%	2,0
25% to 50%	2,5
> 50%	3,0

3.2.2.2. Body Surface Area Method Calculation

The activity calculation most widely used for ^{90}Y resin microspheres has been the body surface area (BSA) method based in empiric method. The second method is recommended by the manufacturer (Sirtex) and has been used safely in clinical trials [97]. The BSA method takes into account the patient's BSA, that is, the patient's weight (W) and height (H), as well as the V_T volume and V_{NL} volume, assuming a correlation between BSA and tumor involvement [9,62,65,82,87]. According to the Dubois and Dubois the formula for BSA is described as [100,101]:

$$\boldsymbol{BSA\ (m^2) = 0,20247\ x\ H\ (m)^{0,725}\ x\ W\ (kg)^{0,425}} \qquad \text{Equation 29}$$

This model assumes that the size of each patient's liver correlates with the BSA, leading to a proportional activity adjustment (Equation 30) [7,9,65,66]. As in the empiric method the activity calculation requires the normal liver and tumor volume from the CT scan [90].

$$\boldsymbol{A\ (GBq) = (BSA - 0,2) + \left(\frac{V_T}{V_T + V_{NL}}\right)} \qquad \text{Equation 30}$$

The BSA method is used due its simplicity, presenting objective responses e low incidence of toxicity. Nevertheless, its main limitation is the absence of the tumor-to-normal liver (T/N) ratio, which can result in underdose for patients with larger livers and overdose for patients with small liver [7,8,56,65]. The T/N ratio exposes on the tumor-to-normal uptake ratio of the therapeutic radiopharmaceutical give a more patient-specific and scientifically sound estimate the proportional microspheres distribution in the tumor [8,9,102].

3.2.2.3. Partition Method Calculation

According to Sirtex, the Partition Model (PM) is another method for calculation of dose/activity [90]. The Partition Method provide the mathematic derivations of the equations used in the Medical Internal Radiation Dose (MIRD) formalism developed by the Committee of the Society of Nuclear Medicine, as previously mentioned [58,66,71].

Ho *et al*, using the MIRD formula, formulated partition model for estimating radiation doses to the lungs, tumor and normal liver parenchyma discriminatively and verified the activity distribution by intraoperative measurement [103,104]. The partition model incorporates tissue masses and a measurement of the tumor-to-normal liver (T/N) ratio.

It requires separation of the organ system into compartments (lungs, tumor and non-tumorous liver). This because, the distribution profile of the ^{90}Y-microspheres activity is determined by the relative vascularity and volume of the tumor and normal liver compartments, which is expressed as the tumor-to-normal liver (T/N) ratio. And, when lung shunting due to intrahepatic peritumoral arteriovenous communication occurs, a third compartment (lung) is expressed as the lung shunt fraction (LSF) [71]. The LSF is calculated on planar images using the formula below:

$$\boldsymbol{LSF} = \frac{\boldsymbol{Counts_{lung}}}{\boldsymbol{Counts_{lung} + Counts_{NL} + Counts_{T}}} \times \mathbf{100} \qquad \text{Equation 31}$$

The determination of the percentage of pulmonary shunt may require that there be a modification to the ^{90}Y activity determined or, for patients with > 20% pulmonary shunting precludes use of SIR-Spheres microspheres (Table 5) [90].

The percentage of activity shunted to the lung, the evaluation of extrahepatic deposition and the tumor-to-normal liver (T/N) ratio (Equation 32) are determined from pre-therapeutic planar and SPECT images acquired using ^{99m}Tc-MAA with the aim to predict the intrahepatic distribution of ^{90}Y-microspheres used in subsequent treatment and hence radiation dose to each compartment [10,90,103,105]. The nuclear medicine scan is performed in all patients.

$$\boldsymbol{T/N} = \frac{\boldsymbol{A_T/M_T}}{\boldsymbol{A_{NL}/M_{NL}}} \qquad \text{Equation 32}$$

In ^{90}Y therapy, it is assumed that ^{90}Y-microspheres will follow the MAA distribution. However, there are great uncertainties associated with this approach, for the distribution of radiotracer between these paired studies does not always match. Parameters that may influence distribution differences between ^{99m}Tc-MAA and ^{90}Y-microspheres include the reproducibility of catheter position during therapy; the different characteristics of ^{99m}Tc-MAA and resin ^{90}Y-microspheres, physiologic variances in hepatic blood flow, tumor histopathology and tumor load. In radionuclide therapy, the absorbed dose is generally estimated, because *in vivo* dose measurement is not practicable in clinical settings. And, without accurate patient dosimetry, it is impossible to establish fundamental dose-response relationship for treatment efficacy and toxicity [10,88,106,107].

The PM involves implanting the highest possible activity to the tumor while maintaining radiation dose to the healthy liver and lung within acceptable limits. Thus, the maximal activity to be administered in order to preserve normal liver and lung are calculated

using the equations Equation 33 and Equation 34. The activity required should be calculated using the lung dose recommended as the limiting factor, and then again using the normal liver dose recommended as the limiting factor. The lower of the two activities calculated should be used [66,90].

$$\boldsymbol{A_{total}\,(lung) = \frac{D_{\max\,lung} \times V_{lung} \times \frac{100}{LSF}}{49{,}670}} \qquad \textbf{Equation 33}$$

$$\boldsymbol{A_{total}\,(liver) = \frac{D_{\max\,liver} \times [(T/N \times V_T) + V_{NL}]}{49{,}670 \times \left(1 - \frac{LSF}{100}\right)}} \qquad \textbf{Equation 34}$$

where D_{max} is the tolerance absorbed dose for healthy tissues, V_{lung}, V_T and V_{NL} represents the volumes obtained from CT scan for lung, normal liver and tumor respectively, LSF is the lung shunt fraction and T/N is the ratio between tumor and normal activity per unit mass. All activities are in GBq and the volumes, with the approximation of mass equal to volume, in dm^3. The lung is largely filled with air then, the CT scan cannot be used to measure the volume of lung, assuming thus an estimated volume of 1 dm^3 [66,90,103]. The recommendations found in literature suggested that 30 Gy could be the limit for the tolerance absorbed dose to the lungs [66,104]. However, the SIR-Spheres® User Manual recommend that pulmonary radiation doses during SIRT should preferably remain below the 25 Gy [90]. The manufacture and the literature suggested that the normal liver can tolerate radiation up 80 Gy, but in patients with cirrhotic liver the limit should not exceed 70 Gy [90,104,108]. The non-resectable HCC is radioresistent and, therefore, it is necessary to implant absorbed doses for tumor response is at least 120 Gy [56,104]. However, there is a limitation in delivered doses because it can cause severe injury to the surrounding tissue, including the liver parenchyma and duodenum [109].

The total activity, A_{total}, of ^{90}Y-microspheres delivered to a patient is distributed in three discrete vascular compartments. As seen previously, the MIRD schema can be used to calculate the absorbed dose on tissue, given that is analytical calculation available at this time and, suggested by manufacture SIR-Sphere®. According to the basic dosimetry formula of ^{90}Y-microspheres and radioactivity distribution, the absorbed doses are expressed as [56,66,90]:

$$\boldsymbol{D_{Lung} = \frac{A_{total} \times 49.670 \times \left(\frac{LSF}{100}\right)}{V_{Lung}}} \qquad \textbf{Equation 35}$$

$$D_{NL} = \frac{A_{total} \times 49.670 \times \left(1 - \frac{LSF}{100}\right)}{V_{NL} + (T/N \times V_T)} \quad \text{Equation 36}$$

$$D_T = T/N \times D_{NL} \quad \text{Equation 37}$$

In clinical practice, the Partition Model is suggested as an alternative means of activity calculation in patients with a tumor mass localized in a discrete area within the liver and the tumor can be delineated as a region-of-interest on a SPECT camera image. This is recommended in majority of cases to patients with HCC where there is often a large single tumor mass. In contrast, patients with metastatic disease usually have multiple areas of metastatic where it presents ill-defined margins that precludes defining the tumor and normal liver [9,90].

Among those methods, the PM method based on ^{99m}Tc-MAA imaging is the most personalized, with the development of more accurate absorbed dose estimates. The correlation of these estimates with biologic response will lead to a better understanding of the results of treatment and improve the clinical outcomes [57,71].

3.2.2.4. Body Surface Area Method versus Partition Method

Different methods have been developed and used for activity calculation and prescription. For resin microspheres, the BSA method and the partition method can be both be used for ^{90}Y activity calculation. The manufacturer's recommendation for the use of PM did not appear to be intended for diffuse tumor [65,90].

The BSA method is the most common in clinical trials due its simplicity and has been used safely, with objective responses and low incidence of toxicity [110]. The calculated activity of the whole liver is correlated with the percentage of the target site as a proportion of the whole liver. Furthermore, the BSA method neglects the individual intrahepatic distribution differences, calculated by the activity concentration ratio between lesion and healthy liver (T/N), which can expose patients to the risk of unnecessary toxicity or tumor underdosage [56,65,66]. The estimated T/N ratio can predict the success or failure of ^{90}Y radioembolization and, its embedding in the activity calculation will lead to a higher administered activity and higher tumor dose without compromising healthy liver tissue [7,8]. The semi-empiric method may has limitations with ^{90}Y activities, because will almost always derive activities ranging between 1.0 and 3.0 GBq. This is because, for example, to small patient who is 1.4 m tall, weighs 40 kg and has 1% tumor involvement the ^{90}Y activity will yield 1.0 GBq. On the other limit a large

patient who is 1.9 m tall, weighs 100 kg and has 90% tumor involvement will yield an estimated ^{90}Y activity of 3.0 GBq [8]. The advantages and disadvantages of the Body Surface Area method are summarized in Table 7.

The partition model was developed by Ho et al. and is validated for calculated ^{90}Y resin microspheres activity based on MIRD formalism. This method takes most relevant factors in account, based on anatomical information but also on the targeting pattern and uptake intensity obtained from ^{99m}Tc-MAA [56,66,82]. This planning treatment needs volume measurement of the liver and tumor tissue and defines compartments (lung, tumor and normal liver) for radiation dose calculation. The estimated T/N ratio it also incorporate to give a more patient-specific and scientifically sound estimate of the radiation dose delivered to each compartment [8,11]. Partition modeling allow for much greater physician flexibility in radiation dose planning, beyond the traditional fixed approach of percentage lung shunting and related empirical adjustments to the desired ^{90}Y activity. However, the literature recommends that PM be applied to solitary hepatic tumors or multifocal lesions if each can be adequately localized. The partition model is the safe, effective and individualized radiation therapy planning [8,9,90,102,103]. The advantages and disadvantages of partition method are summarized in Table 8.

Table 7 - Advantages and disadvantages of the Body Surface Area method

Advantages	Disadvantages
Simple and user friendly	Less personalized than partition modeling
Strong historical data of clinical Use	Low scientific basis. Not a true 'dosimetric' method
Recommended for use in subcentimeter tumors or tumors with ill-defined margins, by visual estimation of the overall tumor burden	The desired ^{90}Y activity in cases of high liver-to-lung shunting is adjusted empirically using standard reference tables provided by the manufacturer
	Artificially limits the injected ^{90}Y activity between 1.0 and 3.0 GBq
	Tumor radiation dose (Gy) is unknown unless the estimated T/N ratio also is calculated

Table 8 - Advantages and disadvantages of the partition method.

Advantages	Disadvantages
Personalized dosimetry	More complex and resource intensive
More scientifically sound than the BSA method	Less historical clinical data as compared to the BSA method
The desired ^{90}Y activity in cases of high lung shunting is adjusted on the basis of predicted lung radiation dose (Gy)	More appropriated for single or discrete tumors
No theoretical limit to the ^{90}Y activity to be injected	
Greater control over radiation dose (Gy) to lung, liver and tumor compartments	

The partition method is recommended in the majority of cases, but is not currently feasible in patients with diffuse metastatic disease with ill-defined margins. ^{99m}Tc-MAA scintigraphic resolution in subcentimeter tumor sizes may not be adequate for accurate tumor ROI delineation in T/N ratio estimation. For very small tumor masses and tumor with diffuse margins the BSA method is more suitable [8,65].

The BSA method and the PM have common limitation this because both were formulated on the assumption of uniform resin microsphere distribution within tumor and normal liver compartments. Nonetheless, the actual distribution of microspheres may be non-uniformly distributed across the liver, with preferential deposition at the tumor periphery. The effect of radiation *cross-fire* must also be considered. These issues create complex dosimetric problems requiring specialized medical physics teams and computed power. Even with the limitation presented the partition method is technically superior to the BSA method [8,82].

3.3. ^{90}Y-microspheres Therapy

The ^{90}Y-microspheres implantation involves repeating the catheterization procedure on the treatment day. The activity of ^{90}Y-microspheres to be implanted is dependent on factors such as type of spheres used (SIR-Spheres or TheraSphere), properties of the target site (primary liver cancer or metastatic tumors) and the level of LSF derived from ^{99m}Tc-MAA scan [56]. ^{90}Y-microspheres are then infused through the hepatic arteries under fluoroscopic guidance, with caution paid to any reflux of spheres. This is because the arterial flow dynamics vary considerably throughout the radioembolization procedure due both to the embolic load of the microspheres and to vessel reactivity in the presence of the microcatheter and the perfusion pressure applied during infusion. In this way, the microspheres administration should be as smooth as possible and constant vigilance are essential to minimizing any turbulent flow or unanticipated jets, which may dislodge the catheter tip from its desired location and/or propel microspheres into unplanned vessels. However, is essential to sustain sufficient pressure and flow to maintain a fairly uniform microspheres suspension avoiding 'settling out' in the vial, delivery tubing or catheter. The administration may be done with alternating injection of infusion solution and contrast medium, in order to maintain fluoroscopic surveillance of changing flow dynamics throughout the procedure [5].

In ^{90}Y therapy, as mentioned before, it is assumed that the ^{90}Y distribution will be the same as that for the ^{99m}Tc-MAA. However, the correlation between ^{99m}Tc-MAA and ^{90}Y distribution can vary. There are several factors that may have caused the disagreement between these activity distributions including differences in catheter position, injection technique, progress of disease between ^{99m}Tc-MAA and ^{90}Y studies and difference in energy radiation between Bremsstrahlung and ^{99m}Tc. In addition, the number, density, size and morphology of the radiopharmaceuticals may also have resulted in a different activity distribution [10,106]. Despite the variability which may occur in the distribution of ^{90}Y activity are important followed accurate dosimetry and the pre-defined strategy to avoid non-hepatic deposition of microspheres [5].

After the procedure is complete, the patient is again taken to a gamma camera and planar and SPECT images of the liver can be performed using ^{90}Y Bremsstrahlung imaging. A precise evaluation of microsphere deposition after treatment is critical to exclude non-targeted microspheres deposition and to evaluate the radiation absorbed dose delivered to the tumor [58].

4. Material and Methods

^{90}Y is widely used in targeted radionuclide therapy and usually imaged with SPECT by recording the Bremsstrahlung x-ray of the β-decay, the energy spectrum of which is continuous. However, Bremsstrahlung SPECT imaging does not have adequate resolution for dose distribution. This because the continuous shape of the x-ray spectrum induces the presence of a significant fraction of scatter rays in the acquisition energy window, reducing the accuracy of biodistribution and of dosimetry assessments. In this way, SPECT image that is obtained prior to the treatment following hepatic infusion of ^{99m}Tc-MAA can be used to provide data regarding the T/N ratio uptake. This data could potentially be appropriate in dose calculation. In addition, the ^{99m}Tc-MAA is primarily used for LSF analysis and evaluation of extrahepatic deposition, with the aim to predict intrahepatic post-therapy ^{90}Y-microspheres distribution.

In this study, the main focus goes to the resin microspheres.

4.1. Pretreatment imaging and dosimetry

^{99m}Tc-MAA scintigraphy is made at the time of the pretreatment angiography to quantify the LSF and to detect any extrahepatic deposition of activity. Pre-treatment imaging was performed on a dual-head γ-camera, e.cam (Siemens Health Care). Static planar imaging is done with low energy, high resolution, and parallel-hole collimator capable of obtaining conjugate anterior and posterior images of the patient. Typically, two static images are acquired, one with planar phantom positioned in posterior and other without planar phantom. These images capture the liver and lungs and, the position of the detector and of the patient not change during the images acquisition. Regions-of-interest (ROI) over the whole liver and lungs are drawn on the actual image using the ImageJ program[1]; the image with planar phantom will help with the ROI outline. A planar image is illustrated in Figure 18, with typical scan parameters listed in Table 9. Both planar acquisitions, with and without planar phantom, are obtained using the same protocol. The ROI counts for each region are recorded and the lung shunt is calculated as described in section 3.2.1.

[1] ImageJ is an open source, Java-based image processing program developed at the National Institutes of Health. It can display, edit, analyze, process, save and print many image formats including TIFF, GIF, JPEG, BMP, DICOM, FITS and

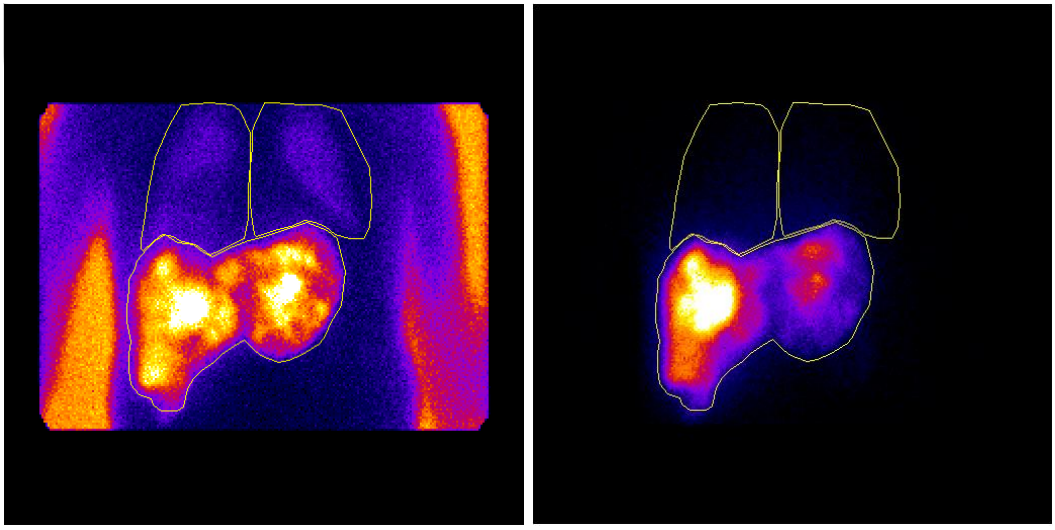

I II

Figure 18 - Planar gamma camera image with ROI. (I) Planar transmission/emission image with planar phantom for anatomical location of the lungs. (II) Planar emission image for the calculation of the LSF.

After obtaining planar images, the distribution of the microspheres in the liver was assessed on the SPECT images. SPECT images of the abdomen are acquired on an e.cam (Siemens Health Care) by rotating gamma detectors around a patient and, subsequently reconstructed using reconstruction software. LSF are calculated using planar images, and extrahepatic activity is noted on both planar and SPECT images. In SPECT base dosimetry, the ^{99m}Tc-MAA particles are used as surrogates for microspheres to assess to microsphere distribution within the liver. For this, software tools perform three-dimensional registration of images sets providing geometric correlations of the activity data with patient anatomy. The uncertainty in the geometrical correlation recommends the use of SPECT/CT fusion images (Figure 19). The typical SPECT acquisition parameters are given in Table 9. SPECT imaging data was reconstructed using an iterative method (2D OSEM, 8i, 4s, 6mm Gaussian filter), and images were then visualized with and without fusion with CT scan data.

Table 9 - Static planar imaging and SPECT protocols, using ^{99m}Tc energy specification.

Parameters	Planar ^{99m}Tc-MAA	SPECT ^{99m}Tc-MAA
Zoom	1	-
Matrix	256x256	128x128
Azimuth angles	-	64
Counting time	300 s	30 s per angle
Energy window	140 keV (15%)	140 keV (15%)
Collimator	Low Energy	Low Energy

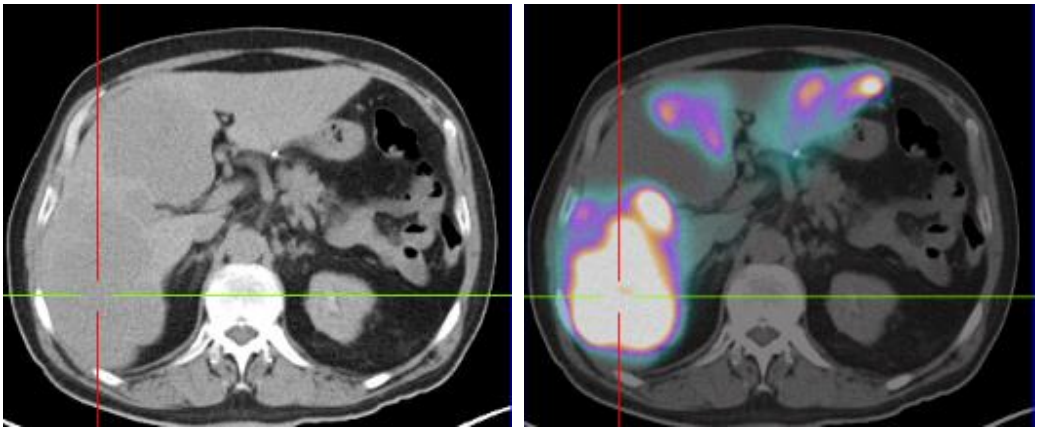

Figure 19 - Pretreatment ^{99m}Tc-MAA SPECT image.

In tumors where the radionuclide distribution and the tumor the can be easily delineated on imaging studies, the tumor-to-liver activity uptake can be estimated from the ^{99m}Tc-MAA study. Volume measurements of liver and tumor were carried out on CT images using ARIA data-processing console display with “Contouring” software (Figure 20). The count measurements were conducted on the SPECT images using ImageJ program. A ROI was drawn in each axial slice encompassing the tumor (ROI_1), and the same is done to the liver (ROI_2). The normal liver counts were obtained by subtracting liver and tumor counts. All delineated ROIs were manually registered to the ^{99m}Tc-MAA SPECT with help of contrast-enhanced CT scan for segmentation (Figure 21).

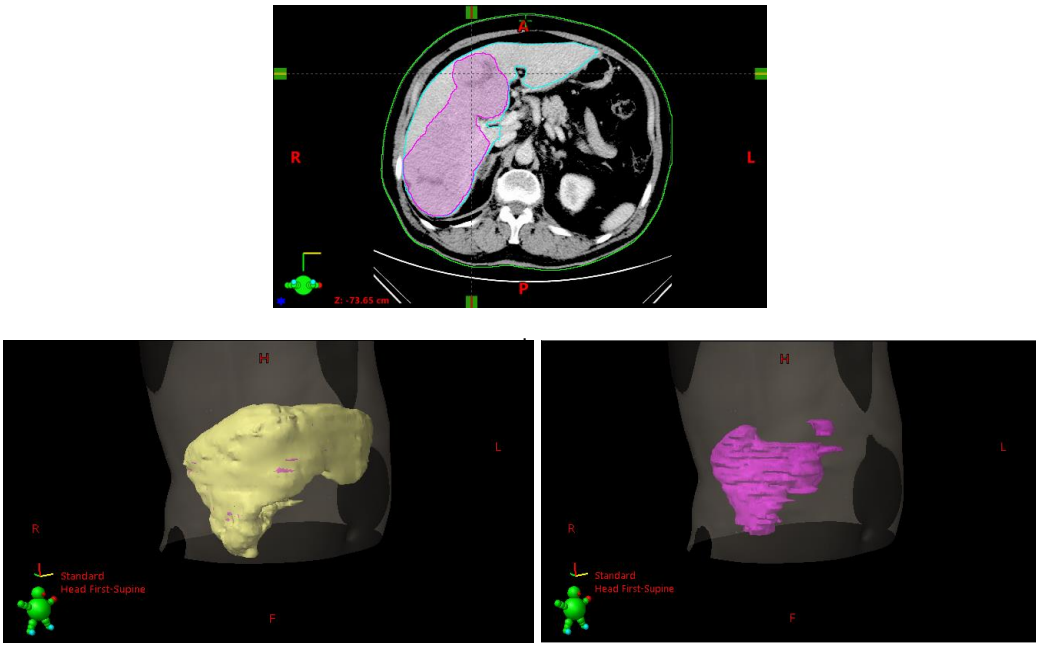

II III

Figure 20 - (I) Segmentation of liver and tumor on CT scan. (II) Representative liver from segmentation. (III) Representative tumor from segmentation.

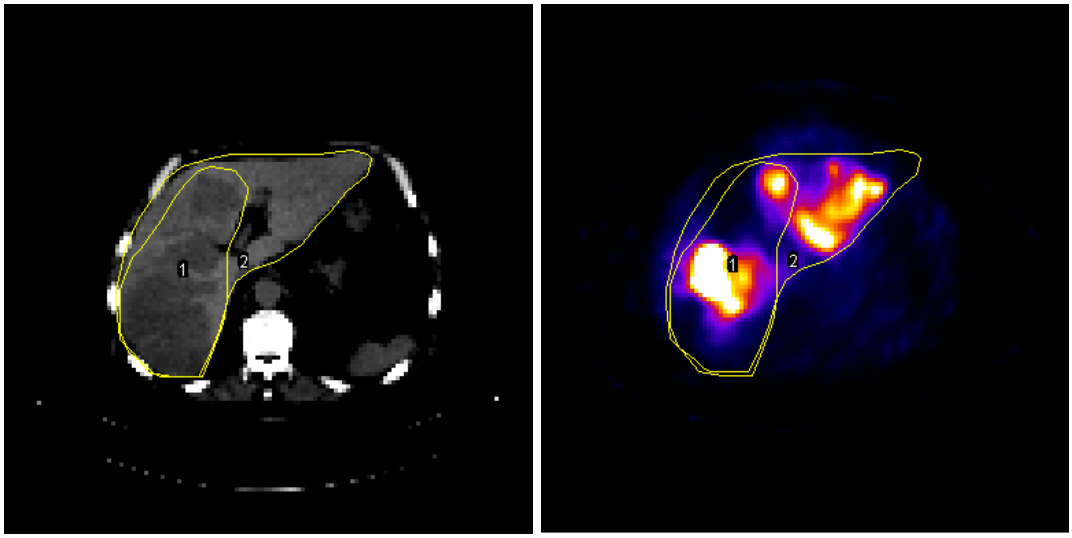

Figure 21 - Representative axial SPECT image to calculate the T/N ratio. CT and ^{99m}Tc-MAA/SPECT images with ROI surrounding the entire liver and the treated tumor.

These ROIs were then used to measure the activity distribution (expressed in counts), where the T/N is calculated as the tumor-to-liver counts over the corresponding ROIs. Mathematically the T/N is calculated using the Equation 32.

The activity and dose absorbed by the tissues of interest (lung, normal liver and tumor) were calculated based on the partition method (section 3.2.2.3) for three cases. Where the injection positions of ^{99m}Tc-MAA and ^{90}Y-microspheres also are analyzed. In addition, sixty four patients evaluated for radioembolization were retrospectively analyzed. The activity of ^{90}Y-microspheres administered to all patients was calculated by the method recommended by the company Sirtex, based on the body surface area and the percentage of perfused liver volume and percentage of liver volume occupied by the tumor (section 3.2.2.2).

4.2. Evaluation of Bremsstrahlung imaging

Treatment efficacy of radioembolization is assessed by the ^{90}Y Bremsstrahlung SPECT imaging. Post-therapy SPECT image has the potential of providing reliable activity map of ^{90}Y-microspheres distribution. However, these images demonstrate a poor image quality. Quantitative Bremsstrahlung imaging is very difficult to obtain due scatter, septal penetration, the continuous nature of the Bremsstrahlung energy spectrum, and inefficient Bremsstrahlung production. In literature, several image acquisition parameters and subsequent different reconstruction protocols are suggested [60,61]. With the aim to obtain an appropriate ^{90}Y Bremsstrahlung SPECT imaging was evaluated

several reconstruction methods. ^{90}Y SPECT images were acquired using a gamma camera (e.cam, Siemens) equipped with a medium energy general purpose parallel-hole collimator and an energy window of 136-184 keV. The acquisition parameters of ^{90}Y Bremsstrahlung SPECT are present in Table 10.

Table 10 - SPECT imaging protocol for ^{90}Y Bremsstrahlung post-implanting studies.

Parameters	^{90}Y-Bremsstrahlung
Acquisition matrix	128x128
Azimuth angles	64
Counting time	30 s per angle
Energy window	160 keV (15%)
Collimator	MEGP

4.2.1. Phantom study

^{90}Y Bremsstrahlung image was acquired with activity uniformly distributed in the line source placed inside a Jaszczak phantom (Standard Jaszczak Phantom™, Data spectrum Corporation, Durham, NC) (Figure 22). The phantom was filled with water and a line source contained 222 MBq was placed inside in the longitudinal direction. The projections were acquired using the same protocol acquisition for post-therapy study (Table 10).

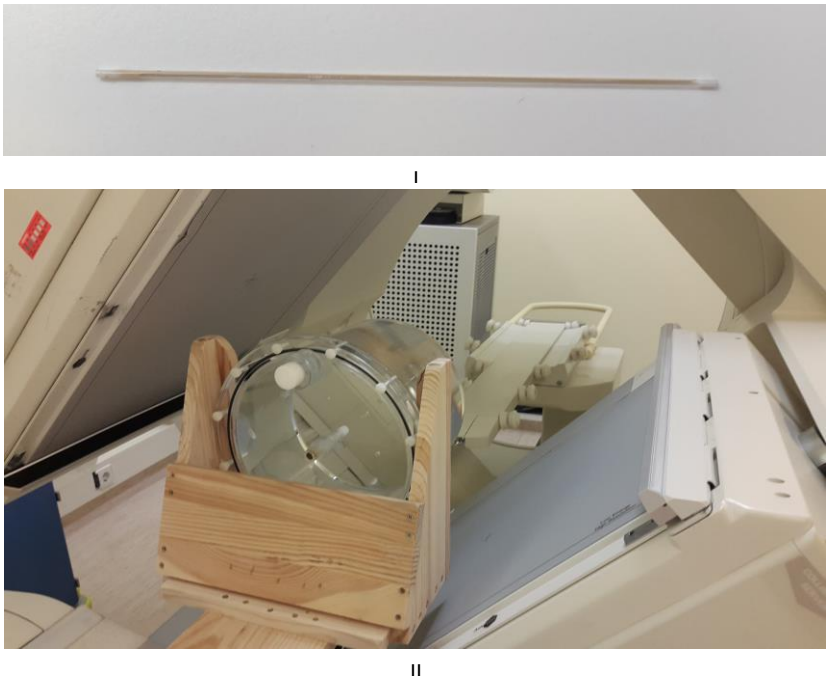

I

II

Figure 22 - (I) Line source with activity uniformly distributed. (II) Jaszczak Phantom with line source used in physical experiment.

For each reconstruction parameters was applied a 2D Gaussian function approximation to create simulated data in order to explore the SPECT resolution (FWHM)[2]. A square ROI was delineated on SPECT slice and the data collected to plot the 2D profile of the experimental data (Figure 23).

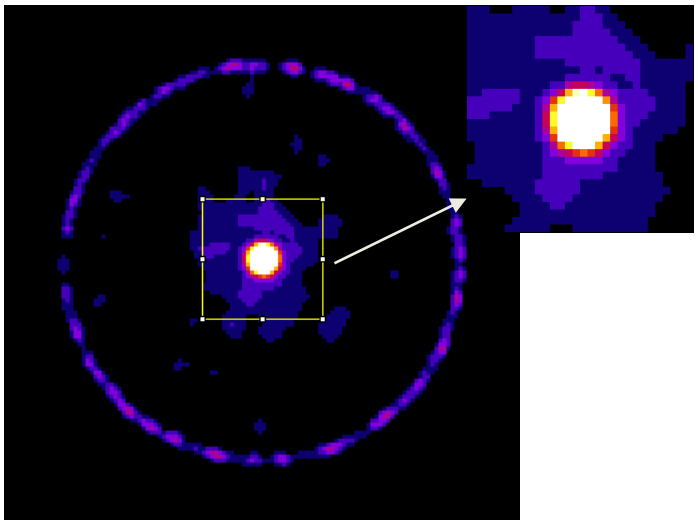

Figure 23 - Axial SPECT slice from experimental measurement.

Image contrast and noise measurements also were obtained from phantom experiment reconstructions. A circular ROI was drawn in hot region and four background ROIs were delineated on the same slice that fell within the physical phantom boundaries on the reconstructed image (Figure 24). The same ROIs and slices were used to analyze all the reconstructed images of the phantom.

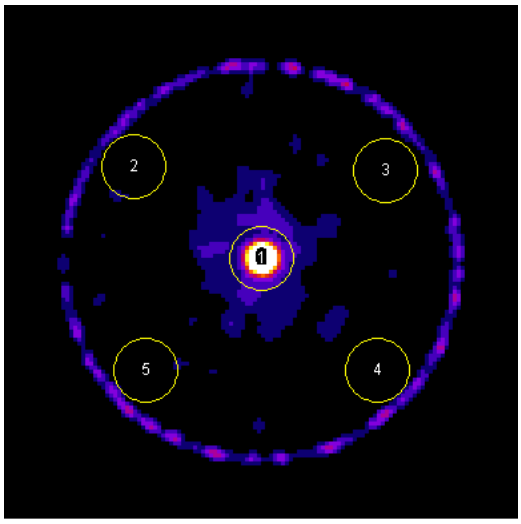

[2] A Gaussian shape seems to the appropriate for FWHM calculation in this situation (Santos *et al* 2008 and Pasciak *et al* 2014).

Figure 24 - Axial SPECT slice from experimental measurement for noise and contrast measurements.

For each reconstructed SPECT volume, contrast recovery coefficients were calculated with Equation 38.

$$\boldsymbol{Contrast}\ (\%) = \left|\frac{C_p - \overline{C_b}}{C_p + \overline{C_b}}\right| \times \mathbf{100} \qquad \textbf{Equation 38}$$

where C_p is the counts in the hot region (ROI_1) and $\overline{C_b}$ is the mean counts in the background ROIs (ROI_2, ROI_3, ROI_4, ROI_5). A measure of image noise was calculated with Equation 39.

$$\boldsymbol{Noise}\ (\%) = \frac{\boldsymbol{STD_b}}{\overline{C_b}} \times \mathbf{100} \qquad \textbf{Equation 39}$$

Here, STD_b is the standard deviation in the background ROIs. The $STD_b$was calculated with Equation 40.

$$\boldsymbol{STD_b} = \sqrt{\frac{1}{N}\sum_{i=1}^{N}(x_i - \overline{x})^2} \qquad \textbf{Equation 40}$$

The counts per voxel are another factor strongly dependent on the method of reconstruction. Hence, the relative SPECT counts in each voxel of the image were converted to absolute activity by normalizing the total counts minus background to the total ^{90}Y administered activity as:

$$\boldsymbol{A_{voxel}} = \boldsymbol{A_{total}} \times \frac{\boldsymbol{C_{voxel}}}{\boldsymbol{C_{total}} + \overline{\boldsymbol{C_b}}} \qquad \textbf{Equation 41}$$

where A_{total} is the present activity in the line source (222 MBq).

Posteriorly, to investigate the feasibility of Bremsstrahlung imaging in a real patient situation, a SPECT reconstruction that presented better results was conducted on a patient undergoing standardized treatment with ^{90}Y-microspheres.

5. Results and Discussion

5.1. Pretreatment imaging and dosimetry

A total of sixty two patients were evaluated for radioembolization after the ^{99m}Tc-MAA procedure and were treated with resin microspheres. The diagnoses included hepatocellular carcinoma, neuroendocrine tumors metastatic to the liver and metastatic liver tumors from other primary tumors including colon, lung, breast or rectal cancer. For all delivered treatments, a retrospective analysis was performed, presented in the Table 11.

Table 11 - Patient characteristics.

Parameters	Data
Sex (*n*)	
Male	45 (72.58%)
Female	17 (27.42%)
Weight (kg)	71.84 ± 14.09
Height (m)	1.69 ± 0.07
Primary tumor (*n*)	
Hepatocellular	23 (37.10%)
Cholangiocarcinoma	21 (33.87%)
Colorectal	4 (6.45%)
Neuroendocrine	4 (6.45%)
Others	10 (16.13%)
Tumor involvement (*n*)	
<25%	23 (37.10%)
25% - 50%	33 (53.23%)
50% - 75%	6 (9.68 %)
75% - 100%	0 (0%)
Lung Shunt Fraction (*n*)	
<5%	20 (32.26%)
5% - 10%	31 (50.00%)
10% - 15%	9 (14.52%)
15% - 20%	2 (3.23%)
Treatment	
Whole liver	48 (77.42%)
Lobar liver	14 (22.58%)
Resin microspheres activity (GBq)	1.70 ± 0.42

Between 2011 and 2017, these treatments were delivered, and the injected activity was calculated with BSA method. Lobar and whole liver treatments were analyzed separately as function of tumor involvement (Figure 25). The injected activities in whole liver treatments present a relative shorter range, where the maximum activity was 2.47 GBq and the lowest activity was 1.24. While the maximum activity administered in lobar treatment was 1.93 GBq and the minimum 0.65 GBq. In each graph was represented the mean ± standard deviation of the analyzed data.

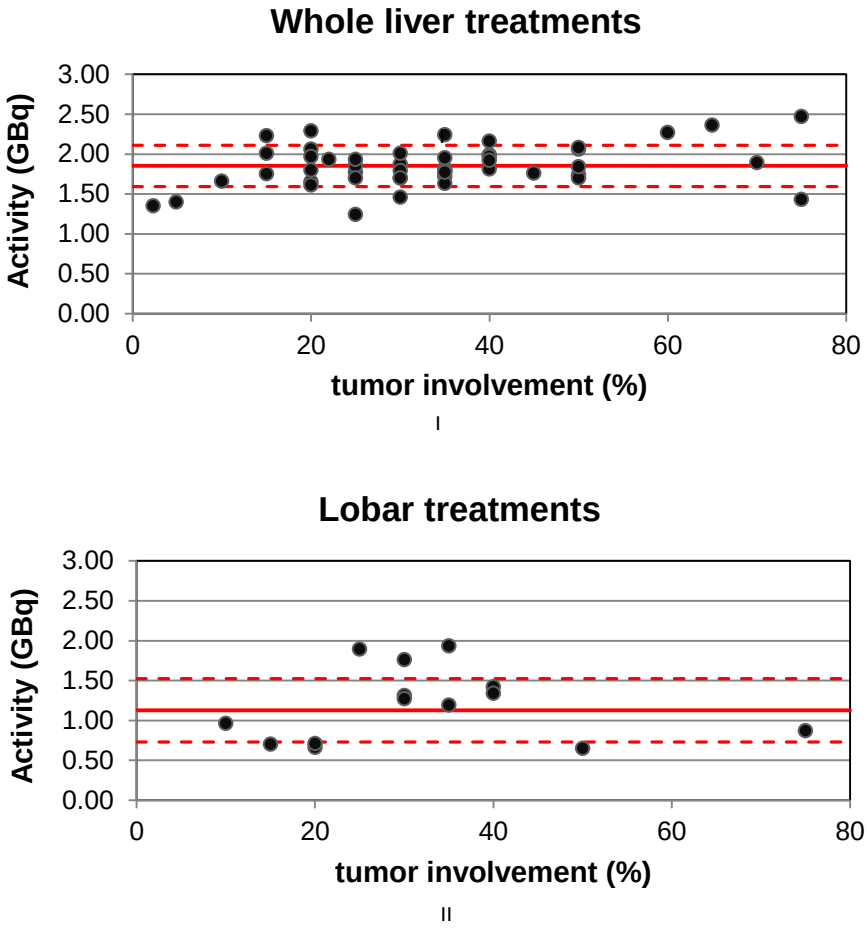

Figure 25 - Calculated activity from BSA method as function of tumor involvement. (I) For whole liver treatments. (II) For lobar treatments.

In this retrospective study, eleven evaluations presented a shunt greater than 10%. For these patients, with significant pulmonary shunting, the prescribed activity was reduced according to recommendations of the manufacturer (20% reduction for LSF: 10% - 15%; 40% reduction for LSF: 15% - 20%). The separated analysis of whole liver and lobar treatments as function of tumor involvement is presented in Figure 26.

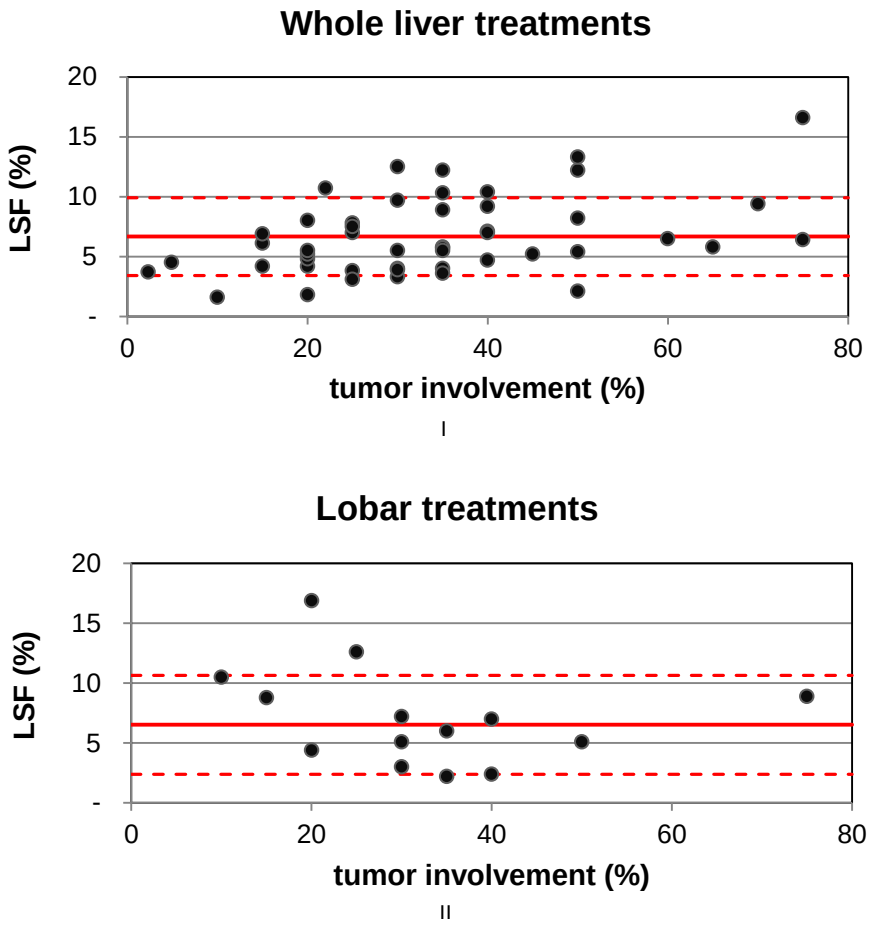

Figure 26 - LSF as function of tumor involvement. (I) For whole liver treatments. (II) For lobar treatments.

In clinical routine, the injected activity was calculated with the BSA method. The idea is to evaluate some cases to understand the influence of the method used to calculate the activity.

The first case study is a patient with a hepatocellular carcinoma, the most frequent treated pathology, involving more than 30% of the evaluations. This patient presented a voluminous HCC infiltrating almost the entire right lobe. After pre-treatment with ^{99m}Tc-MAA a pulmonary shunt fraction of 13% forced the reduction of activity to be administered. With ^{99m}Tc-MAA/SPECT it is also possible see accumulated ^{99m}Tc at the periphery of the lesion in the right lobe. Table 12 summarizes the tumor volume, LSF, administered ^{90}Y activity, and lung, liver, and tumor dosimetry in each target volume, calculated from PM and BSA method.

Table 12 - Summary of the characteristics of the case 1.

CASE 1		
Pathology: Hepatocellular Carcinoma LSF: 13.10 % Tumor involvement: 34 % T/N: 2.74		
	Partition Method	**BSA Method**
Activity to be administered GBq)	**2.65**	**1.27**
Activity Normal Liver (GBq)	0.96	0.46
Dose Normal Liver (Gy)	50.00	23.91
Activity Tumor (GBq)	1.35	0.65
Dose Tumor (Gy)	136.81	65.42
Activity Lung (GBq)	0.35	0.17
Dose Lung (Gy)	17.27	8.26

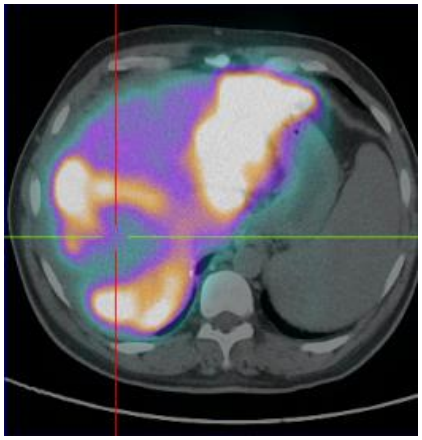

Patient 2 presented NET metastases involving whole liver. Despite presenting pulmonary metastases, the lesions are well defined in CT scan. That way, the ROI to delineate the tumor in ^{99m}Tc-MAA/SPECT was conducted with the help of a CT scan without major difficulties. The obtained results are presented in Table 13. The previous calculated activity by BSA method, as well the activity recalculated, this time by PM, and the corresponding doses of the normal liver, tumor and lung are also shown in the table.

Table 13 - Summary of the characteristics of the case 2.

CASE 2		
Pathology: Neuroendocrine tumor LSF: 6.50 % Tumor involvement: 37% T/N: 4.72		
	Partition Method	**BSA Method**
Activity to be administered GBq)	**7.40**	**2.04**
Activity Normal Liver (GBq)	1.84	0.51
Dose Normal Liver (Gy)	50.00	13.79
Activity Tumor (GBq)	5.08	1.40
Dose Tumor (Gy)	236.00	65.06
Activity Lung (GBq)	0.48	0.13
Dose Lung (Gy)	23.89	6.59

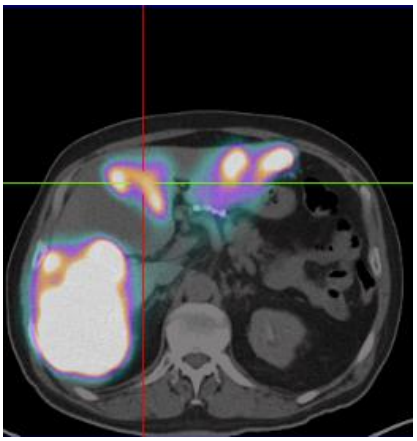

Patient 3 presented a pancreatic cancer with multiple (diffuse) metastases in both lobes of the liver. ^{99m}Tc-MAA distribution not always reached lesions and presented small metastasis with ill-defined margins. This is a problem in PM due to tumor ROI delineation. In Table 14 are presented the patient characteristics.

Table 14 - Summary of the characteristics of the case 3.

CASE 3		
Pathology: Pancreatic cancer LSF: 6.90 % Tumor involvement: 6.48 T/N: 34.10		
	Partition Method	**BSA Method**
Activity to be administered GBq)	**6.90**	**1.92**
Activity Normal Liver (GBq)	1.91	0.53
Dose Normal Liver (Gy)	50.00	13.96
Activity Tumor (GBq)	4.51	1.26
Dose Tumor (Gy)	1704.95	475.88
Activity Lung (GBq)	0.48	0.13
Dose Lung (Gy)	23.63	6.60

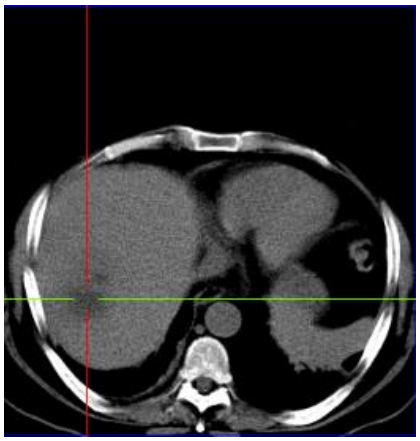

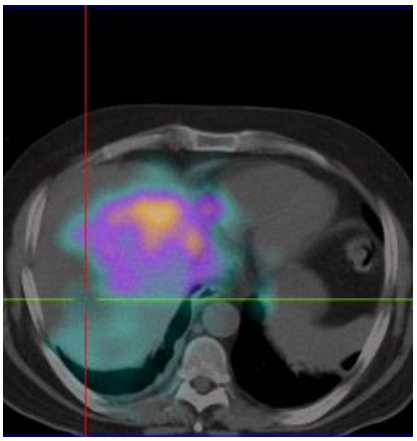

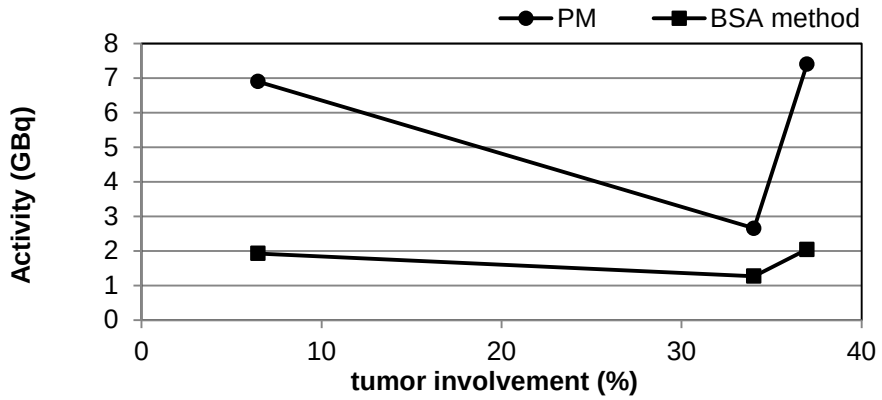

Figure 27 - Relative difference in calculated activities with PM and BSA method as a function of tumor involvement.

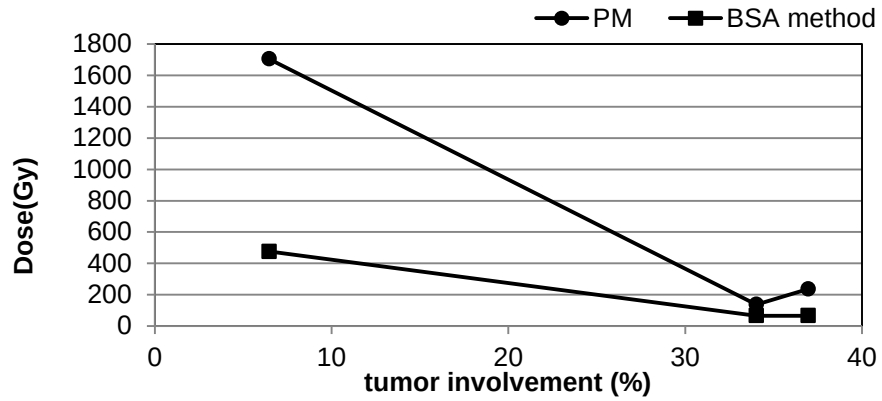

Figure 28 - Comparison between absorbed doses to tumor obtained from PM and BSA method as a function of tumor involvement.

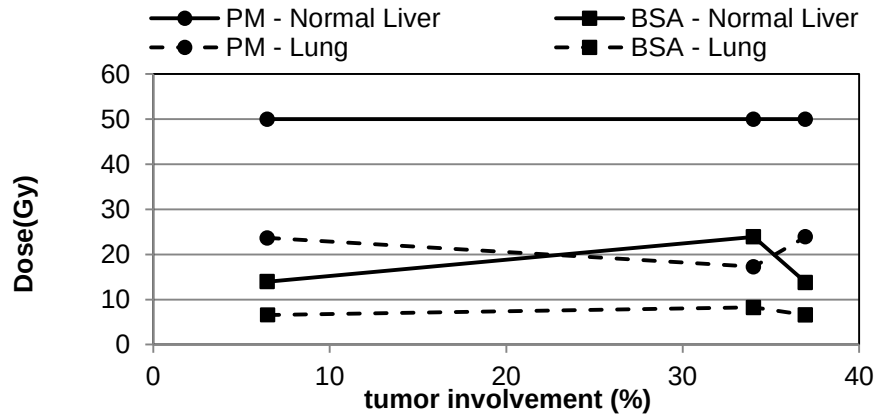

Figure 29 - Comparison between absorbed doses to normal liver and lung obtained from PM and BSA method as a function of tumor involvement.

The three patients in study received resin ^{90}Y-microspheres with the activity of radiation determined by the BSA method. The percentage of microspheres that passes from the liver arterial system through to the pulmonary capillary beds was relatively low, with all patients presenting a LSF below 20%. Only the patient 1 had a LSF above 10% and following the recommendations of Sirtex manufacture, the total activity was reduced in 20%. In addition, the patient 1 was treated to the right lobe, reducing the activity further. The other two patients received the planned activity.

A major challenge is determining the optimal activity of resin microspheres for an individual patient in advance of the procedure. And it is expected that patients may benefit greatly from individualized treatment planning. In these three cases under study, the partition method was applied to calculate the injected activity and, subsequently evaluating the dose which could possibly be delivered to the normal liver, lung and tumor. Comparing the initial calculated activity by BSA method with calculated activity by PM is possible to verify a considerable difference. In relation to the dose in the normal liver was established a limit of 50 Gy for all patients.

In the first case, a lobar treatment, the calculated activity based on PM is 208% higher than BSA activity. Absorbed dose to the tumor is higher in partition method, with 137 Gy, while with the BSA method the tumor only received 66 Gy. In both cases PM and BSA method the dose to the lung was below than 25 Gy.

In the second case, a whole liver treatment with a tumor with well-defined margins, the PM activity is 363% higher than activity calculated using the BSA method. Thus, maintaining the limit for the normal liver, in 50 Gy, the absorbed dose to tumor was 236 Gy based on PM, and only 65 Gy by the BSA method. Once again, the dose to the lung has not exceeded the upper limit.

In the third case, a patient with multiple metastases in the whole liver, the segmentation of the tumor and non-tumor liver was complicated. This is because for very small tumors may not be possible an accurate delineation of the tumor, harming the T/N ratio estimation. Thus, the activity calculated according to PM is 360% higher than BSA activity. However, with the result of the T/N ratio, the absorbed dose to tumor is very high: 1705 Gy by PM, and 476 Gy from BSA method. In this situation, the BSA method should be used given that is suited for small lesions especially with diffuse margins.

The partition method usually applies to solitary hepatic tumors, although, can also be applies in multifocal lesions if each can be adequately localized (Case 1 and Case 2). Thus, relatively few metastases will qualify for partition model planning because

accurate partitioning of the tumor compartment and normal liver not always feasible, especially in patients with disseminated disease including diffuse, heterogeneous, or multiple metastasis (Case 3). However, it is important to keep in mind that the PM should be the preferred method for activity calculation of ^{90}Y-microspheres for every patient.

Relative differences in calculated activity with PM and BSA method as function of tumor involvement was presented in Figure 27. As well as the absorbed doses by the relevant tissues, as tumor (Figure 28), normal liver and lungs (Figure 29), obtained from PM and BSA method.

5.2. Evaluation of Bremsstrahlung imaging

After radioembolization with ^{90}Y resin microspheres, Bremsstrahlung images of the abdomen are obtained using a gamma camera. These images are performed to verify the distribution of ^{90}Y-microspheres to the extrahepatic tissue and liver. However, Bremsstrahlung imaging suffers from poor resolution. One aim of this study is to improve ^{90}Y Bremsstrahlung SPECT images.

5.2.1. Phantom and Patient study

SPECT phantom data was acquired using the same protocol for patient acquisition and was performed several reconstruction protocols. Table 15 shows the results of the reconstruction methods evaluated.

Table 15 - Phantom reconstruction parameters.

Reconstruction parameters	$FWHM_x$ (mm)	$FWHM_y$ (mm)	Contrast (%)	Noise (%)	A_{voxel} (MBq)
FBP, btw, 0.2, 4	20.22	19.98	90.49	0.33	0.74
FBP, btw, 0.4, 5	13.34	12.89	88.96	0.49	1.20
FBP, btw, 0.6, 6	13.05	12.51	82.86	0.57	0.93
2D OSEM, 4i2s	14.45	13.90	89.62	0.26	1.45
2D OSEM, 8i4s	8.59	8.36	93.74	0.69	3.54
2D OSEM, 16i8s	5.81	5.98	92.91	1.53	5.62
2D OSEM, 4i2s, 6mm Gaussian filter	15.45	14.90	88.35	0.20	1.31
2D OSEM, 8i4s, 6mm Gaussian filter	9.15	9.10	93.02	0.55	3.04
2D OSEM, 16i8s, 6mm Gaussian filter	6.65	6.76	92.74	0.95	4.60
2D OSEM, 4i16s, 10mm Gaussian filter	9.05	9.10	91.10	0.48	2.83
2D OSEM, 5i8s, 10mm Gaussian filter	9.99	9.96	91.20	0.43	2.45
2D OSEM, 8i4s, 10mm Gaussian filter	10.22	10.34	91.40	0.42	2.33
2D OSEM, 10i16s, 10mm Gaussian filter	7.87	8.10	92.19	0.62	2.97
2D OSEM, 15i16s, 10mm Gaussian filter	7.53	1.98	91.30	0.61	3.57
2D OSEM, 4i2s, 12mm Gaussian filter	17.40	18.12	85.80	0.03	1.01
2D OSEM, 8i4s, 12mm Gaussian filter	11.25	12.08	91.45	0.42	2.03
2D OSEM, 16i8s, 12mm Gaussian filter	8.95	9.14	91.34	0.49	2.72

Two algorithms are presented, the FBP and MLEM (OSEM) algorithm. In the FBP algorithm was changed the cut-off frequency and the filter order. This algorithm was preferred, in clinical practice, because it was computationally faster. However, it has several flaws, where to improve the noise compromise image resolution. For example, a first application of FBP (0.2, 4) presents a good contrast and noise results, but poor resolution (approximately 20 mm). In contrast, to improve the image resolution there is a loss of contrast and noise.

The second algorithm tested was an iterative algorithm requiring also an optimization to provide the best trade-off between noise/contrast and image resolution. The OSEM algorithm was performed with and without Gaussian filters changing the number of iterations and subsets. For reconstructive OSEM method without Gaussian filter with 8 iterations and 4 subsets present the best trade-off between noise/contrast and image resolution. The accuracy increases when applying a Gaussian filter. From Table 15 it is still possible to verify that the poor contrast occurs if the number of subsets and iterations is small. An increase of the noise level occurs with a higher number of iterations. Thus, the noise level in the SPECT images may to be substantially reduced when reconstructed with 8 iterations, 4 subsets and Gaussian filter of 10 mm.

Image contrast and noise is a measure of differences in the counts (activity) concentration. Thus the activity per voxel depends on the reconstruction algorithm parameters. Increasing the noise also increases the A_{voxel}.

Figure 30, Figure 31 and Figure 32 show a transaxial 2D profile from three examples of reconstruction parameters. The first is a FBP reconstruction with an image resolution of 13 mm and some noise. The second example is an iterative reconstruction without Gaussian filter, 16 iterations and 8 subsets, which, although presenting an optimal resolution and image contrast, have a large noise level. In the last example, the reconstruction provides the best trade-off between noise/contrast and image resolution.

The results of reconstructed images of the patient study are shown in Table 16, Table 17 and Table 18. For each case in study was applied the reconstruction parameters showed in Figure 30, Figure 31 and Figure 32. The liver is clearly seen in the images, however, the last reconstruction method, a OSEM with 8 iterations, 4 subsets and 10 mm Gaussian filter present the best results.

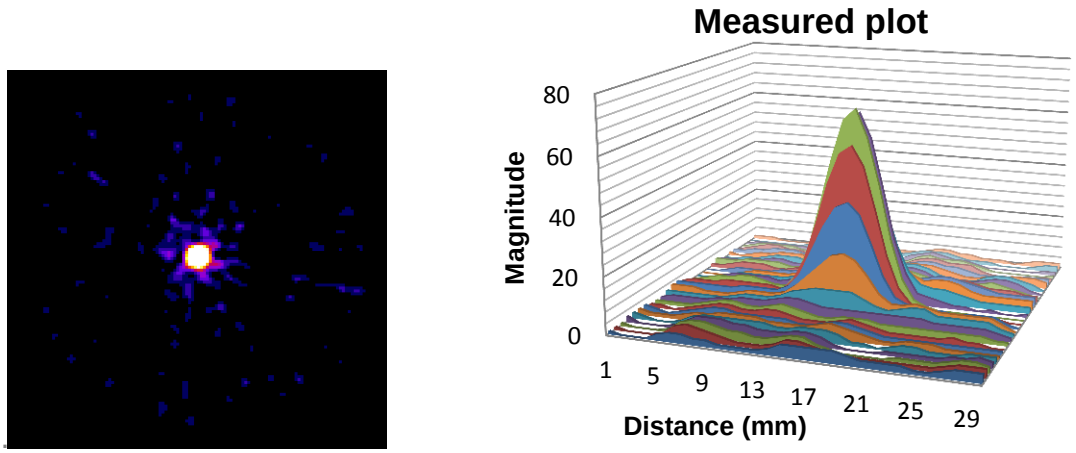

I II

Figure 30 - (I) Representative slice from FBP reconstruction (Bwt, 0.4, 5). (II) 2D plot from axial profile of a ^{90}Y line source in water.

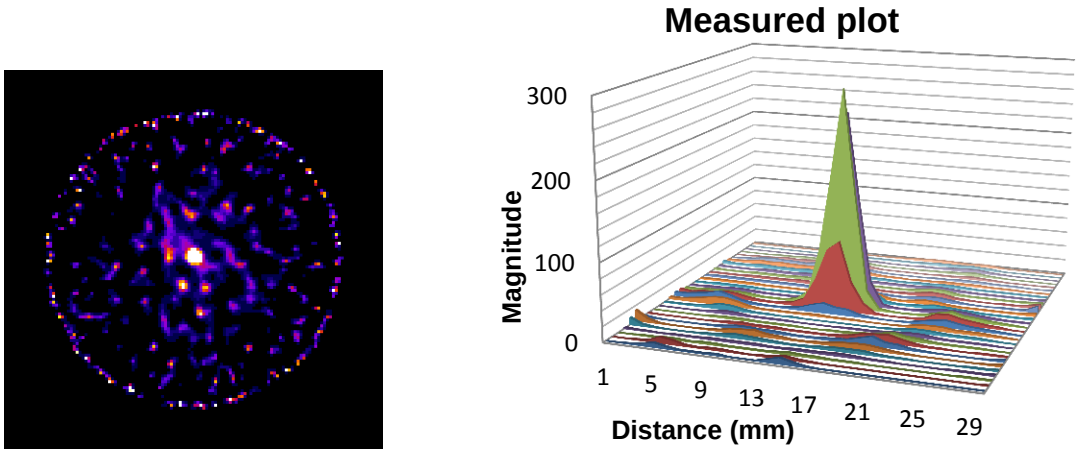

I II

Figure 31 - (I) Representative slice from iterative reconstruction (2D OSEM, 16i8s). (II) 2D plot from axial profile of a ^{90}Y line source in water. (III) Comparative Gaussian profile.

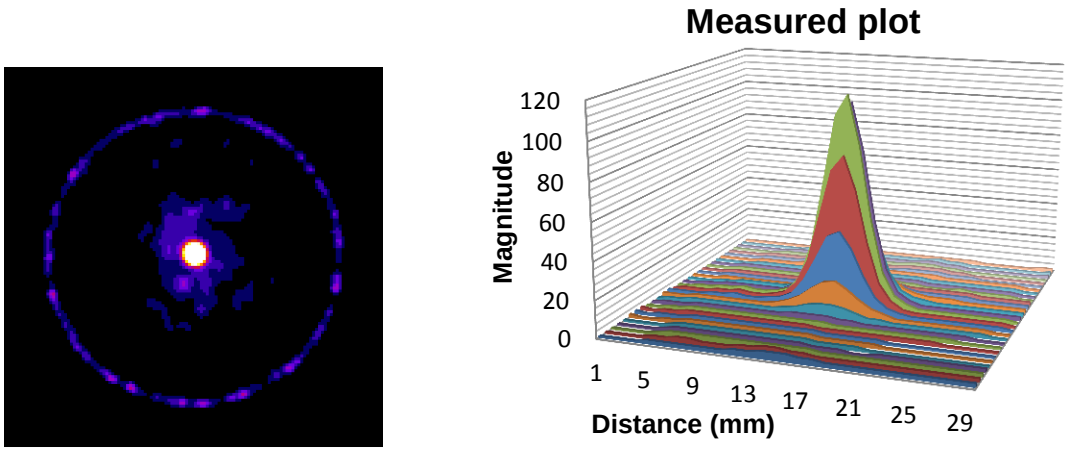

I II

Figure 32 - (I) Representative slice from iterative reconstruction (2D OSEM, 8i4s, 10mm Gaussian Filter). (II) 2D plot from axial profile of a ^{90}Y line source in water.

Table 16 - Transversal slices of the patient 1 measurement.

CASE 1		
FBP 0.4, 5	**OSEM 16i8s**	**OSEM 8i4s, 10mm Gaussian filter**
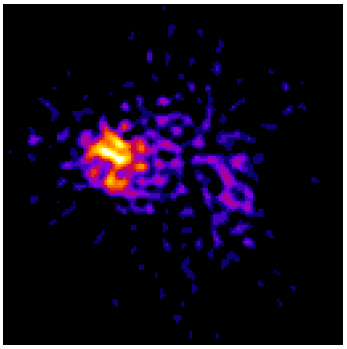	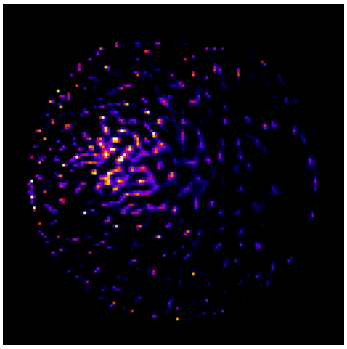	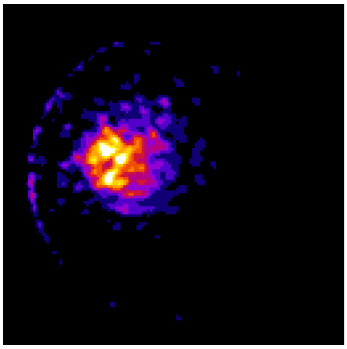

Table 17 - Transversal slices of the patient 2 measurement.

CASE 2		
FBP 0.4, 5	**OSEM 16i8s**	**OSEM 8i4s, 10mm Gaussian filter**
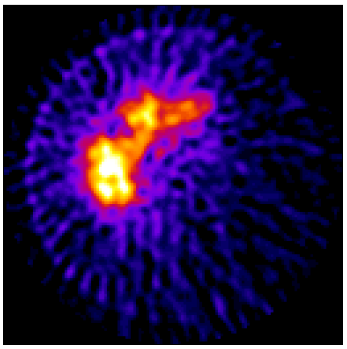	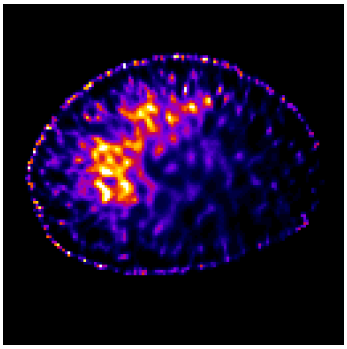	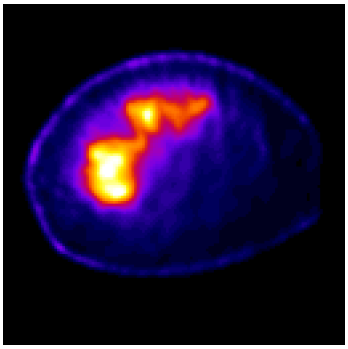

Table 18 - Transversal slices of the patient 3 measurement.

CASE 3		
FBP 0.4, 5	**OSEM 16i8s**	**OSEM 8i4s, 10mm Gaussian filter**
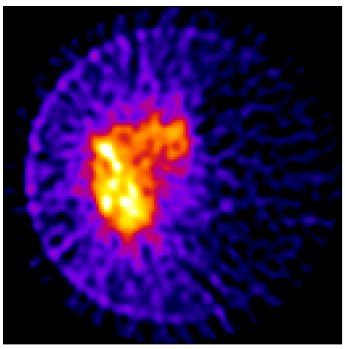	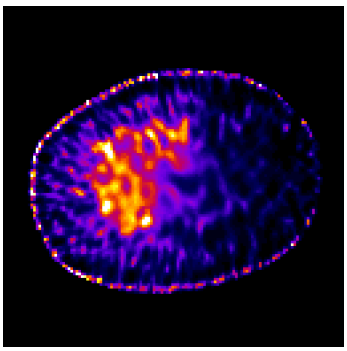	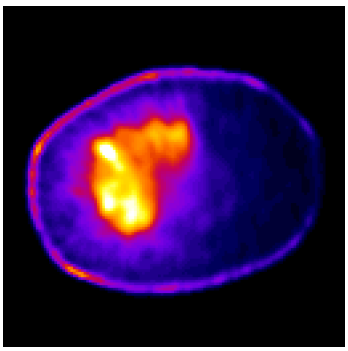

6. Conclusion and Future Work

Therapeutic nuclear medicine is developing rapidly as an alternative choice of treatment in oncology. Particularly, the radioembolization with ^{90}Y-microspheres has been a powerful tool to achieve regional tumor response and disease control in hepatic malignancy of various origins. For a long time, has been used a fixed activity or activity based in the body surface area. However, caution regarding patient selection, treatment preparation including an appropriate dosimetry, and performance is particularly important to prevent toxicity to be associated with this treatment. Thus, the shift towards personalized radionuclide therapy is an inevitable trend. Stabin for *Cancer Biotherapy and Radiopharmaceuticals* (2008) remarks: *Treating all nuclear medicine patients with a single, uniform method of activity administration amounts to consciously choosing that these patients be treated with a lower standard of care than patients who receive radiation externally for cancer treatments* [111].

Using a ^{99m}Tc-MAA scan, it is possible to determine the desired activity of ^{90}Y-microspheres to be injected. In addition, its biodistribution can provide a predictive dose distribution within the tumor volume and organs at risk (normal liver and lungs). To administer an optimal activity for each patient is needed an improved activity calculation method based on accurate physiology parameters. The partition method allows calculation of the administered activity in the target volume, the healthy liver volume and the lungs. This study included only three cases, but these patients represent the cohort of patients indicated for radioembolization. For these patients, BSA method remained conservative relative to the activities to be administered, that is, the activities obtained by BSA method delivered a sub-therapeutic dose. Meanwhile, the PM proposes an activity calculation method that includes patient-specific characteristics such as tumor, normal liver and lung volumes and T/N ratio. Thus, the accurate radiation dose from PM provides a safe, effective and personalized radiation therapy planning.

In radionuclide therapy, there is the need to measure the distribution of the ^{90}Y, that is, through Bremsstrahlung imaging, *in vivo,* usually performed by SPECT imaging. Bremsstrahlung images after radioembolization treatment are useful in evaluation the intrahepatic distribution of ^{90}Y and detecting possible extrahepatic activity. To ensure a better image quality several reconstruction methods were analyzed. The results presented in Table 15 as well as the both phantom and patient studies showed that a

trade-off between noise/contrast and image resolution can be obtained with an iterative algorithm with a Gaussian filter, 8 iterations and 4 subsets.

In conclusion, an implementation of the individualized treatment planning is fundamental. Thus, the Partition Model is preferable in relation to BSA method because it is based on accurate physiologic parameters. Prescription of activity using BSA method usually results in an under-treatment in selected patient.

6.1. Future work

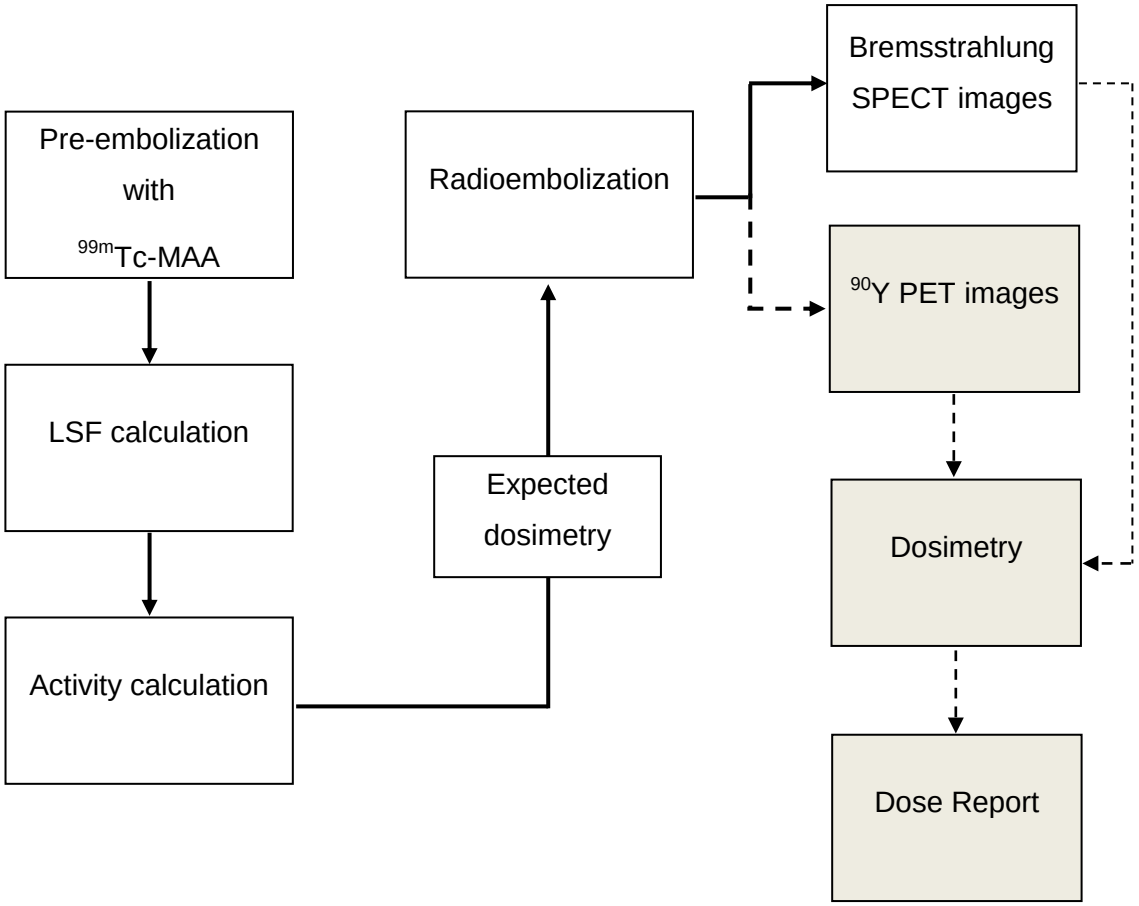

Figure 33 - Schematic of general procedure of radioembolization.

SPECT imaging after post-therapy can also be useful for dose verification and validation of the treatment planning. Unfortunately, the low photon yield and continuous nature of the Bremsstrahlung X-ray spectrum limit the quantitative accuracy of ^{90}Y Bremsstrahlung SPECT.

Future ^{90}Y radioembolization dosimetry techniques are based on today's emerging technologies. ^{90}Y PET was recently shown to be feasible in phantoms and patients and

may be an interesting alternative to Bremsstrahlung SPECT allowing direct imaging of ^{90}Y-microspheres. Although, ^{90}Y is predominantly a β^- emitter, where decays to the fundamental level of ^{90}Zr (99.99%), a lower probability branch (0.01%) follows another β^- decay to the first ^{90}Zr excited state (Figure 34). The following $0^+ – 0^+$ transition 0f ^{90}Zr happen via internal par production β^- β^+ with an even smaller branching ratio (approximately 32 x 10^{-6}). Although it results in a weak signal, it is detectable by PET imaging.

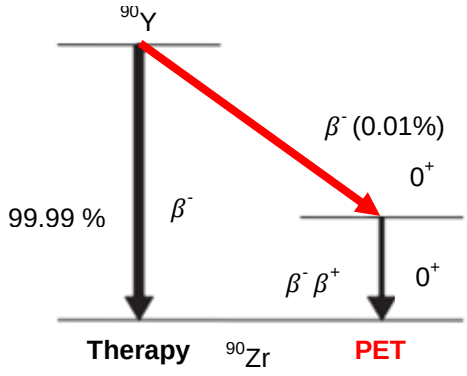

Figure 34 - Simplified decay scheme for ^{90}Y.

The conventional PET scanners, although can be superior over Bremsstrahlung SPECT need longer acquisition times for dosimetry calculation due to the loss of contrast. In alternative, ^{90}Y PET is feasible with the help of the time-of-flight information. The concept of TOF means simply that for each annihilation event, the precise time that each of coincident photon is detected and calculated the difference. However, PET imaging of ^{90}Y continues to present challenges including attenuation and scatter correction.

In September of 2017, Nuclear Medicine Service of IPO-Porto purchases a new TOF PET/CT (Biograph mCT Flow, Siemens Healthcare, Germany) and was possible an acquisition of a patient treated for liver using ^{90}Y resin microspheres. Despite of the low positron abundance and a low acquisition time (approximately 12 minutes) it demonstrates satisfactory results. In the future, improvements in the ^{90}Y PET are necessary and indispensable.

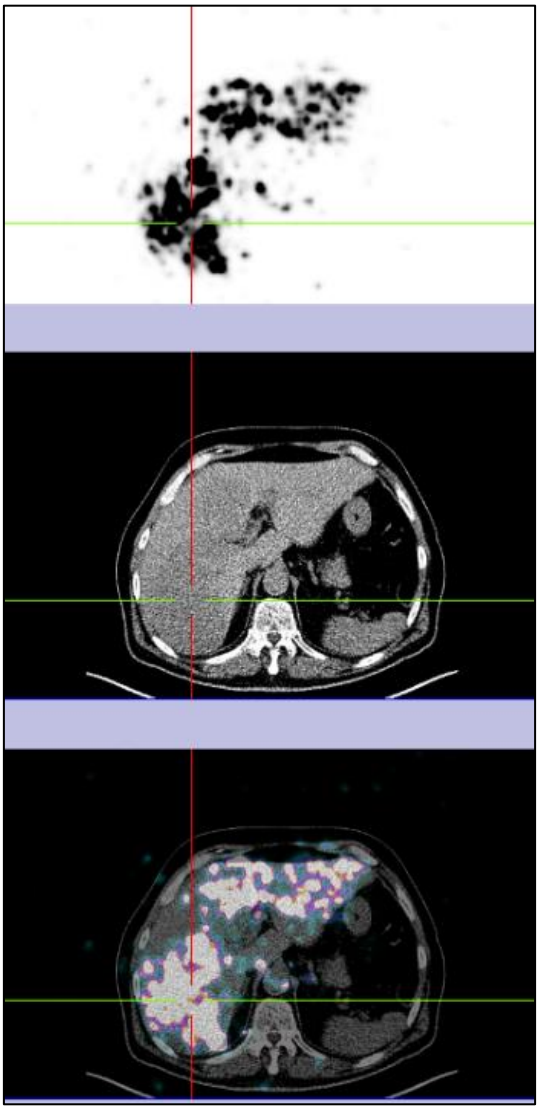

Figure 35 - ^{90}Y TOF PET/CT image.

7. Bibliography

1. Torre, L. a. *et al.* Global Cancer Statistics, 2012. *CA a cancer J. Clin.* **65,** 87–108 (2015).

2. American Cancer Society. Key Statistics About Liver Cancer. at <https://www.cancer.org/cancer/liver-cancer/about/what-is-key-statistics.html>

3. Garin, E. *et al.* Utility of Quantitative Tc-MAA SPECT/CT for yttrium-Labelled Microsphere Treatment Planning: Calculating Vascularized Hepatic Volume and Dosimetric Approach. *Int. J. Mol. Imaging* (2011). doi:10.1155/2011/398051

4. Eftekhari, A., Worsley, D., Klass, D. & Liu, D. M. Technical note : simultaneous 90 Y and 99m Tc-MAA injection for two-stage selective internal radiation therapy (SIRT) of liver metastases. *Transl. Cancer Res. J.* **3,** 138–145 (2014).

5. Wang, S. C. *et al.* Clinical care and technical recommendations for 90yttrium microsphere treatment of liver cancer. *Journal of Medical Imaging and Radiation Oncology* **54,** 178–187 (2010).

6. Toohey, R. E., Stabin, M. G. & Watson, E. E. The AAPM/RSNA Physics Tutorial for Residents Internal Radiation Dosimetry: Principles and Applications. *RadioGraphics* **20,** 533–546 (2000).

7. Braat, A. J. a T. *et al.* 90Y Hepatic Radioembolization: An Update on Current Practice and Recent Developments. *J. Nucl. Med.* **56,** 1079–1087 (2015).

8. Kao, Y. H., Tan, E. H., Ng, C. E. & Goh, S. W. Clinical implications of the body surface area method versus partition model dosimetry for yttrium-90 radioembolization using resin microspheres: A technical review. *Ann. Nucl. Med.* **25,** 455–461 (2011).

9. Lau, W. Y. *et al. Patient selection and activity planning guide for selective internal radiotherapy with yttrium-90 resin microspheres*. *International Journal of Radiation Oncology Biology Physics* **82,** (2012).

10. Wondergem, M. *et al.* 99mTc-Macroaggregated Albumin Poorly Predicts the Intrahepatic Distribution of 90Y Resin Microspheres in Hepatic Radioembolization. *J. Nucl. Med.* **54,** 1294–1301 (2013).

11. Dieudonne, A. *et al.* Clinical Feasibility of Fast 3-Dimensional Dosimetry of the Liver for Treatment Planning of Hepatocellular Carcinoma with 90Y-Microspheres. *J. Nucl. Med.* **52,** 1930–1937 (2011).

12. Cherry, S., Sorenson, J. & Phelps, M. *Physics in Nuclear Medicine*. (Elsevier Health Sciences, 2012).

13. Ott, R. J. Imaging technologies for radionuclide dosimetry. *Phys. Med. Biol.* **41,** 1885–1894 (1996).

14. D'Asseler, Y. Advances in SPECT imaging with respect to radionuclide therapy. *Quarterly Journal of Nuclear Medicine and Molecular Imaging* **53,** 343–347 (2009).

15. Singh, M. & Waluch, V. Physics and instrumentation for imaging in-vivo drug distribution. *Advanced Drug Delivery Reviews* **41,** 7–20 (2000).

16. Saha, G. B. *Physics and radiobiology of nuclear medicine*. *Physics and Radiobiology of Nuclear Medicine* (Springer, 2006). doi:10.1007/978-1-4614-4012-3

17. Attix, F. H. *Introduction to Radiological Physics and Radiation Dosimetry*. (Wiley-VCH Verlag GmbH & Co. KGaA, 2004). doi:10.1002/9783527617135

18. *Radiation Oncology Physics: A Handbook for Teachers and Students*. *International Atomic Energy Agency* (2005). doi:10.1038/sj.bjc.6604224

19. Turner, J. E. *Atoms, Radiation, and Radiation Protection*. (Wiley-VCH Verlag GmbH & Co. KGaA, 2007).

20. Ljungberg, M. & Gleisner, K. S. Personalized Dosimetry for Radionuclide Therapy Using Molecular Imaging Tools. *Biomedicines* **4,** 1–21 (2016).

21. *Practical Nuclear Medicine*. (Springer, 2005). doi:10.1007/b136183

22. Peterson, T. E. & Furenlid, L. R. SPECT detectors: the Anger Camera and beyond. *Phys. Med. Biol.* **56,** R145–R182 (2011).

23. Madsen, M. T. Recent Advances in SPECT Imaging. *J Nucl Med* **48,** 661–673 (2007).

24. Knoll, P. *et al.* Comparison of advanced iterative reconstruction methods for SPECT/CT. *Z. Med. Phys.* **22,** 58–69 (2012).

25. Bruyant, P. P. Analytic and iterative reconstruction algorithms in SPECT. *J. Nucl. Med.* **43,** 1343–1358 (2002).

26. Van Laere, K., Koole, M., Lemahieu, I. & Dierckx, R. Image filtering in single-photon emission computed tomography: Principles and applications. *Comput. Med. Imaging Graph.* **25,** 127–133 (2001).

27. Hutton, B. F., Nuyts, J. & Zaidi, H. in *Quantitative Analysis in Nuclear Medicine Imaging* (ed. Zaidi, H.) 107–140 (Springer US, 2006). doi:10.1007/b107410

28. International Atomic Energy Agency. *Yttrium-90 and Rhenium-188 Radiopharmaceuticals for Radionuclide Therapy*. *IAEA Radioisotopes and Radiopharmaceuticals Series* (IAEA, 2015).

29. Rong, X., Du, Y. & Frey, E. C. A method for energy window optimization for quantitative tasks that includes the effects of model-mismatch on bias: application to Y-90 bremsstrahlung SPECT imaging. *Phys. Med. Biol.* **57,** 3711–3725 (2012).

30. Zukotynski, K., Fahey, F., Jadvar, H. & Capala, J. Targeted Radionuclide Therapy: Practical Applications and Future Prospects. *Biomark. Cancer* **8,** 35 (2016).

31. Gudkov, S. V., Shilyagina, N. Y., Vodeneev, V. a. & Zvyagin, A. V. Targeted radionuclide therapy of human tumors. *Int. J. Mol. Sci.* **17,** 1–19 (2016).

32. Eary, J. F. & Brenner, W. *Nuclear Medicine Therapy*. (Informa healthcare USA, Inc, 2007).

33. Yeong, C., Cheng, M. & Ng, K. Therapeutic radionuclides in nuclear medicine : current and future prospects. **15,** 845–863 (2014).

34. Stabin, M. G. *Radiation protection and dosimetry*. *Radiation Protection and Dosimetry* (2007). doi:10.1007/978-0-387-49983-3

35. Pillai, M. R. A. *Metallic Radionuclides and Therapeutic Radiopharmaceuticals*. (Institute of Nuclear Chemister and Technology, 2010).

36. Kassis, A. I. Molecular and Cellular Radiobiological Effects of Auger Emitting Radionuclides. **143,** 241–247 (2011).

37. Jackson, M. R., Falzone, N. & Vallis, K. a. Advances in anticancer radiopharmaceuticals. *Clin. Oncol.* **25,** 604–609 (2013).

38. Kassis, A. I. & Adelstein, S. J. Radiobiologic principles in radionuclide therapy. *J. Nucl. Med.* **46 Suppl 1,** 4S–12S (2005).

39. Institute of Medicine and National Research. *Advancing Nuclear Medicine Through Innovation*. (National Academies Press, 2007). doi:10.17226/11985

40. Gabriel, M. Radionuclide therapy beyond radioiodine. *Wiener Medizinische Wochenschrift* **162,** 430–439 (2012).

41. Stokkel, M. P. M., Handkiewicz Junak, D., Lassmann, M., Dietlein, M. & Luster, M. EANM procedure guidelines for therapy of benign thyroid disease. *Eur. J. Nucl. Med. Mol. Imaging* **37,** 2218–2228 (2010).

42. Luster, M. *et al.* Guidelines for radioiodine therapy of differentiated thyroid cancer. *Eur. J. Nucl. Med. Mol. Imaging* **35,** 1941–1959 (2008).

43. Giammarile, F., Chiti, A., Lassmann, M., Brans, B. & Flux, G. EANM procedure guidelines for 131I-meta-iodobenzylguanidine (131I-mIBG) therapy. *Eur. J. Nucl. Med. Mol. Imaging* **35,** 1039–1047 (2008).

44. Kayano, D. & Kinuya, S. Iodine-131 metaiodobenzylguanidine therapy for neuroblastoma: Reports so far and future perspective. *Sci. World J.* **2015,** 1–9 (2015).

45. Wheat, J. M., Currie, G. M., Davidson, R. & Kiat, H. Radionuclide therapy. *Radiogr.* **58,** 53–59 (2011).

46. Ersahin, D., Doddamane, I. & Cheng, D. Targeted radionuclide therapy. *Cancers (Basel).* **3,** 3838–3855 (2011).

47. Stanciu, A. E. Radionuclides in Targeted Therapy of Cancer. *Rev. Roum. Chim.* **57,** 5–13 (2012).

48. Parker, C. *et al.* Alpha Emitter Radium-223 and Survival in Metastatic Prostate Cancer. *N. Engl. J. Med.* **369,** 213–223 (2013).

49. Tennvall, J. & Brans, B. EANM procedure guideline for 32P phosphate treatment of myeloproliferative diseases. *Eur. J. Nucl. Med. Mol. Imaging* **34,** 1324–1327 (2007).

50. De Jong, M., Breeman, W. A. P., Valkema, R., Bernard, B. F. & Krenning, E. P. Combination radionuclide therapy using 177Lu- and 90Y-labeled somatostatin analogs. *J. Nucl. Med.* **46,** 13S–17S (2005).

51. Monroy-Guzman, F., Jimenez Barreiro, F., Salinas, E. J. & Treviño, A. L. V. Radiolanthanides Device Production. *World J. Nucl. Sci. Technol.* **5,** 111–119 (2015).

52. Lehenberger, S. *et al.* The low-energy β - and electron emitter 161Tb as an alternative to 177Lu for targeted radionuclide therapy. *Nucl. Med. Biol.* **38,** 917–924 (2011).

53. Baum, R. P. *et al.* [177 Lu-DOTA] 0 -D-Phe 1 -Tyr 3 -Octreotide (177 Lu-DOTATOC) For Peptide Receptor Radiotherapy in Patients with Advanced Neuroendocrine Tumours: A Phase-II Study. *Theranostics* **6,** 501–510 (2016).

54. Ito, S. *et al.* 90Y bremsstrahlung emission computed tomography using gamma cameras. *Ann. Nucl. Med.* **23,** 257–267 (2009).

55. Gulec, S. a & Siegel, J. a. Posttherapy Radiation Safety Considerations in Radiomicrosphere Treatment with 90 Y-Microspheres. *J. Nucl. Med.* **48,** 2080–2086 (2007).

56. Giammarile, F. *et al.* EANM procedure guideline for the treatment of liver cancer and liver metastases with intra-arterial radioactive compounds. *Eur. J. Nucl. Med. Mol. Imaging* **38,** 1393–1406 (2011).

57. Song, Y. S. *et al.* PET/CT-Based Dosimetry in 90Y-Microsphere Selective Internal Radiation Therapy. *Medicine (Baltimore).* **94,** e945 (2015).

58. Dezarn, W. a. *et al.* Recommendations of the American Association of Physicists in Medicine on dosimetry, imaging, and quality assurance procedures for 90Y microsphere brachytherapy in the treatment of hepatic malignancies. *Med. Phys.* **38,** 4824–4845 (2011).

59. Simpkin, D. J. & Mackie, T. R. EGS4 Monte Carlo determination of the beta dose kernel in water. *Med. Phys.* **17,** 179–186 (1990).

60. Minarik, D., Gleisner, K. S. & Ljungberg, M. Evaluation of quantitative 90 Y SPECT based on experimental phantom studies. *Phys. Med. Biol.* **53,** 5689–5703 (2008).

61. Rong, X. *et al.* Development and evaluation of an improved quantitative 90 Y bremsstrahlung SPECT method. *Med. Phys.* **39,** 2346–2358 (2012).

62. Murthy, R. *et al.* Therapy for Hepatic Malignancy : Devices , Indications , Technical Considerations , and OBJECTIVES. *RadioGraphics* **25,** 41–56 (2005).

63. Denardo, G. L., Siantar, C. L. H. & DeNardo, S. J. Radiation Dosimetry for Radionuclide Therapy in a Nonmyeloablative Strategy. *Cancer Biother. Radiopharm.* **17,** 107–118 (2002).

64. Zanzonico, P. B. Internal radionuclide radiation dosimetry: a review of basic concepts and recent developments. *J. Nucl. Med.* **41,** 297–308 (2000).

65. Lam, M. G. E. H. *et al.* Limitations of body surface area-based activity calculation for radioembolization of hepatic metastases in colorectal cancer. *J. Vasc. Interv. Radiol.* **25,** 1085–1093 (2014).

66. Bernardini, M. *et al.* Liver Selective Internal Radiation Therapy with 90Y resin microspheres: Comparison between pre-treatment activity calculation methods. *Phys. Medica* **30,** 752–764 (2014).

67. Flux, G. *et al.* The Impact of PET and SPECT on Dosimetry for Targeted Radionuclide Therapy. *Z. Med. Phys.* **16,** 47–59 (2006).

68. Bolch, W. E., Eckerman, K. F., Sgouros, G. & Thomas, S. R. MIRD Pamphlet No . 21 : A Generalized Schema for Radiopharmaceutical Dosimetry — Standardization of Nomenclature. *J. Nucl. Med.* **50,** 477–485 (2009).

69. Siegel, J. A. *et al.* MIRD pamphlet no. 16: Techniques for quantitative radiopharmaceutical biodistribution data acquisition and analysis for use in human radiation dose estimates. *J. Nucl. Med.* **40,** 37S–61S (1999).

70. Liu, C. S. *et al.* Model-based radiation dose correction for yttrium-90 microsphere treatment of liver tumors with central necrosis. *Int. J. Radiat. Oncol. Biol. Phys.* **81,** 660–668 (2011).

71. Gulec, S. a, Mesoloras, G. & Stabin, M. Dosimetric techniques in 90Y-microsphere therapy of liver cancer: The MIRD equations for dose calculations. *J. Nucl. Med.* **47,** 1209–1211 (2006).

72. Dewaraja, Y. K. *et al.* MIRD Pamphlet No. 23: Quantitative SPECT for Patient-Specific 3-Dimensional Dosimetry in Internal Radionuclide Therapy Yuni. *J. Nucl. Med.* **53,** 1310–1325 (2012).

73. Stabin, M. Nuclear medicine dosimetry. *Phys. Med. Biol.* **51,** R187–R202 (2006).

74. Ljungberg, M. & Sjögreen-Gleisner, K. The accuracy of absorbed dose estimates in tumours determined by Quantitative SPECT : A Monte Carlo study. *Acta Oncol. (Madr).* **50,** 981–989 (2011).

75. Ferlay, J. *et al.* Cancer incidence and mortality worldwide: Sources, methods and major patterns in GLOBOCAN 2012. *Int. J. Cancer* **136,** E359–E386 (2015).

76. Cancer Research UK. Liver cancer statistics. at <http://www.cancerresearchuk.org/health-professional/cancer-statistics/statistics-by-cancer-type/liver-cancer>

77. Fourkal, E. *et al.* 3D inpatient dose reconstruction from the PET-CT imaging of 90Y microspheres for metastatic cancer to the liver: feasibility study. *Med. Phys.* **40,** 081702 (2013).

78. Kennedy, A. S. *et al.* Resin 90Y-microsphere brachytherapy for unresectable colorectal liver metastases: Modern USA experience. *Int. J. Radiat. Oncol. Biol. Phys.* **65,** 412–425 (2006).

79. Kennedy, A. S., Dezarn, W. A., McNeillie, P. & Sangro, B. in *Liver Radioembolization with 90Y Microspheres* (eds. Bilbao, J. I. & Reiser, M. F.) 53–61 (Springer, Berlin, Heidelberg, 2013). doi:10.1007/174_2013_862

80. Vente, M. a D. *et al.* Yttrium-90 microsphere radioembolization for the treatment of liver malignancies: A structured meta-analysis. *Eur. Radiol.* **19,** 951–959 (2009).

81. Breedis, C. & Young, G. The blood supply of neoplasms in the liver. *Am. J. Pathol.* **30,** 969–985 (1954).

82. Cremonesi, M. *et al.* Radioembolization of hepatic lesions from a radiobiology and dosimetric perspective. *Front. Oncol.* **4,** 1–20 (2014).

83. Kennedy, A. *et al.* Recommendations for radioembolization of hepatic malignancies using Yttrium-90 microspheres brachytherapy: a consensus panel report from the radiembolization braquitherapy oncology consortium. *Int. J. Radiat. Oncol. Biol. Phys.* **68,** 13–23 (2007).

84. Zech, C. J. & Reiser, M. F. in *Liver Radioembolization with 90Y Microspheres* (eds. Bilbao, J. I. & Reiser, M. F.) 15–26 (Springer, Berlin, Heidelberg, 2013). doi:10.1007/174_2013_810

85. Sangro, B., Iñarrairaegui, M. & Bilbao, J. I. Radioembolization for hepatocellular carcinoma. *Journal of Hepatology* **56,** 464–473 (2012).

86. Padia, S. a. *et al.* Radioembolization of Hepatic Malignancies: Background, Quality Improvement Guidelines, and Future Directions. *J. Vasc. Interv. Radiol.* 1–14 (2016). doi:10.1016/j.jvir.2016.09.024

87. Salem, R. & Thurston, K. G. Radioembolization with 90yttrium microspheres: a state-of-the-art brachytherapy treatment for primary and secondary liver malignancies. Part 1: technical and methodologic considerations. *J. Vasc. Interv. Radiol.* **17,** 1251–1278 (2006).

88. Jiang, M., Fischman, A. & Nowakowski, F. S. Segmental Perfusion Differences on Paired Tc-99m Macroaggregated Albumin (MAA) Hepatic Perfusion Imaging and Yttrium-90 (Y-90) Bremsstrahlung Imaging Studies in SIR-Sphere Radioembolization: Associations with Angiography. *J. Nucl. Med. Radiat. Ther.* **3,** 1–5 (2012).

89. Kokabi, N. *et al.* A simple method for estimating dose delivered to hepatocellular carcinoma after yttrium-90 glass-based radioembolization therapy: Preliminary results of a proof of concept study. *J. Vasc. Interv. Radiol.* **25,** 277–287 (2014).

90. Sirtex Medical. SIR-Spheres® microspheres - Training Program:physicians and institutions. 108 at <http://foxfireglobal.sirtex.com/sites/foxfireglobal.sirtex.com/files/user/trn-rw-04_for_eu_au_nz_and_asia.pdf>

91. Garin, E. *et al.* Personalized Dosimetry with Intensification Using 90Y-Loaded Glass Microsphere Radioembolization Induces Prolonged Overall Survival in Hepatocellular Carcinoma Patients with Portal Vein Thrombosis. *J. Nucl. Med.* **56,** 339–347 (2015).

92. TheraSphere®. Package Insert – TheraSphere® Yttrium-90 Glass Microspheres – Rev. 14. *MDS Nordion* 1–21 (2014). at <http://www.therasphere.com/physicians-package-insert/package-insert-eu-en.pdf>

93. U.S. Food and Drugs Administration. Summary of Safety and Effectiveness Data: SIR-Spheres®. 15 (2002). at <https://www.accessdata.fda.gov/cdrh_docs/pdf/p990065b.pdf>

94. Burton, M. a., Gray, B. N., Jones, C. & Coletti, A. Intraoperative dosimetry of 90Y in liver tissue. *Int. J. Radiat. Appl. Instrumentation.* **16,** 495–498 (1989).

95. Burton, M. A., Gray, B. N., Kelleher, D. K. & Klemp, P. F. Selective internal radiation therapy: validation of intraoperative dosimetry. *Radiology* **175,** 253–255 (1990).

96. Gray, B. N., Burton, M. A., Kelleher, D. K., Klemp, P. F. & Matz, L. Tolerance of the liver to the effects of yttrium-90 radiation. *Int. J. Radiat. Oncol. Biol. Phys.* **18,** 619–623 (1990).

97. Gray, B. *et al.* Randomised trial of SIR-Spheres plus chemotherapy vs. chemotherapy alone for treating patients with liver metastases from primary large bowel cancer. *Annu. Oncol.* **12,** 1711–1720 (2001).

98. Gulec, S. A., Mesoloras, G., Dezarn, W. A., McNeillie, P. & Kennedy, A. S. Safety and efficacy of Y-90 microsphere treatment in patients with primary and metastatic liver cancer: The tumor selectivity of the treatment as a function of tumor to liver flow ratio. *J. Transl. Med.* **5,** (2007).

99. Kennedy, A. S. *et al.* Treatment Parameters and Outcome in 680 Treatments of Internal Radiation With Resin 90Y-Microspheres for Unresectable Hepatic Tumors. *Int. J. Radiat. Oncol. Biol. Phys.* **74,** 1494–1500 (2009).

100. DuBois, D. & DuBois, E. A formula to estimate the approximate surface area if height and weight be known. *Arch Int Med* **17,** 863–871 (1916).

101. Body Surface Area Calculator. at <http://www.medcalc.com/body.html>

102. Ho, S. *et al.* Tumour-to-normal uptake ratio of 90 Y microspheres in hepatic cancer assessed with 99 Tc m macroaggregated albumin. *Br. J. Radiol.* **70,** 823–828 (1997).

103. Ho, S. *et al.* Partition model for estimating radiation doses from yttrium-90 microspheres in treating hepatic tumours. *Eur J Nucl Med* **23,** 947–952 (1996).

104. Ho, S. *et al.* Clinical evaluation of the partition model for estimating radiation doses from yttrium-90 microspheres in the treatment of hepatic cancer. *Eur J Nucl Med* **24,** 293–298 (1997).

105. Walrand, S., Hesse, M., Demonceau, G., Pauwels, S. & Jamar, F. Yttrium-90-labeled microsphere tracking during liver selective internal radiotherapy by bremsstrahlung pinhole SPECT: feasibility study and evaluation in an abdominal phantom. *EJNMMI Res.* **1,** 32 (2011).

106. Knesaurek, K. *et al.* Quantitative comparison of yttrium-90 (90Y)-microspheres and technetium-99m (99mTc)-macroaggregated albumin SPECT images for planning 90Y therapy of liver cancer. *Technol. Cancer Res. Treat.* **9,** 253–262 (2010).

107. Ng, S. C. *et al.* Patient dosimetry for 90Y selective internal radiation treatment based on 90Y PET imaging. *J. Appl. Clin. Med. Phys.* **14,** 212–221 (2013).

108. Lau, W. Y. *et al.* Treatment of inoperable hepatocellular carcinoma with intrahepatic arterial yttrium-90 microspheres: a phase I and II study. *Br. J. Cancer* **70,** 994–999 (1994).

109. Strigari, L. *et al.* Efficacy and Toxicity Related to Treatment of Hepatocellular Carcinoma with 90Y-SIR Spheres: Radiobiologic Considerations. *J. Nucl. Med.* **51,** 1377–1385 (2010).

110. Sangro, B. *et al.* Liver disease induced by radioembolization of liver tumors: Description and possible risk factors. *Cancer* **112,** 1538–1546 (2008).

111. Stabin, M. G. Update: The Case for Patient-Specific Dosimetry in Radionuclide Therapy. *Cancer Biother. Radiopharm.* **23,** 273–284 (2008).